

ALMA MATER STUDIORUM - UNIVERSITÀ DI BOLOGNA

**Dottorato di Ricerca in Ingegneria Energetica,
Nucleare e del Controllo Ambientale**

Ciclo XXVI

Settore concorsuale di afferenza: 09/G2

Settore scientifico-disciplinare: ING-INF/06

**MULTILEVEL DOMAIN DECOMPOSITION
ALGORITHMS FOR MONOLITHIC
FLUID-STRUCTURE INTERACTION
PROBLEMS WITH APPLICATION TO
HAEMODYNAMICS**

Presentata da: SIMONE BNA'

Coordinatore di Dottorato:

Prof. ANTONIO BARLETTA

Relatore:

Dott. Ing. RUBEN SCARDOVELLI

Esame finale anno 2014

To my girlfriend Marianna, to my loving parents, Luisa e Angelo,
and to my sister Francesca.

Acknowledgements

My first acknowledgment paragraph goes to my advisor, prof. Ing. Ruben Scardovelli. Thank you for your support, encourage and the trust you put in me over the three years. His professional experience has been important for my growth in the scientific research methodology.

I would like to express my gratitude to my co-advisor prof. Ing. Sandro Manservigi. As my teacher, Sandro guided me into the wonderful world of numerical analysis and finite element method. I thank him for his important advices during my initial phase of PhD studies.

I would like to express my appreciation to my co-advisor prof. Ing. Eugenio Aulisa for his support and motivation throughout my research work. I feel very fortunate to work closely with him. He helped me during the final phase of my PhD studies to improve my knowledge on domain decomposition algorithms, multigrid solvers and Vanka smoothers. His availability and optimism were essential for the completion of this thesis.

I am also sincerely grateful to all the people I knew during my PhD permanency at department of Mathematics and Statistics of Texas Tech University in Lubbock - Texas. In particular, I want to acknowledge prof. Akif Ibraguimov for the long discussions on several subjects, for his criticism and for the enjoyable evenings spent watching movies and tasting wine.

Thanks to all the people at laboratory of Montecuccolino for the good times we spent together and for the long discussions we took during the meal. In particular, I want to acknowledge my friend Alberto

Previti for the long debates in my office and for the trips together in scooter.

A special paragraph goes to my friend Giorgio Bornia. Reflecting back on my enjoyable and painful PhD journey, my experience at Texas Tech and at laboratory of Montecuccolino would not have been such a pleasurable one without his presence. I am greatly indebted for his availability, criticism and optimism that they have been important for the completion of this thesis.

And last, but not the least, I want to express my heartiest thanks to my parents and my girlfriend Marianna who have to live with a numerical computing scientist.

Bologna, February 15, 2014

Simone Bnà

Abstract

Finite element techniques for solving the problem of fluid-structure interaction of an elastic solid material (incompressible or compressible) in a laminar incompressible viscous flow are described. The mathematical problem consists of the Navier-Stokes equations in the Arbitrary Lagrangian-Eulerian formulation coupled with a non-linear structure model, considering the problem as one continuum. The coupling between the structure and the fluid is enforced inside a monolithic framework which computes simultaneously for the fluid and the structure unknowns within a unique solver. We used the well-known Q_2P_1 Crouzeix-Raviart finite element pair for discretization in space and the method of lines for discretization in time. A stability result using the Backward-Euler time-stepping scheme for both fluid and solid part and the finite element method for the space discretization has been proved. The resulting linear system has been solved by multilevel domain decomposition techniques. Our strategy is to solve several local subproblems over subdomain patches using the Schur-complement or GMRES smoother within a multigrid iterative solver. For validation and evaluation of the accuracy of the proposed methodology, we present corresponding results for a set of two FSI benchmark configurations which describe the self-induced elastic deformation of a beam attached to a cylinder in a laminar channel flow, allowing stationary as well as periodically oscillating deformations, and for a benchmark proposed by COMSOL multiphysics where a narrow vertical structure attached to the bottom wall of a channel bends under the force due to both viscous drag and fluid pressure. Then, as an example of fluid-structure interaction in biomedical problems, we con-

sidered the academic numerical test which consists in simulating the pressure wave propagation through a straight compliant vessel.

All the tests show the applicability and the numerical efficiency of our approach to both two-dimensional and three-dimensional problems.

Keywords: Fluid-Structure Interaction (FSI), monolithic FEM, ALE, multigrid, multilevel domain decomposition, Vanka smoother, incompressible laminar flow, bio-engineering.

Contents

Contents	vii
List of Figures	xi
List of Tables	xv
1 Introduction	1
2 Introduction to Functional Analysis	11
2.1 The Conceptual Path from the PDE problem to the Solution . . .	12
2.2 Preliminary notation and function spaces	13
2.2.1 Hilbert and Banach spaces	14
2.2.2 Dual Spaces	15
2.2.3 L^p spaces	15
2.2.4 Generalized (weak) derivatives	17
2.2.5 Sobolev spaces	19
2.3 Some results about Sobolev spaces	21
3 Mathematical Modeling	25
3.1 Overview	25
3.2 Continuum theory	28
3.2.1 Kinematic descriptions	28
3.2.1.1 Configurations	30
3.2.1.2 Lagrangian description	30
3.2.1.3 Eulerian description	32
3.2.1.4 Arbitrary Lagrangian Eulerian Description	32

CONTENTS

3.2.2	Deformation and strain	36
3.2.3	Stress tensors	40
3.3	Balance Laws	43
3.3.1	Balance of mass	44
3.3.2	Balance of Momentum	46
3.3.3	Balance of Angular Momentum	49
3.3.4	Balance of Energy	49
3.4	Fluid Structure Interaction problem formulation	50
3.4.1	Continuum description	50
3.5	Constitutive equations	56
3.5.1	Constitutive equations for incompressible fluid	56
3.5.1.1	Generalized Newtonian Fluid	57
3.5.2	Constitutive equations for solid	60
3.5.2.1	Elastic Material	61
3.5.2.2	Hyperelastic material	61
3.5.2.3	Incompressible and nearly incompressible hyper- elastic material	63
4	Discretization procedure	67
4.1	The Galerkin Method	67
4.1.1	Introduction	67
4.1.2	An abstract reference Boundary Value Problem	68
4.1.3	Description of the method	70
4.2	The Galerkin Finite Element Method	72
4.2.1	Introduction	72
4.2.2	Triangulation	73
4.2.3	Finite element interpolation	74
4.2.4	Conforming Q_2P_1 Element	76
4.3	Temporal discretization	78
4.3.1	Theta-scheme method	79
4.3.2	Generalized alpha method	81
4.4	Weak formulation	84
4.4.1	Continuous weak formulation	84

4.4.2	Space-time discretized weak formulation	87
5	Solvers	93
5.1	Introduction	93
5.2	Nonlinear solver	95
5.2.1	Newton’s method	95
5.2.2	Modified Newton’s methods	96
5.2.3	Quasi-Newton’s methods	98
5.3	Linear Solvers	100
5.3.1	Krylov Subspace Solver	101
5.3.1.1	Preconditioning techniques	103
5.3.2	Multigrid Solver	104
5.3.2.1	Multilevel Domain Decomposition	105
5.3.2.2	Vanka-type smoothers	111
6	Numerical results	119
6.1	Navier-Stokes Turek Benchmark	119
6.1.1	Definitions	119
6.1.2	Numerical Results	124
6.2	FSI numerical benchmarks	126
6.2.1	FSI Hron-Turek Benchmark	126
6.2.1.1	Definitions	128
6.2.1.2	Numerical Results	134
6.2.2	FSI COMSOL Multiphysics Benchmark	138
6.2.2.1	Definitions	139
6.2.2.2	Numerical results	143
6.3	Biomedical application: wave propagation in a compliant vessel	145
6.3.1	Definitions	146
6.3.2	Numerical results	149
7	Conclusions	155
	Appendix	159
	References	161

CONTENTS

List of Figures

1.1	Coupling strategies for multi-physics FSI problems.	3
2.1	The conceptual path from the PDE problem to the solution. . . .	13
3.1	Sketch of the referential domain Ω , initial domain Ω_0 and current domain Ω_t and relations between them.	27
3.2	Transformation of a material volume under deformation and displacement fields \mathbf{U} and \mathbf{u} of a generic material particle.	29
3.3	Top: 1D Lagrangian description; Middle: 1D Eulerian description; Bottom: 1D ALE (Arbitrary Lagrangian-Eulerian) description. . .	31
3.4	The initial domain Ω , the current domain Ω_t , the moving computational domain $\Omega_{\mathcal{X}}$ and the relations between them.	34
3.5	Traction vector.	41
3.6	Undeformed (reference) and deformed (current) configurations of a system in which a vessel wall interacts with a fluid.	50
4.1	Location of the degrees of freedom for the (Crouzeix-Raviart) Q_2P_1 element.	77
5.1	Sparsity pattern of the Jacobian matrix of the FSI operator. . . .	98
5.2	Example of a non conforming mesh built using multilevel triangulations.	106
5.3	Weights for the prolongation operator in Q_2 with biquadratic interpolation.	109
5.4	Multigrid V, W and F cycles.	111
5.5	Vanka-block for the FSI $Q_2Q_2P_1$ Crouzeix-Raviart finite element. .	113

LIST OF FIGURES

6.1	Computational domain.	121
6.2	Coarse Mesh.	121
6.3	u velocity field.	125
6.4	Plot of the pressure and drag and lift stresses over the circle perimeter.	125
6.5	Pressure field in the dark gray region.	126
6.6	Domain partition among 6 processors for different levels of refinement: Figure (a) shows the domain partition of the whole region at level 3, Figure (b-c) the domain partition of the gray and dark gray regions at level 3+2, Figure (d) only the dark gray region at level 3+2+1.	127
6.7	Computational domain and detail of the beam.	128
6.8	Coarse mesh.	129
6.9	Integration path $S = S_1 \cup S_2$ for the force calculation.	133
6.10	x and y displacement of the point A.	136
6.11	Fluid flow during one-half oscillation for the FSI3 benchmark.	137
6.12	y-displacement field during one-half oscillation for the FSI3 benchmark.	137
6.13	Computational domain.	139
6.14	Coarse mesh.	140
6.15	Integration path for the force calculation.	142
6.16	u velocity and mesh deformation at $t = 4s$; the contour lines indicates the u velocity field.	144
6.17	Geometry and mesh near the top of the structure at $t = 0s$ and $t = 0.21s$	145
6.18	Inflow maximum velocity, horizontal mesh deformation and mesh velocity. The solid curve shows the maximum u velocity at the inflow boundary (m/s); the dashed one shows the mesh displacement in the x direction (mm) at the geometry point $(1.00275e^{-04}m, 6.83267e^{-05}m)$; the dotted one shows the mesh velocity in the x direction (mm/s) at the same point.	146
6.19	Computational domain.	147
6.20	Coarse mesh.	148

LIST OF FIGURES

6.21	Maximum solid displacement magnitude.	151
6.22	In- and out-flow rates.	151
6.23	Plot over time of the solid displacement magnitude in the middle section of the cylinder for different meshes.	151
6.24	Pressure wave propagation.	152
6.25	Solid domain deformed configuration.	153

LIST OF FIGURES

List of Tables

3.1	Various generalized Newtonian models for blood.	59
6.1	Overview of the geometry parameters.	121
6.2	Number of elements and degrees of freedom for refined levels. . . .	122
6.3	Results for the Turek-Navier Stokes benchmark.	124
6.4	Execution times of the parallel steady Navier-Stokes solver.	127
6.5	Overview of the geometry parameters.	129
6.6	Number of elements and degrees of freedom for refined levels. . . .	130
6.7	Overview of some solid material parameters.	132
6.8	Overview of some fluid material parameters.	133
6.9	Parameter settings for the Hron-Turek FSI benchmarks.	135
6.10	Results for FSI1.	136
6.11	Results for FSI3 using the Backward-Euler algorithm for both fluid and solid equations.	138
6.12	Results for FSI3 using the Backward-Euler algorithm for the fluid equations and the Generalized-alpha algorithm for the solid equa- tions.	138
6.13	Overview of the geometry parameters.	140
6.14	Number of elements and degrees of freedom for refined levels. . . .	141
6.15	Results for COMSOL benchmark.	144
6.16	Overview of the geometry parameters.	147
6.17	Number of elements and degrees of freedom for refined levels. . . .	148

LIST OF TABLES

Chapter 1

Introduction

Since the early eighties a great interest in solving Fluid-Structure Interaction (FSI) problems has been increasing because of a large number of applications that can be found in various fields of physics and engineering disciplines such as aerodynamics, elasticity, civil engineering, biomechanics, hemodynamics, meteorological phenomena and hydroelasticity. Among the multitude of multi-physics problems we may cite, for instance, the problem of fluttering of wings and structures such as bridges, mechanical vibrations or water hammer effects in pipe network, parachute modeling, environmental hazards, petroleum flow in porous media and blood flow in large arteries. These are only a few examples of fluid-structure interaction problems that engineers have to deal with.

In particular, a great interest in the numerical solution of the equations of fluid-structure interaction arised in the medical community because a detailed understanding of the cardiovascular system can have interesting clinical applications, for instance, the prediction of the consequences of a surgical intervention, and can lead to a reduction of the risk of cardiovascular diseases.

In all fluid-structure interaction physical processes, fluid and structure dynamics influence each other in a nonlinear way. Indeed, the structure changes its shape under the action of the fluid force and, conversely, the fluid flow is altered by the structure deformation. In other words, the fluid follows the structure motion and in the meantime the region in which the fluid is confined changes as a consequence of the structure deformation.

Typically, structure dynamics are described in a Lagrangian frame of refer-

1. INTRODUCTION

ence, i.e. with respect to a fixed (material) configuration, while the fluid equations are derived using the Eulerian frame which allows us to describe the fluid quantities in the physical (spatial) domain.

In those situations where the structure deformation is relatively small, the fluid domain can be approximated as a fixed domain and the interaction of the structure onto the fluid flow can be accounted for by suitable boundary conditions that are called *transpiration conditions*. This approach is widely used in the context of wing fluttering or more generally in all physical situation where fluid flow induces vibrations in the structure. If the structure displacement is such that the change of the fluid domain is not negligible, as for instance in hemodynamics where, during a cardiac beat, the diameter of an artery can increase or decrease of about 10%, we have to face with the complex problem of solving the fluid equations on a moving domain.

Different techniques have been proposed by scientists in the literature to face the problem of numerical approximation of Partial Differential Equations (PDEs) on moving domains. The most popular technique is the *Arbitrary Lagrangian Eulerian (ALE) formulation* that was proposed at the beginning of the eighties by Hughes and Donea (see e.g. Donea [1983]; Donea *et al.* [1982]; Hughes *et al.* [1981]). This method is based on the construction of an appropriate (arbitrary) mapping from the fluid fixed reference configuration to the current moving domain. The ALE mapping is practically constructed as a harmonic extension of the trace of the structure displacement on the fluid-solid interface. Other methods are the *space-time approach*, (see e.g. Masud & Hughes [1997]; Tezduyar *et al.* [1992a,b] and Hübner *et al.* [2004]; Mittal & Tezduyar [1995] for FSI applications), the *fictitious domain method* (Glowinski *et al.* [1994a,b]), the *level set method* (Chang *et al.* [1996]), the *volume of fluid method* (see Appendix) and finally the *immersed boundary method* proposed by C. Peskin (Peskin [1977]; Peskin & McQueen [1989]) and applied successfully since the end of seventies to the numerical simulation of heart contractions.

In recent years, the development of computational techniques in fluid dynamics (CFD) and structural mechanics (CSM), together with the increasing computing power of modern computers, has allowed simulations to be effective and valuable for the design of many systems in the engineering practice. Many

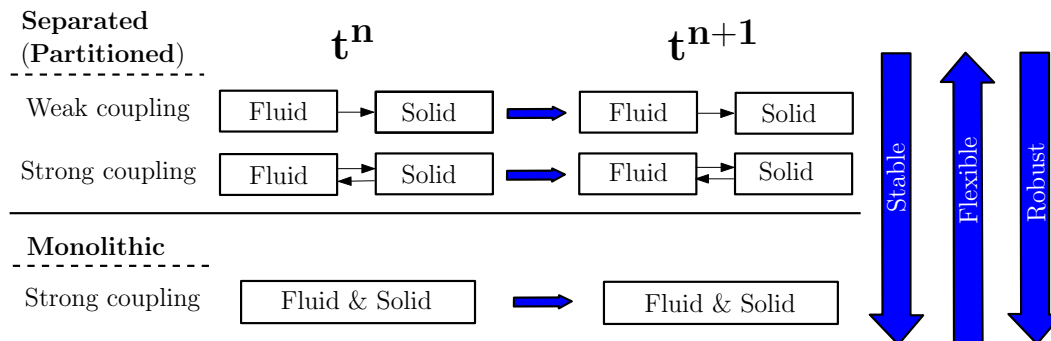


Figure 1.1: Coupling strategies for multi-physics FSI problems.

commercial programs have been developed, tested on benchmark settings and successfully applied as development tool for complex engineering problems. However, experimental setups are fundamental to provide reliable data for code validation despite its associated enormous costs.

Fluid-structure interaction physical processes are so complex that the combined solution of FSI problems cannot be obtained analytically but it necessitates of numerical techniques and computational tools. However, nowadays, there are still challenging questions in the FSI solution strategies ranging from mathematical modeling, numerical discretization, linear solver and implementation issues.

Concerning the coupling between the solid and fluid unknowns, the different approaches to solve fluid-structure interaction problems can be divided in two broad categories, the *separated or partitioned* approach and the *monolithic* approach (see Figure 1.1). The solution strategy that is most commonly encountered and implemented in software packages is the so-called partitioned approach (Hron *et al.* [2002]). This consists in decoupling the problem into separate sub-problems for the fluid and solid domains, where for each of them well-tested numerical solution techniques and efficient solvers are available. According to this solution strategy the coupling between the two physical domains eventually consists in a external boundary condition to be enforced at the interface. For this case the memory requirements are lower, the approach is more flexible and fewer programming efforts are required since existing computational codes can be reused. The drawback of the segregated approach is the treatment of the interface force which can lead to instabilities and convergence problems when *ex-*

1. INTRODUCTION

implicit partitioned algorithms (also called loosely coupled strategies) are adopted. This issue is important, for instance, in hemodynamics, when the solid material is light with a density of the same order of magnitude as that of the fluid one. The reason is that in this kind of system the interaction between fluid and solid is very strong and one or just few iterations per time step may not be sufficient to compute correctly the force at the interface, even if implicit time-stepping schemes are used by the two-solvers. In these cases numerical experiments show that only fully-coupled algorithms, which are based on subsequent solutions of the fluid and structure subproblems, exhibit good stability properties (Causin *et al.* [2005]; Förster *et al.* [2007]). Several sub-structuring strategies have been investigated so far; see, e.g., Deparis *et al.* [2003b, 2006]; Fernández & Moubachir [2005]; Fernández *et al.* [2007]; Gerbeau & Vidrascu [2003]; Le Tallec & Mouro [2001]; Matthies & Steindorf [2000].

Alternatively, one could manage implicitly the coupling conditions at each time step (*implicit* algorithms), leading to monolithic algorithms, which are fully coupled by definition. Monolithic algorithms solve simultaneously for the fluid and the structure unknowns in a unique solver, so that the solid and fluid regions are treated as a single continuum and the boundary conditions at the interface are automatically taken into account (Heil [2004]; Hron & Turek [2006]). Monolithic fully-coupled algorithms are always stable in the energy norm but they are also CPU-time expensive. This issue is enhanced by the saddle-point character of the incompressible solid and fluid formulation and is of particular importance in 3D geometries where a high number of degrees of freedom has to be managed.

The approach that we have pursued in this thesis is a monolithic strong coupling strategy. This approach is the most robust and stable one among the strong coupling approaches, but it requires strong programming efforts and the development of strategies to reduce the computational time. In this thesis, we have developed and validated a Finite Element Method (FEM) C++ library for solving the problem of fluid-structure interaction of a compressible/incompressible elastic solid object in a laminar incompressible viscous flow based on Selective Multilevel Domain Decomposition (SMDD) numerical techniques. In several physical fields, such as FSI, CFD or two-phase flow, it is of interest to have an algorithm that is able to handle finer mesh near interfaces and in boundary layers where the

solution has strong variations. The selective multilevel domain decomposition technique allows the user to select the regions of mesh refinement in order to reduce the degrees of freedom to be solved. The selective domain decomposition method has been investigated in the paper of (Aulisa *et al.* [2006]) in the context of fluid-dynamics and extended to fluid-structure interaction and fluid-structure-thermal interaction loosely coupled problems (Aulisa *et al.* [2008, 2009]). We have decided to extend this method to two and three dimensional monolithic fluid-structure interaction problems to reduce the computational time in the FSI solution process (Bnà *et al.* [2013a]).

It is known that domain decomposition methods allow for effective implementation of numerical techniques for partial differential equations on parallel architectures. In this work the parallelization of these numerical techniques has been performed by using the library *PETSCs* (Balay *et al.* [1997, 2013]). We observed a cpu-time reduction when multilevel domain decomposition methods are used for solving CFD, CSM and FSI problems, both in serial and parallel computations, with respect to standard Krylov based solvers.

During my PhD studies we have investigated the possibility of splitting the update of the domain from the computation of the physical quantities which define the status of the fluid and the solid (Bnà *et al.* [2012a,b]). This leads to a *semi-implicit* algorithm where the domain configuration is treated in an explicit way. We reformulated the solid problem from a displacement-pressure formulation into a velocity-pressure one, so that the solid and fluid unknowns (velocity and pressure) are written together in a monolithic manner. Then a velocity-pressure splitting is performed by using a projection method, which consists of two steps. In the first predictor step, an intermediate velocity, which does not satisfy the divergence constraint, is computed. This velocity is projected onto a divergence-free space in a subsequent pressure correction step (Guermond *et al.* [2006]; Jobelin *et al.* [2006]). In this way a mathematical velocity-pressure decoupling is performed without partitioning the domain. This cancels the oscillations induced by the solid-fluid partitioning in the enforcement of the interface conditions. On the external solid surface a penalty term is added in order to enforce the correct stress-free boundary conditions.

The fluid-structure interaction equations have been formulated adopting a

1. INTRODUCTION

mixed description. The ALE (Arbitrary-Lagrangian-Eulerian) description has been used for the fluid equations while the Lagrangian description has been adopted for the solid ones. We have discretized the velocity and displacement quantities in two and three dimensions by utilizing the high order biquadratic finite element Q_2 and the discontinuous linear P_1 finite element for the pressure variable to maintain high accuracy. This choice of finite element for variable discretization is such that the well-known *LBB-stability condition* is not violated.

The resulting discrete nonlinear system for the variables displacement, velocity and pressure is solved by utilizing outer quasi-Newton iterations in a fully coupled monolithic framework. Due to the finite element method, the sparsity pattern of the Jacobian matrix is known in advance and computed by numerical integration of the Fréchet Derivative of a simplified FSI operator. Other variants have been proposed in literature. [Hron & Turek \[2006\]](#) utilize outer quasi-Newton iterations with line search and computes the Jacobian matrix by divided difference approach, [Fernández & Moubachir \[2005\]](#) adopt a Newton method with the exact computation of the Fréchet Derivative of the FSI operator while [Gerbeau & Vidrascu \[2003\]](#) implement a quasi-Newton algorithm based on a reduced model for fluid-structure interaction problems.

Inside one Newton step, the solution of the linear subsystem is the most time consuming part of the whole solution process in terms of the CPU time ([Turek \[1999\]](#)). The matrix associated to the FEM discretization of the FSI equations is sparse. This matrix can be inverted by direct solver like UMFPACK ([Davis & Duff \[1999\]](#)) for the serial case or MUMPS ([Amestoy *et al.* \[2000\]](#)) for the parallel case. This choice provides a very robust linear solver but its memory and CPU time requirements are too high for systems with more than 20,000 unknowns.

Alternatively, large linear subproblems can be solved by Krylov-space iterative methods (BiCGStab, GMRes ([Balay *et al.* \[2013\]](#); [Saad \[2000\]](#))) with suitable preconditioners. The ILU preconditioner is a good candidate because it has been successfully used for problems arising from unstructured finite element grids. The saddle point character of our FSI discretized system requires a special treatment because we have to allow a certain fill-in for the zero diagonal block of the resulting sparsity matrix.

Nowadays, the multigrid solver is the most efficient algorithm for the nu-

merical solution of a large sparse linear subproblems with more than 100,000 unknowns. In this thesis we have used an algebraic geometric multigrid approach based on a hierarchy of linear operators obtained directly from the system matrix. The complete multigrid iteration is performed in the standard defect-correction setup with the possibility of choosing the V or F-type cycle. While the coarse grid solution is obtained by inverting the corresponding matrix with a direct sparse solver, on finer levels several local subproblems over subdomain patches using Vanka-smoothing or Pressure-Schur-Complement-smoothing procedures are solved. This solver is very robust and its efficiency can be increased if the selective domain decomposition method is applied, in particular in the parallel context.

Different time stepping schemes can be adopted in the context of fluid-structure interaction, like the well-known Backward Euler, the Crank-Nicholson, the Newmark method and its variant or the Fractional step θ -scheme. In our numerical simulations we used the strongly A-stable Backward-Euler scheme for both solid and fluid parts, or alternatively the Backward Euler-scheme for the fluid domain and the generalized-alpha scheme for the solid domain.

In this research work we seek to validate and evaluate the accuracy and performance of the proposed methodology for a set of FSI benchmark configurations that can be found in literature (see [Bathe & Ledezma \[2007\]](#); [Fernández & Moubachir \[2005\]](#); [Turek & Hron \[2006\]](#)).

The first example deals with the self-induced elastic deformation of a beam attached to a infinite rigid cylinder in a laminar channel flow. The magnitude of the average inlet velocity determines if stationary or periodically-oscillating deformations are induced. Our results has been compared with the numerical results reported in the paper of [Turek & Hron \[2006\]](#).

The second example describe the interaction between the fluid and a vertical beam in a narrow microchannel. The boundary conditions are time-dependent but the high viscosity of the fluid is such that the beam and the fluid reach a final steady configuration. This benchmark belongs to a set of tests proposed by the COMSOL Multiphysics® company.

The third example deals with the propagation of a wave in a compliant vessel. This fluid-structure interaction problem arises in the modeling of the blood flow in large arteries: it consists of a thin elastic vessel that interacts with a viscous

1. INTRODUCTION

incompressible fluid. We have compared our results with the ones proposed in the papers by [Fernández & Moubachir \[2005\]](#) and [Formaggia *et al.* \[2001\]](#).

In bioengineering, modeling FSI in the cardiovascular system is a vast and complex mathematical subject. Even a simplified description of the vessel wall behavior leads to algorithms that can suffer from stability and convergence problems (see [Causin *et al.* \[2005\]](#)). Arterial walls are anisotropic and heterogeneous, composed of layers with different biomechanical characteristics (see [Fung \[1993\]](#)). A variety of different models has been suggested in the literature to model the mechanical behavior of arteries (see [Fung \[1993\]](#); [Humphrey \[1995\]](#); [Quarteroni *et al.* \[2000\]](#); [Vito & Dixon \[2003\]](#)), ranging from the detailed description of each of the layers to the average description of the total mechanical response of the vessel wall under the assumptions of homogeneity, linear elastic behavior, special geometry, symmetry and periodicity. In this thesis, we assumed the hypothesis of homogeneity and isotropy and the mechanical behavior of the vessel wall has been described by the Neo-Hookean non-linear model.

Talking about the blood, different models has been suggested in the literature to model is non-linear behavior. However, if the diameter value of the artery is not too small, as in our cases, the linear assumption of the Newton model can be accepted.

The contents of the thesis are organized as follows.

Chapter 2 will provide the notation that will be used throughout the thesis, the basic concepts of Functional Analysis and the most important results of the theory of Sobolev Spaces. This abstract framework will be used in the formulation of the numerical algorithms for the solution of the fluid-structure interaction equations.

Chapter 3 will present the mathematical modeling of the multi physical phenomena depicting the fluid-structure interaction with all necessary theoretical descriptions and mathematical formulas. It will also gives a comprehensive overview over the basic principles of continuum mechanics needed for the mathematical description of a monolithic-ALE formulation.

Chapter 4 will discuss and suggest the Galerkin finite element and the time discretization techniques for the numerical discretization of the fluid-structure interaction equations coupled in a monolithic way. A stability result using the Backward-Euler time-stepping scheme for both fluid and solid part and the finite

element method for the space discretization will be also reported.

Chapter 5 will describe the adopted numerical solution strategy of the nonlinear system arising in the numerical discretization of the fluid-structure equations coupled in a monolithic fashion. More specifically, the Newton-method and its variants will be presented together with a general introduction to direct and iterative solvers like Krylov subspace and multigrid solvers. Last section will be dedicated to the general description of a variant of multigrid algorithms, the Multilevel Domain-Decomposition algorithm.

In Chapter 6 we validate the proposed algorithm for a set of well known numerical benchmarks. We will present corresponding results for a set of two FSI benchmark configurations which describe the self-induced elastic deformation of a beam attached to a cylinder in a laminar channel flow, allowing stationary as well as periodically oscillating deformations, and for a benchmark proposed by COMSOL multiphysics where a narrow vertical structure attached to the bottom wall of a channel bends under the force due to both viscous drag and fluid pressure. Then, as an example of fluid-structure interaction in biomedical problems, the academic numerical test which consists in simulating the pressure wave propagation through a straight compliant vessel will be considered.

Finally, in Chapter 7 we will give some conclusions and draw some lines for future works.

1. INTRODUCTION

Chapter 2

Introduction to Functional Analysis

Numerical approximation of Partial Differential Equations (PDE) is an important branch of Numerical Analysis. It is an interdisciplinary field and it requires a knowledge of functional analysis, computer science and calculus of variations.

First of all, the physical background of the problem at hand is required to understand the behavior of the numerical solution.

Secondly, modern formulation of the problem is based on the variational (weak) form since it allows the search for generalized solutions in Hilbert (or Banach) functional spaces. Variational techniques yield a-priori estimates for the solution, which is important because it indicates in which kind of norms any numerical solution can be proven to be stable. Moreover, theoretical results about smoothness of the mathematical solutions may suggest the numerical methodology to be used and consequently the kind of accuracy that can be achieved.

In this introductory chapter we provide the notation that will be used throughout the thesis, the basic concepts of Functional Analysis and the most important results of the theory of Sobolev Spaces. This abstract framework will be used in the formulation of the numerical algorithms for the solution of the fluid-structure interaction equations.

2.1 The Conceptual Path from the PDE problem to the Solution

Let us imagine to have a great number of problems and numerical methods for their solution in mind. For the numerical approximation of a given boundary value problem, what are the possible paths that we may follow to obtain the solution? Let us look to the scheme in Figure 2.1.

Level 1 is the boundary value problem at hand in the weak formulation together with the prescribed boundary conditions.

Level 2 provides the kind of discretization (or numerical method) that can be selected in order to reduce the given problem to one with a finite dimension. Clearly, the strategy adopted will determine the structure of the numerical problem. We consider two kinds of discretization. The former is the *Galerkin method*, together with its remarkable variant, the *Petrov-Galerkin method*, which is based on an integral formulation of the differential problem. The second discretization we consider is the *collocation method*, which is based on the fulfillment of the differential equations at some selected points of the computational domain.

Level 3 specifies the nature of the subspaces where we are looking for the solution. Typically, we have piecewise-polynomial functions of low-degree if we are using finite element subspaces, and global algebraic polynomial functions of high-degree for the spectral method. This choice is crucial because it determines the functional structure of the numerical solution, the kind of accuracy that can be achieved and the topological structure of the resulting algebraic system.

At Level 4 we have to select a numerical algorithm for solving the algebraic form that arises from the discretization of the boundary value problem exploiting, at most, the topological structure and the properties of the associated matrices. In Chapter 5 we will present an overview of the most important methods available nowadays for solving large scale symmetric and non-symmetric linear systems. In particular we will give a presentation of the multigrid techniques that are nowadays the most efficient methods for solving large scale linear system.

For initial-boundary value problems the time discretization have to be carried out between Level 1 and Level 2. Quite often, this is performed using finite difference divided quotients to approximate the time derivatives. However, other

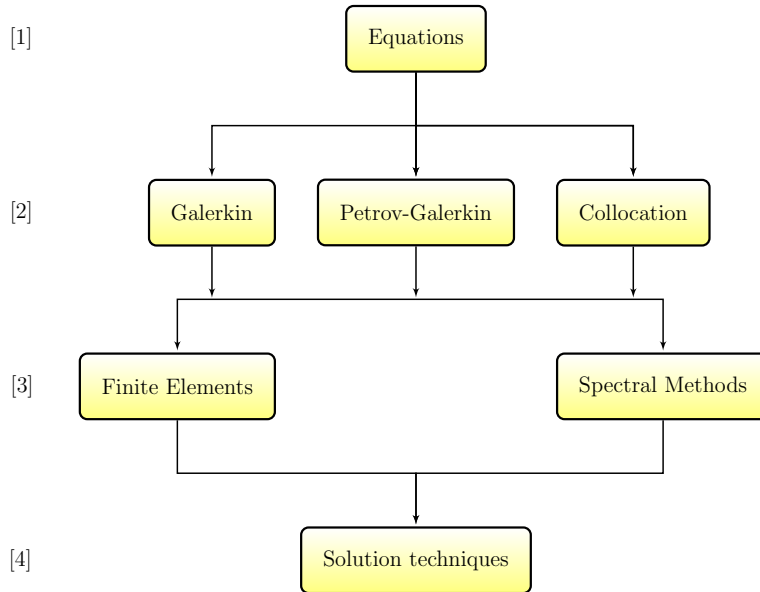


Figure 2.1: The conceptual path from the PDE problem to the solution.

approaches can be pursued, for instance the Crank-Nicolson method which uses the trapezoidal rule for approximate the integral computation. In Chapter 4 we will present some of the most commonly time discretization algorithms used in literature for the solution of fluid-structure interaction problems.

All the numerical results presented in this thesis have been obtained in a double precision on a workstation INTEL® with 6 Xeon® processors E5-1660 (15M Cache, 3.30 GHz) and 16 GB RAM DDR3 (51.2 Gb/s). Compiler is gcc version 4.6.

2.2 Preliminary notation and function spaces

In this section we introduce some notations which will be used in the sequel and we give you an introduction to the basic mathematical tools of the Finite Element Method (FEM). For a complete presentation we refer the reader to, e.g., Yosida [1974] or Brezis [1983].

2. INTRODUCTION TO FUNCTIONAL ANALYSIS

2.2.1 Hilbert and Banach spaces

Definition 2.2.1. Let V be a (real) linear space. A norm, $\|\cdot\|$, is a function on V with values in the non-negative reals having the following properties:

1. a) $\|v\| \geq 0 \quad \forall v \in V$
b) $\|v\| = 0 \iff v = 0$
2. $\|c \cdot v\| = |c| \cdot \|v\| \quad \forall c \in \mathbb{R}, v \in V$
3. $\|v + w\| \leq \|v\| + \|w\| \quad \forall v, w \in V$.

A seminorm is a map $\|\cdot\| : V \rightarrow \mathbb{R}$ that satisfies only the properties 1a, 2 and 3.

Definition 2.2.2. A scalar product on V is a bilinear map $(\cdot, \cdot) : V \times V \rightarrow \mathbb{R}$ such that

1. $(w, v) = (v, w)$ for each $w, v \in V$ (symmetry)
2. $(v, v) \geq 0$ for each $v \in V$ (positivity)
3. $(v, v) = 0$ if and only if $v = 0$.

It is very easy to verify that at any scalar product it is associated a norm through the following definition: $\|v\| := (v, v)^{1/2}$. Moreover, a norm, $\|\cdot\|$, can be used to define a notion of distance, or *metric*, $d(v, w) = \|v - w\|$ for points $v, w \in V$. A vector space endowed with the topology induced by a norm (respectively, a scalar product) is called a *normed linear space* (respectively, pre-hilbertian linear space). A special case of metric space is the *complete metric space*. For a complete metric space, every *Cauchy sequence* $\{v_j\}$ of elements of V has a limit $v \in V$. We recall that, for a normed linear space, a Cauchy sequence is one such that $\|v_j - v_k\| \rightarrow 0$ as $j, k \rightarrow \infty$. By using this definition, *completeness* means that $\|v - v_j\| \rightarrow 0$ as $j \rightarrow \infty$. We are now in the position to give the definition of Banach and Hilbert spaces. These function spaces play a key role in the modern formulation of mathematical problem based on the variational form since they are the function spaces where we are looking for generalized solutions.

Definition 2.2.3. A normed linear space $(V, \|\cdot\|)$ is called a **Banach space** if it is complete with respect to the metric induced by the norm, $\|\cdot\|$.

Definition 2.2.4. A pre-hilbertian linear space $(V, (\cdot, \cdot))$ is called a **Hilbert space** if it is complete with respect to the metric induced by the scalar product, (\cdot, \cdot) .

In a Hilbert space the *Schwarz' Inequality* holds

$$|(w, v)| \leq \|w\| \|v\| \quad \forall w, v \in V. \quad (2.1)$$

2.2.2 Dual Spaces

If $(V, \|\cdot\|_V)$ and $(W, \|\cdot\|_W)$ are normed spaces, we denote by $\mathcal{L}(V; W)$ the set of linear continuous functionals from V into W , and for $L \in \mathcal{L}(V, W)$ we define the norm

$$\|L\|_{\mathcal{L}(V; W)} := \sup \frac{\|Lv\|_W}{\|v\|_V} \quad \forall v \in V, v \neq 0. \quad (2.2)$$

Therefore $\mathcal{L}(V; W)$ is a normed space; moreover, if W is a Banach space then $\mathcal{L}(V; W)$ is a Banach space, too. If $W = \mathbb{R}$, the space $\mathcal{L}(V; W)$ is called the *dual space* of V and is denoted by V' . The bilinear form $\langle \cdot, \cdot \rangle$ from $V' \times V$ into \mathbb{R} defined as $\langle L, v \rangle := L(v)$ is called the *duality pairing* between V' and V . As a consequence of the *Riesz representation theorem*, if V is a Hilbert space then the dual space V' is a Hilbert space too and it can be canonically identified with V .

2.2.3 L^p spaces

We now introduce some spaces of functions that are the basis of the modern theory of partial differential equations. Let Ω be a Lebesgue-measurable open set contained in \mathbb{R}^d , $d \geq 1$, with non-empty interior. Let $1 \leq p \leq \infty$, and consider the set of real-valued Lebesgue measurable functions v such that

$$\int_{\Omega} |v(\mathbf{x})|^p d\mathbf{x} < \infty, \quad 1 \leq p < \infty, \quad (2.3)$$

or, when $p = \infty$,

$$\sup\{|v(\mathbf{x})| : \mathbf{x} \in \Omega\} < \infty, \quad (2.4)$$

2. INTRODUCTION TO FUNCTIONAL ANALYSIS

where we have denoted with

$$\int_{\Omega} |v(\mathbf{x})|^p d\mathbf{x} \quad (2.5)$$

the Lebesgue integral of v and with $d\mathbf{x}$ the Lebesgue measure. These spaces are called **Lebesgue spaces** and are usually denoted with $L^p(\Omega)$. Their associated norm is

$$\|v\|_{L^p(\Omega)} := \left(\int_{\Omega} |v(\mathbf{x})|^p d\mathbf{x} \right)^{1/p}, \quad 1 \leq p < \infty, \quad (2.6)$$

or, when $p = \infty$,

$$\|v\|_{L^\infty(\Omega)} := \sup\{|v(\mathbf{x})| : \mathbf{x} \in \Omega\}. \quad (2.7)$$

To be precise, $L^p(\Omega)$ denoted the space of classes of equivalence of measurable functions, satisfying (2.3) or (2.4) with respect to the equivalence relation: $w \equiv v$ if w and v are different on a subset having zero measure. In fact, we know from the Lebesgue theory that the Lebesgue integral does not change its value if the integrand function assumes different values on a subset of points having zero measure. In other words, if two functions that belong to the $L^p(\Omega)$ space differ only on a subset of measure zero, we view them as representing the same function. As a consequence, the definition of the space $L^\infty(\Omega)$ in (2.4) and of its norm in (2.7) should be modified in the following way: $v \in L^\infty(\Omega)$ if

$$\inf\{M \geq 0 : |v(\mathbf{x})| \leq M \text{ almost everywhere in } \Omega\} < \infty, \quad (2.8)$$

and

$$\|v\|_{L^\infty(\Omega)} := \{M \geq 0 : |v(\mathbf{x})| \leq M \text{ almost everywhere in } \Omega\}, \quad (2.9)$$

where “almost everywhere” means “except on a subset of Ω having zero measure”.

The following theorem is a cornerstone of Lebesgue integration theory and incorporates the key feature of L^p spaces.

Theorem 2.2.1. *For $1 \leq p \leq \infty$, $L^p(\Omega)$ is a Banach space.*

Moreover, the space $L^2(\Omega)$ is a Hilbert space endowed with the scalar product

$$(w, v)_{L^2(\Omega)} := \int_{\Omega} w(\mathbf{x})v(\mathbf{x}) d\mathbf{x}. \quad (2.10)$$

In the sequel the norm in $L^2(\Omega)$ is denoted by $\|\cdot\|_{0,\Omega}$, or simply $\|\cdot\|_0$ when it

is clear which is the domain Ω . In addition, the scalar product $(\cdot, \cdot)_{L^2(\Omega)}$ is often indicated by $(\cdot, \cdot)_{0,\Omega}$ or simply (\cdot, \cdot) .

There are some important inequalities that hold for functionals defined over L^p spaces. The most important is the *Hölder's Inequality*,

$$\left| \int_{\Omega} w(\mathbf{x})v(\mathbf{x}) \, d\mathbf{x} \right| \leq \|w\|_{L^p(\Omega)} \|v\|_{L^{p'}(\Omega)}, \quad (2.11)$$

where $1 \leq p \leq \infty$ and $(1/p) + (1/p') = 1$, ($p' = \infty$ if $p = 1$). Notice that for $p = 2$ the Hölder's Inequality is the Schwarz' Inequality (2.1) for the Hilbert space $L^2(\Omega)$. In addition, from (2.11) it easily follows that $L^q(\Omega) \subset L^p(\Omega)$ if $p \leq q$ and Ω has a finite Lebesgue measure.

2.2.4 Generalized (weak) derivatives

There are several definitions of derivative that are useful in different context. The classical definition of derivative as the limit of the incremental ratio is a “local” definition since it involves information about the function only near the point where the derivative is computed. In the variational formulation of partial differential equations, (see Chapter 4), pointwise values of derivatives are not needed; only derivatives that can be interpreted as functions in L^p spaces are relevant. We have seen before that pointwise values of functions defined in L^p spaces are not important, only the global behavior describes these kind of functions. Thus, it is natural to develop a global notion of *derivative* that is more suited to L^p spaces.

First, let us introduce the *multi-index* notation that is very useful for partial derivatives. A multi-index, $\boldsymbol{\alpha}$, is an n -tuple of non-negative integers, α_i . The length of $\boldsymbol{\alpha}$ is given by

$$|\boldsymbol{\alpha}| := \sum_{i=1}^n \alpha_i. \quad (2.12)$$

For an infinitely differentiable functions v , we denote by $D^{\boldsymbol{\alpha}}v$ the usual (pointwise) partial derivative

$$D^{\boldsymbol{\alpha}}v := \frac{\partial^{|\boldsymbol{\alpha}|} v}{\partial x_1^{\alpha_1} \dots \partial x_n^{\alpha_n}}. \quad (2.13)$$

2. INTRODUCTION TO FUNCTIONAL ANALYSIS

Next, let us introduce the concept of the *support* of a function defined over some domain in \mathbb{R}^n . For a continuous function, v , this is the closure of the (open) set $\{\mathbf{x} : v(\mathbf{x}) \neq 0\}$. If this is a compact set (i.e., if it is bounded) and it is a subset of the interior of a set, Ω , then v is said to have a “compact support” with respect to Ω . Outside the support of a function, it is natural to define it to be zero, thus extending it to be defined on all of \mathbb{R}^n .

Definition 2.2.5. *Let Ω be a domain in \mathbb{R}^n . Denote by $\mathcal{D}(\Omega)$ or $C_0^\infty(\Omega)$ the set of $C^\infty(\Omega)$ functions with compact support in Ω .*

We now use the space \mathcal{D} to extend the notion of pointwise derivative to a class of functions that is larger than $C^\infty(\Omega)$. For simplicity, we restrict our notion of derivatives to the following space of functions.

Definition 2.2.6. *Given a domain Ω , the set of **locally integrable** functions is denoted by*

$$L_{loc}^1(\Omega) := \{v : v \in L^1(K) \quad \forall \text{ compact } K \subset \text{interior } \Omega\}. \quad (2.14)$$

$L_{loc}^1(\Omega)$ is a function space that contains all of $C^0(\Omega)$, without growth restrictions. This implies that functions that belongs to $L_{loc}^1(\Omega)$ can behave arbitrarily badly near the boundary. Finally we can read the new definition of derivative.

Definition 2.2.7. *We say that a given function $v \in L_{loc}^1(\Omega)$ has a **weak derivative**, $D_w^\alpha v$, provided there exists a function $w \in L_{loc}^1(\Omega)$ such that*

$$\int_{\Omega} w(\mathbf{x})\phi(\mathbf{x}) d\mathbf{x} = (-1)^{|\alpha|} \int_{\Omega} v(\mathbf{x})\phi^{(\alpha)}(\mathbf{x}) d\mathbf{x} \quad \forall \phi \in \mathcal{D}(\Omega). \quad (2.15)$$

If such a w exists, we define $D_w^\alpha v = w$.

One can notice that the new definition of derivative coincides with the old one if the function v is regular enough. The following theorem shows that the smoothness is related to the dimension n and that the weak derivative is a generalization of the classical derivative.

Theorem 2.2.2. *Let α be arbitrary and let $v \in C^{|\alpha|}(\Omega)$. Then the weak derivative $D_w^\alpha v$ exists and is given by $D^\alpha v$.*

2.2.5 Sobolev spaces

Using the notion of weak derivative, we introduce a class of functions as a generalization of the Lebesgue norm and spaces in order to include derivatives. A comprehensive presentation of these spaces can be found in [Adams \[1975\]](#).

Definition 2.2.8. *Let k be a non-negative integer, and let $v \in L^1_{loc}(\Omega)$. Suppose that the weak derivatives $D_w^\alpha v$ exist for all $|\alpha| \leq k$. Define the **Sobolev norm***

$$\|v\|_{W^{k,p}(\Omega)} := \left(\sum_{|\alpha| \leq k} \|D_w^\alpha v\|_{L^p(\Omega)}^p \right)^{1/p} \quad (2.16)$$

in the case $1 \leq p < \infty$, and in the case $p = \infty$

$$\|v\|_{W^{k,\infty}(\Omega)} := \max_{|\alpha| \leq k} \|D_w^\alpha v\|_{L^\infty(\Omega)}. \quad (2.17)$$

In either case, we define the **Sobolev spaces** via

$$W^{k,p}(\Omega) := \{v \in L^1_{loc}(\Omega) : \|v\|_{W^{k,p}(\Omega)} < \infty\}. \quad (2.18)$$

Clearly, for each p , $1 \leq p \leq \infty$, $W^{0,p}(\Omega) = L^p(\Omega)$ and $W^{k_2,p}(\Omega) \subset W^{k_1,p}(\Omega)$ when $k_1 \leq k_2$.

In addition, it is useful to introduce the notation of *semi-norms* for the Sobolev space,

Definition 2.2.9. *For k a non-negative integer and $v \in W_p^k(\Omega)$, let*

$$|v|_{W^{k,p}(\Omega)} = \left(\sum_{|\alpha|=k} \|D_w^\alpha v\|_{L^p(\Omega)}^p \right)^{1/p} \quad (2.19)$$

in the case $1 \leq p < \infty$, and in the case $p = \infty$

$$|v|_{W^{k,\infty}(\Omega)} = \max_{|\alpha|=k} \|D_w^\alpha v\|_{L^\infty(\Omega)}. \quad (2.20)$$

It is clear that $W^{k,p}(\Omega)$ is by definition a normed linear space since $\|\cdot\|_{W^{k,p}(\Omega)}$ satisfies the three properties of the norm definition. The following theorem asserts

2. INTRODUCTION TO FUNCTIONAL ANALYSIS

that the Sobolev spaces are also complete.

Theorem 2.2.3. *The Sobolev space $W^{k,p}(\Omega)$ is a Banach space.*

There is another potential definition of Sobolev space that was proved to be equivalent to the previous one. Let $H^{k,p}(\Omega)$ denote the closure of $C^k(\Omega)$ with respect to the Sobolev norm $\|\cdot\|_{W^{k,p}(\Omega)}$. For $1 \leq p < \infty$ it turns out that $H^{k,p}(\Omega) = W^{k,p}(\Omega)$. Only in the case $p = \infty$ we have $H^{k,p}(\Omega) = C^k(\Omega) \neq W^{k,p}(\Omega)$. The following density result shows an important feature of the Sobolev spaces.

Theorem 2.2.4. *Let Ω be any open set. Then $C^\infty(\Omega) \cap W^{k,p}(\Omega)$ is dense in $W^{k,p}(\Omega)$ for $p < \infty$.*

This result should be separated from another kind of density result, the density of $C^\infty(\bar{\Omega})$ in $W^{k,p}(\Omega)$. In order for this stronger result to hold, a sort of regularity condition must also hold. In fact, if Ω has a Lipschitz continuous boundary, $C^\infty(\bar{\Omega})$ is dense in $W^{k,p}(\Omega)$.

When $p = 2$, mathematicians used to write $H^k(\Omega)$ instead of $W^{k,2}(\Omega)$ and $\|\cdot\|_{k,\Omega}$ instead of $\|\cdot\|_{W^{k,2}(\Omega)}$. We will adopt this notation in the sequel.

It is easy to verify that if we introduce the following scalar product

$$(w, v)_{k,\Omega} := \sum_{|\alpha| \leq k} (D^\alpha w, D^\alpha v)_{0,\Omega}, \quad (2.21)$$

the Sobolev spaces $H^k(\Omega)$ are Hilbert spaces.

Finally, we denote with $W^{-k,p'}(\Omega)$ the dual space of $W_0^{k,p}(\Omega)$. As before, when $p = 2$ we write $H_0^k(\Omega)$ and $H^{-k}(\Omega)$ instead of $W_0^{k,2}(\Omega)$ and $W^{-k,2}(\Omega)$, respectively.

When considering vector-valued functions $\mathbf{v}: \Omega \rightarrow \mathbb{R}^n$, it is useful to introduce the following function space

$$H(\operatorname{div}; \Omega) := \{\mathbf{v} \in (L^2(\Omega))^n \mid \operatorname{div} \mathbf{v} \in L^2(\Omega)\}, \quad (2.22)$$

endowed with the graph norm, i.e.,

$$\|\mathbf{v}\|_{H(\operatorname{div}; \Omega)} := (\|\mathbf{v}\|_{0,\Omega}^2 + \|\operatorname{div} \mathbf{v}\|_{0,\Omega}^2)^{1/2}. \quad (2.23)$$

When considering space-time functions $v(t, \mathbf{x})$, $(t, \mathbf{x}) \in Q_T := (0, T) \times \Omega$, it is natural to define the following space

$$L^q(0, T; W^{k,p}(\Omega)) := \left\{ v : (0, T) \rightarrow W^{k,p}(\Omega) \mid v \text{ is measurable} \right. \\ \left. \text{and } \int_0^T \|v(t)\|_{W^{k,p}(\Omega)}^q dt < \infty \right\}, \quad (2.24)$$

endowed with the norm

$$\|v\|_{L^q(0,T;W^{k,p}(\Omega))} := \left(\int_0^T \|v(t)\|_{W^{k,p}(\Omega)}^q dt \right)^{1/q}, \quad (2.25)$$

and $1 \leq k < \infty$. In an analogous way $L^\infty(0, T; W^{k,p}(\Omega))$ and $C^0(0, T; W^{k,p}(\Omega))$ can be defined.

2.3 Some results about Sobolev spaces

In this Section we present some important properties of functions that belong to Sobolev spaces without reporting any proofs. In particular we will consider only the Hilbert spaces $H^s(\Omega)$. The reader interested to the general case and to the proofs can consult the books of [Lions & Magenes \[1968a,b\]](#) or [Adams \[1975\]](#).

The first step is to give a meaning to the trace on the boundary $\partial\Omega$ of a function $v \in H^s(\Omega)$ because a function that belongs to the Hilbert space $H^s(\Omega)$ is not univocally defined on a manifold having zero measure. This task is accomplished by the following theorem. Let us denote by $C^0(\bar{\Omega})$ the space of continuous functions on $\bar{\Omega}$. The result reads as follows:

Theorem 2.3.1 (Trace theorem). *Let Ω be a bounded open set of \mathbb{R}^n with Lipschitz continuous boundary $\partial\Omega$ and let $k > 1/2$.*

1. *There exists a unique linear continuous map $\gamma_0 : H^k(\Omega) \rightarrow H^{k-1/2}(\partial\Omega)$ such that $\gamma_0 v = v|_{\partial\Omega}$ for each $v \in H^k(\Omega) \cap C^0(\bar{\Omega})$.*
2. *There exists a linear continuous map $\mathcal{R}_0 : H^{k-1/2}(\partial\Omega) \rightarrow H^k(\Omega)$ such that $\gamma_0 \mathcal{R}_0 \phi = \phi$ for each $\phi \in H^{k-1/2}(\partial\Omega)$. Analogous results also hold true if we*

2. INTRODUCTION TO FUNCTIONAL ANALYSIS

consider the trace γ_Σ over a Lipschitz continuous subset Σ of the boundary $\partial\Omega$.

The previous theorem provides a useful characterization of the space $H^{k-1/2}(\Sigma)$ since asserts that any functions that belongs to $H^{k-1/2}(\Sigma)$, $k > 1/2$ is the trace on the boundary Σ of a function in $H^k(\Omega)$.

The previous trace theorem can be extended to vector functions belonging to $H_0(\text{div}; \Omega)$ and reads as follows

Theorem 2.3.2 (Trace theorem for vector functions). *Let Ω be a bounded open set of \mathbb{R}^n with Lipschitz continuous boundary $\partial\Omega$ and let $k > 1/2$.*

1. *There exists a unique linear continuous map $\gamma^*: H(\text{div}; \Omega) \rightarrow H^{-1/2}(\partial\Omega)$ such that $\gamma^* \mathbf{v} = (\mathbf{v} \cdot \mathbf{n})|_{\partial\Omega}$ for each $\mathbf{v} \in H(\text{div}; \Omega) \cap (C^0(\bar{\Omega}))^n$.*
2. *There exists a linear continuous map $\mathcal{R}^*: H^{-1/2}(\partial\Omega) \rightarrow H(\text{div}; \Omega)$ such that $\gamma^* \mathcal{R}^* \phi = \phi$ for each $\phi \in H^{-1/2}(\partial\Omega)$.*

Here we have denoted with \mathbf{n} the unit outward normal vector on $\partial\Omega$. Let us notice that the normal trace of a vector function $\mathbf{v} \in H(\text{div}; \Omega)$ over a subset Σ that is different from the whole boundary $\partial\Omega$ does not belong in general to $H^{-1/2}(\Sigma)$, but to a larger space, which is usually denoted by $H_{00}^{-1/2}(\Sigma)$ (see, e.g., [Lions & Magenes \[1968a\]](#)).

By means of these trace operators it is possible to characterize the spaces $H_0^1(\Omega)$ and $H_0(\text{div}; \Omega) := \overline{(C_0^\infty(\Omega))^n}$ (here the closure must be intended with respect to the norm $\|\cdot\|_{H_0(\text{div}; \Omega)}$). In fact, if the boundary $\partial\Omega$ is Lipschitz continuous we have

$$H_0^1(\Omega) = \{v \in H^1(\Omega) \mid \gamma_0 v = 0\}, \quad H_0(\text{div}; \Omega) = \{\mathbf{v} \in H(\text{div}; \Omega) \mid \gamma^* \mathbf{v} = 0\}.$$

A similar characterization holds for the space

$$H_\Sigma^1(\Omega) := \{v \in H^1(\Omega) \mid \gamma_\Sigma v = 0\}. \quad (2.26)$$

As a consequence of the density of $C^\infty(\bar{\Omega})$ in $H^1(\Omega)$ (under the assumption that the boundary $\partial\Omega$ is Lipschitz continuous), it is easy to prove that for each

$v, w \in H^1(\Omega)$ the following *Green formula* holds

$$\int_{\Omega} (D_j w)v \, d\mathbf{x} = - \int_{\Omega} w D_j v \, d\mathbf{x} + \int_{\partial\Omega} \gamma_0 w \gamma_0 v n_j \, d\gamma, \quad j = 1, \dots, n, \quad (2.27)$$

where we have indicated with D_j the partial derivative $\frac{\partial}{\partial x_j}$.

Similarly, if $\mathbf{w} \in H(\text{div}; \Omega)$ and $v \in H^1(\Omega)$, we have

$$\int_{\Omega} (\text{div } \mathbf{w})v \, d\mathbf{x} = - \int_{\Omega} \mathbf{w} \cdot \nabla v \, d\mathbf{x} + \int_{\partial\Omega} \gamma^* \mathbf{w} \gamma_0 v \, d\gamma. \quad (2.28)$$

Generally, functions in Sobolev spaces $W^{k,p}$ are not so smooth. If some restrictions on the two indices k and p are prescribed, these functions turns out to be regular in according to the following theorem

Theorem 2.3.3 (Sobolev embedding theorem). *Assume that Ω is a (bounded or unbounded) open set of \mathbb{R}^n with Lipschitz continuous boundary, and that $1 \leq p < \infty$. Then the following continuous embeddings hold:*

1. *If $0 \leq kp < n$, then $W^{k,p}(\Omega) \subset L^{p^*}(\Omega)$ for $p^* = np/(n - kp)$;*
2. *If $kp = n$, then $W^{k,p}(\Omega) \subset L^q(\Omega)$ for any q such that $p \leq q < \infty$;*
3. *If $kp > n$, then $W^{k,p}(\Omega) \subset C^0(\bar{\Omega})$.*

The Sobolev embedding theorem states that any function with suitably regular weak derivative turns out to be continuous. In the one-dimensional case ($n = 1$) we have in particular that $H^1(\Omega) \subset C^0(\bar{\Omega})$.

2. INTRODUCTION TO FUNCTIONAL ANALYSIS

Chapter 3

Mathematical Modeling

Every physical phenomena can be described from the mathematical point of view for quantitative and qualitative analysis. This chapter will present the basic principles of continuum mechanics for the mathematical description of fluid flows, solid dynamics and the interaction between the fluid and the solid, namely fluid-structure interaction. The theoretical background presented in this chapter will enable the reader to understand how modeling a FSI problem. The formulation of the physical problem, the Eulerian, Lagrangian and Arbitrary Lagrangian Eulerian (ALE) descriptions and the constitutive equations are presented in the FSI context.

3.1 Overview

In the last decades a great attention has been paid to the study of fluid-structure interaction problems because of a large number of applications ranging from biology to civil engineering and aeroelasticity. In particular, the numerical solution of the equations of fluid-structure interaction is of great interest because of the increasing demand from the medical community for scientifically rigorous and quantitative investigations of cardiovascular diseases. In recent years, the simulation of complex problems in Computational Fluid Dynamics (CFD) has been feasible because of the development of efficient computational techniques and increasing performances of modern computers. However the solution of a fluid-

3. MATHEMATICAL MODELING

structure interaction problem remains a difficult task.

In this work, the problem of an incompressible viscous fluid flow interacting with an incompressible or nearly-incompressible elastic body which is being deformed by the fluid force is considered. Typical engineering problems of this kind can be found in the areas of biomechanics which include the blood flow interaction with elastic veins and cerebral aneurysm hemodynamics or in the field of aeroelasticity.

Nowadays there are not theoretical results providing the well-posedness of the interaction problem between an incompressible Newtonian viscous flow and a hyperelastic material in the general case. This difficulty task was overcome by some authors introducing additional simplifying assumptions such as smallness of the data, linearity, periodic boundary conditions, simple structure model, rigidity of elastic shells or plates (see, e.g., [Beirão da Veiga \[2004\]](#); [Chambolle *et al.* \[2005\]](#); [Coutand & Shkoller \[2005\]](#); [Desjardins & Esteban \[2000\]](#); [Desjardins *et al.* \[2001\]](#); [Grandmont & Maday \[2000\]](#); [Le Tallec & Mani \[2000\]](#); [Rumpf \[1998\]](#)).

In [Le Tallec & Mani \[2000\]](#) a time dependent, linearized model of interaction between a viscous fluid and an elastic shell in small displacement approximation and its discretization is analyzed. The problem is further simplified by neglecting all changes in the geometry configuration. Under these assumptions the authors are able to show that the proposed formulation is well posed and a global weak solution exists by using energy estimates. Further they show that an independent discretization by standard mixed finite elements for the fluid and by nonconforming discrete Kirchhoff triangle finite elements for the shell together with a backward or central difference approximation of the the time derivative converges to the solution of the continuous problem.

In [Beirão da Veiga \[2004\]](#) a rigorous result on the existence of strong solutions to two-dimensional initial-boundary value problems, in which a fluid flow, modeled by the Navier-Stokes equations, interacts with a vessel described by a simple model, the so-called generalized string model, has been established. The mathematical obstacles coming out from the artificial consideration of just a segment of vessel are avoided by considering data and solutions periodic in the “vessel direction”.

In [Grandmont & Maday \[2000\]](#) the well-posedness of an unsteady fluid-structure

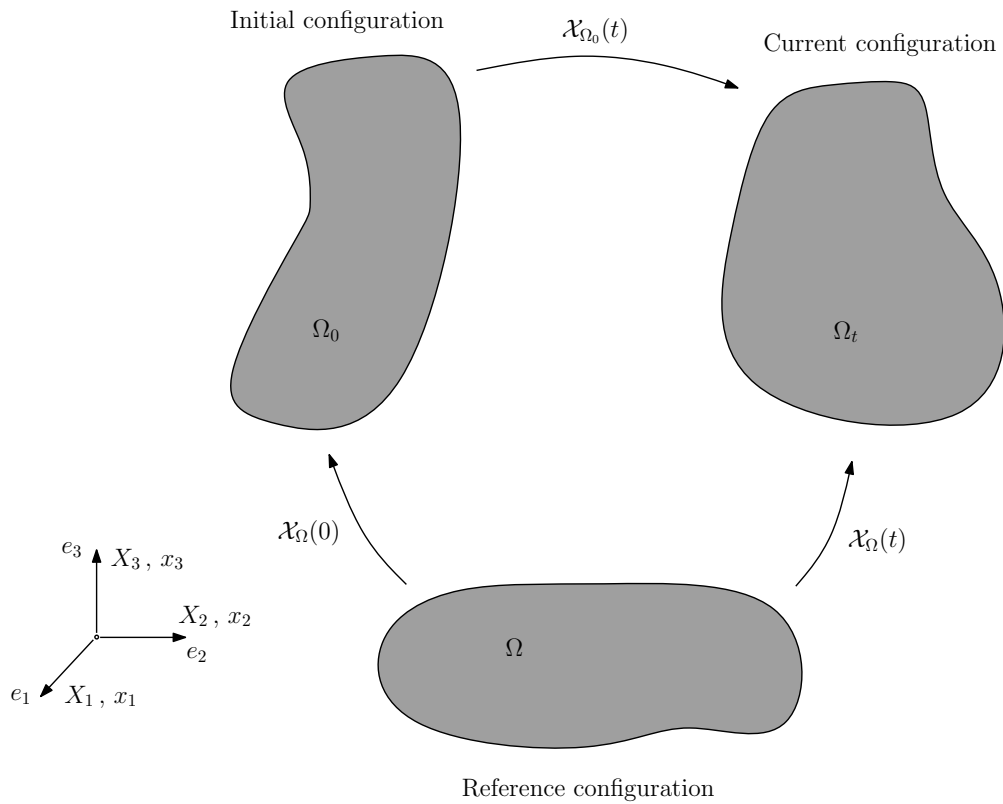


Figure 3.1: Sketch of the referential domain Ω , initial domain Ω_0 and current domain Ω_t and relations between them.

interaction problem has been proved. They consider a viscous incompressible Newtonian fluid, described by the Navier-Stokes equations, interacting with a viscoelastic structure assumed as a collection of rigid moving bodies which position influences the fluid domain.

In [Chambolle *et al.* \[2005\]](#) a three-dimensional viscous incompressible fluid governed by the Navier-Stokes equations, interacting with an elastic plate located on one part of the fluid boundary, is considered. The existence of at least one weak solution for this unsteady fluid-structure interaction problem without any (artificial) viscosity of the structure has been proved.

The basic principles of the continuum theory such as kinematic descriptions and balance laws principles presented in this chapter are based on [Bonet & Wood \[1997\]](#) and [Ciarlet \[1998\]](#). For a basic introduction and a complete reference of continuum theory the reader can see [Haupt \[2000\]](#) and [Gurtin \[1981\]](#).

3.2 Continuum theory

In continuum mechanics, we are interested in the motion and deformations of an elastic body under the action of external and internal forces. The theory of continuum mechanics is a powerful and effective tool for the design of machine elements in engineering. This theory is an approximation of the physical reality because it does not care about the complexity of the internal microscopic structure of a solid object. If the dimension of the solid object is very large compared to the atomic reference length this approximation is good enough for engineers. The basic ideas of continuum mechanics, kinematics, stress and balance laws are presented in the next paragraphs.

3.2.1 Kinematic descriptions

Let $\Omega \subset \mathbb{R}^3$ be a reference (undeformed) configuration of a given body. Let $\Omega_t \subset \mathbb{R}^3$ be a current (deformed) configuration of this object at time t . Let assume that there is a one-to-one, uniquely invertible, sufficiently smooth mapping \mathcal{X}_Ω of the reference (undeformed) configuration Ω to the current (deformed) configuration

$$\mathcal{X}_\Omega : \Omega \times [0, T] \rightarrow \Omega_t,$$

which determines the successive position of the material point, see Figure 3.1. It is clear that the mapping \mathcal{X}_Ω depends on the choice of the reference configuration Ω which can be selected in various ways. All the reference configurations are equivalent but for our purposes it is sufficient to define one of them as the reference configuration. For instance, we can see Ω as the initial (stress-free) configuration. Let us denote an arbitrary material point in the reference configuration Ω by \mathbf{X} . The position of this point at time t is given by

$$\mathbf{x} = \mathcal{X}(\mathbf{X}, t) \quad \mathbf{X} \in \Omega,$$

where \mathbf{x} is the position vector of the point in Ω_t . The mapping \mathcal{X} is called the deformation from Ω to Ω_t . In this context the displacement vector field is a function of time and the material and spatial descriptions are defined respectively

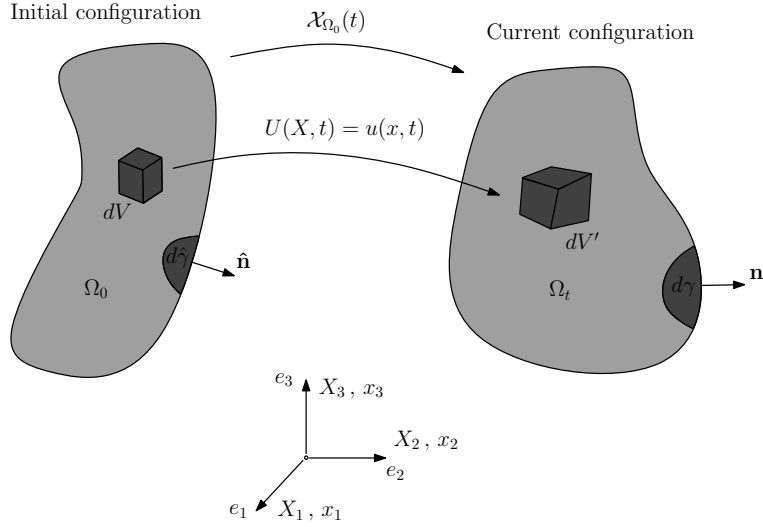


Figure 3.2: Transformation of a material volume under deformation and displacement fields \mathbf{U} and \mathbf{u} of a generic material particle.

as

$$\mathbf{U}(\mathbf{X}, t) = \mathcal{X}(\mathbf{X}, t) - \mathbf{X}, \quad \mathbf{u}(\mathbf{x}, t) = \mathbf{x} - \mathcal{X}^{-1}(\mathbf{x}, t),$$

where $\mathbf{U}(\mathbf{X}, t)$ represents the displacement field of a *material point* (also called *material particle*) identified by \mathbf{X} and relates its position in the reference configuration to the current configuration at time t , while $\mathbf{u}(\mathbf{x}, t)$ is the displacement field in the Eulerian frame. These two physical quantities are related each other using the mapping invertibility hypothesis by the following expression

$$\mathbf{U}(\mathbf{X}, t) = \mathbf{U}(\mathcal{X}^{-1}(\mathbf{x}, t), t) = \mathbf{u}(\mathbf{x}, t).$$

It is known that in solid mechanics the motion and the deformation of a body are described in terms of the displacement field. However, the velocity and the acceleration are involved in the description of the dynamical behavior. The velocity and acceleration fields are defined as the first and second time derivative of the mapping \mathcal{X} respectively

$$\mathbf{v} = \frac{\partial \mathcal{X}}{\partial t}, \quad \mathbf{a} = \frac{\partial^2 \mathcal{X}}{\partial t^2}. \quad (3.1)$$

3. MATHEMATICAL MODELING

3.2.1.1 Configurations

All physical quantities can be defined alternatively on the reference or on the current configuration and the choice is a matter of convenience. We have seen in the previous paragraph that the displacement field can be defined in the reference or in the spatial framework thanks to the invertibility of the mapping.

The interaction between these two “point of view” is essential in continuum mechanics. The transformation between material and spatial regions are typically called *push forward* and *pull back* operations. The push forward means a transformation from the material to the spatial configuration and the pull back means the converse. When we use (\mathbf{X}, t) as independent variables we adopt the *Lagrangian formulation*, while when we refer to the (\mathbf{x}, t) pair we employ the *Eulerian formulation*. In the Lagrangian formulation we follow the evolution of a material particle; in the Eulerian formulation we observe the history of a physical quantity in a given point in the physical space. When a field is expressed in the Eulerian coordinates it is referred to as an *Eulerian field* and when it is expressed in Lagrangian coordinates we call it *Lagrangian field*.

The Eulerian description is well suited to describe the fluid flow through a fixed spatial region. In this case the fluid particles enter and leave the fixed domain of interest. On the other hand the Lagrangian description is well suited to describe the motion a body defined as a fixed collection of material particles. The body can change its shape under the action of external and/or internal forces but not its composition.

3.2.1.2 Lagrangian description

In the Lagrangian description mesh nodes follow the position of the material particles. In other words, the mesh nodes are linked to the same material particle at any time. This approach is mainly used in structural mechanics in the context of finite element method.

Some applications of this approach are, for instance, the metal forming processes and the vehicle crash tests. The drawback of this method is related to the inability in handling strong mesh deformations which results in frequent re-meshing and expensive data projection with loss of accuracy.

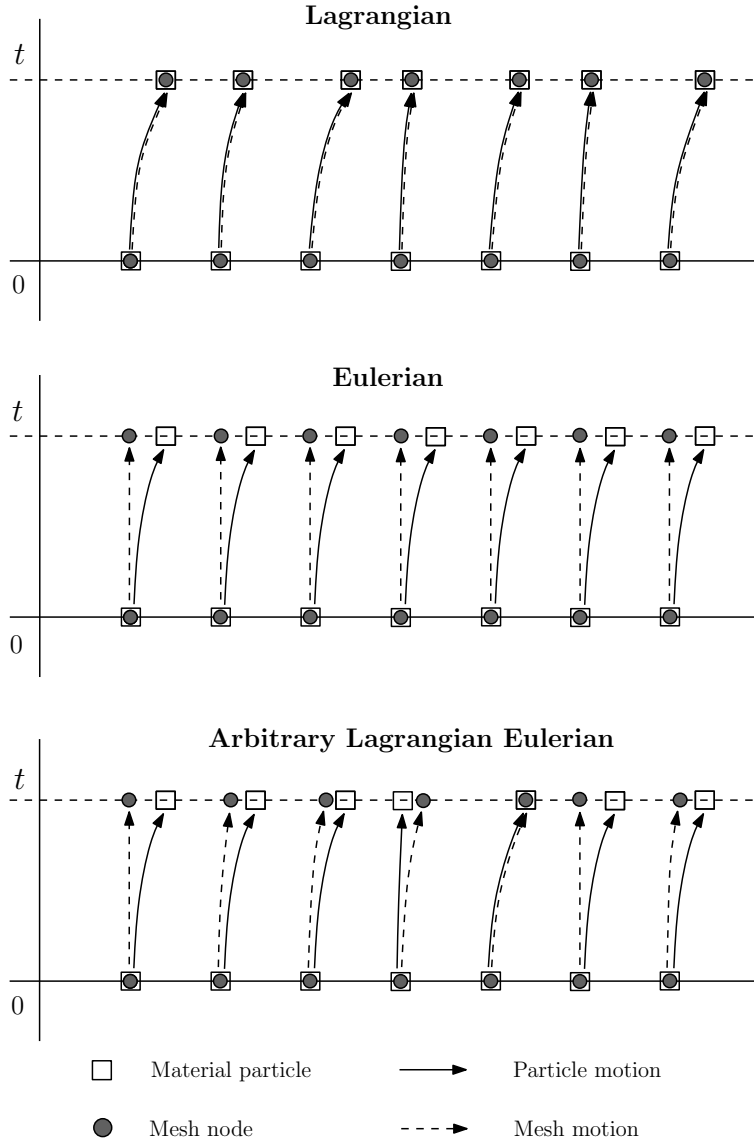


Figure 3.3: Top: 1D Lagrangian description; Middle: 1D Eulerian description; Bottom: 1D ALE (Arbitrary Lagrangian-Eulerian) description.

In the Lagrangian description we consider a physical quantity φ to be defined on the reference configuration Ω as a function of the material coordinate \mathbf{X} and time t :

$$\varphi = \hat{\varphi}(\mathbf{X}, t) : \Omega \times [0, T] \rightarrow Y. \quad (3.2)$$

For the Lagrangian field $\hat{\varphi}$ we define the Lagrangian time-derivative and the

3. MATHEMATICAL MODELING

Lagrangian gradient as simply

$$\frac{d\varphi}{dt} := \frac{\partial \hat{\varphi}}{\partial t}, \quad \nabla \varphi = \frac{\partial \varphi}{\partial \mathbf{X}} := \frac{\partial \hat{\varphi}}{\partial \mathbf{X}}. \quad (3.3)$$

Since the material particles coincide with the same mesh nodes during the motion the negative effects induced by the convective term disappear and the Lagrangian time-derivative reduces to a simple time derivative.

3.2.1.3 Eulerian description

In the Eulerian description the position of the mesh nodes is fixed in time. Material particles move through the fixed region of interest occupying different position at different time while the mesh nodes do not change their position (see Figure 3.3 in 1D). This approach is widely used in fluid mechanics because it is able to handle strong deformation without moving the mesh and it can be used in different context such as finite difference, finite volume and finite element. Structured and unstructured meshes can be used but it is clear that structured meshes are preferable because of fixed nodes, in particular in the finite difference framework. The drawback of this approach is that one has to deal with convective terms that are sources of numerical instability.

Any field quantity φ with values in some vector space Y (i.e. scalar, vector or tensor valued) can be expressed as a function of the spatial position $\mathbf{x} \in \mathbb{R}^3$

$$\varphi = \tilde{\varphi}(\mathbf{x}, t) : \Omega_t \times [0, T] \rightarrow Y. \quad (3.4)$$

For the Eulerian field $\tilde{\varphi}$ we define the Eulerian time-derivative and the Eulerian gradient as simply

$$\frac{\partial \varphi}{\partial t} := \frac{\partial \tilde{\varphi}}{\partial t}, \quad \nabla \varphi = \frac{\partial \varphi}{\partial \mathbf{x}} := \frac{\partial \tilde{\varphi}}{\partial \mathbf{x}}. \quad (3.5)$$

3.2.1.4 Arbitrary Lagrangian Eulerian Description

The Arbitrary Lagrangian Eulerian (ALE) description is an intermediate and more general description that combines the advantages of the Eulerian and Lagrangian approaches. In this description the position of the mesh nodes can be

fixed or can change in time in a prescribed fashion that is independent from the motion of the material particles. After each time step the mesh is updated and the solution is obtained using the most recent mesh configuration.

The Arbitrary Lagrangian Eulerian description was first introduced by Noh [1964] addressing the hydrodynamics problem in the finite difference framework. The method was also used by Hirt *et al.* [1974] and Pracht [1975] for finite difference analysis. In the eighties the method was extended in the finite element context for solving fluid-structure interaction and free surface flows problems by Belytschko (Belytschko [1977]; Belytschko & Kennedy [1976]; Belytschko & Mullen [1981]; Belytschko & Schumann [1980]; Belytschko *et al.* [1982]), Donea (Donea [1983]; Donea *et al.* [1982]), Hughes (Hughes & Tezduyar [1984]; Hughes *et al.* [1981]) and Liu (Liu & Gvildys [1986]; Liu & Ma [1982]). More recently, this approach was applied to nonlinear solid problems and contact problems by Haber [1984], Liu *et al.* [1986], Benson [1984], Ghosh & Kikuchi [1991] and others.

It is known that Eulerian methods are well suited for fluid mechanics while Lagrangian methods for solid mechanics. If our problem deals with the interaction between fluid and solid, like moving walls, or with moving boundaries, this intermediate approach is typically used because exploits the features of both the descriptions.

In fluid-structure interaction problems the fluid flows in a domain with moving boundaries due to the motion of the structure which is affected by the fluid force. In this case the intermediate ALE description is generally used for the fluid part while we can still describe the solid motion in the Lagrangian framework. The fundamental physical quantity describing the motion of the fluid is still the velocity but it is necessary to compute a certain displacement to be defined in order to provide a transformation of the current fluid domain to some fixed reference domain. For these reasons this method is sometimes called *pseudo-solid mapping method*.

In the following, we introduce the basic mathematical concepts of the ALE method and then we provide a relationship among all the three descriptions. In the ALE formulation, a third region $\Omega_{\mathcal{X}}$ is introduced to be the reference configuration, which is in general different from Ω or Ω_t . The mapping $\zeta_{\mathcal{X}}$ from the reference configuration $\Omega_{\mathcal{X}}$ to the Eulerian configuration Ω_t , which represents

3. MATHEMATICAL MODELING

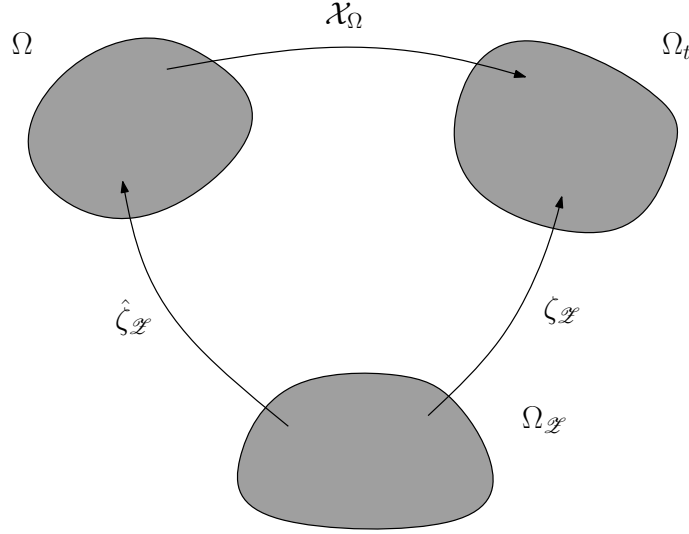


Figure 3.4: The initial domain Ω , the current domain Ω_t , the moving computational domain Ω_x and the relations between them.

the motion of the mesh nodes in the spatial framework, is given by

$$\zeta_x : \mathcal{L} \times [0, T] \rightarrow \mathcal{L}_t, \quad \mathcal{L} \subset \Omega_x, \quad \mathcal{L}_t \subset \Omega_t \quad \forall \in [0, T], \quad (3.6)$$

$$\zeta_x(\mathcal{L}, t) = (\mathbf{x}, t). \quad (3.7)$$

Its gradient is defined as

$$\frac{\partial \zeta_x(\mathcal{L}, t)}{\partial(\mathcal{L}, t)} = \begin{pmatrix} \frac{\partial \mathbf{x}}{\partial \mathcal{L}} & \mathbf{v}_x \\ \mathbf{0}^T & 1 \end{pmatrix} \quad (3.8)$$

where

$$\mathbf{v}_x = \frac{\partial \zeta_x}{\partial t} \quad (3.9)$$

is called *computational domain velocity*, also named *ALE velocity*, and $\mathbf{0}^T$ is a null row-vector. Finally, for the mapping $\hat{\zeta}_x$ from the intermediate ALE configuration to the Lagrangian configuration, we have

$$\hat{\zeta}_x : \mathcal{L} \times [0, T] \rightarrow \mathcal{L}, \quad \mathcal{L} \subset \Omega_x, \quad \mathcal{L} \subset \Omega, \quad \forall \in [0, T], \quad (3.10)$$

$$\hat{\zeta}_x(\mathcal{L}, t) = (\mathbf{X}, t). \quad (3.11)$$

The inverse of the mapping $\hat{\zeta}_{\mathcal{Z}}$ and its gradient are defined as follows

$$(\mathcal{Z}, t) = \hat{\zeta}_{\mathcal{Z}}^{-1}(\mathbf{X}, t), \quad \frac{\partial \hat{\zeta}_{\mathcal{Z}}^{-1}(\mathbf{X}, t)}{\partial(\mathbf{X}, t)} = \begin{pmatrix} \frac{\partial \mathcal{Z}}{\partial \mathbf{X}} & \mathbf{v}_{\mathbf{X}} \\ \mathbf{0}^T & 1 \end{pmatrix}, \quad (3.12)$$

where $\mathbf{v}_{\mathbf{X}} = \frac{\partial \hat{\zeta}_{\mathcal{Z}}^{-1}}{\partial t}$ is defined as the particle velocity in the ALE reference configuration $\Omega_{\mathcal{Z}}$. The material velocity $\mathbf{v} = \frac{\partial \mathbf{x}_{\Omega}}{\partial t}$ and the velocities $\mathbf{v}_{\mathbf{X}}$ and $\mathbf{v}_{\mathcal{Z}}$ previously defined, are related each other by the following expression

$$\mathbf{v} = \mathbf{v}_{\mathcal{Z}} + \frac{\partial \mathbf{x}}{\partial \mathcal{Z}} \cdot \mathbf{v}_{\mathbf{X}}. \quad (3.13)$$

This relation can be attained by differentiating $\mathcal{X}_{\Omega} = \zeta \circ \hat{\zeta}^{-1}$ keeping \mathbf{X} fixed. The relation (3.13) can be rewritten as

$$\mathbf{c} := \mathbf{v} - \mathbf{v}_{\mathcal{Z}} = \frac{\partial \mathbf{X}}{\partial \mathcal{Z}} \cdot \mathbf{v}_{\mathbf{X}}, \quad (3.14)$$

where \mathbf{c} is defined as the relative velocity of the material particle with respect to the mesh, as seen from the spatial region.

Now we can consider three particular cases that we can encounter.

- Pure translation of continuum (i.e. no deformation), $\frac{\partial \mathbf{x}}{\partial \mathcal{Z}} = \mathbf{I}$, which implies $\mathbf{c} = \mathbf{v}_{\mathbf{X}}$.
- The Lagrangian and Eulerian cases can be seen as particular cases of the more general ALE description under the following assumptions:
 - The Lagrangian description, $\hat{\zeta}_{\mathcal{Z}} = \mathbf{I}$ and $\mathbf{X} = \mathcal{Z}$, which implies that material and mesh velocities coincide.
 - The Eulerian description, $\zeta_{\mathcal{Z}} = \mathbf{I}$ and $\mathbf{x} = \mathcal{Z}$, which implies a null mesh velocity $\mathbf{v}_{\mathcal{Z}} = \mathbf{0}$.

The fundamental relation between material time derivatives, ALE referential time derivatives and spatial gradient is the following

$$\frac{df}{dt} = \frac{\partial f}{\partial t} \Big|_{\mathbf{x}} = \frac{\partial f}{\partial t} \Big|_{\mathcal{Z}} + \mathbf{c} \cdot \nabla f = \frac{\partial f}{\partial t} \Big|_{\mathbf{x}} + \mathbf{v} \cdot \nabla f, \quad (3.15)$$

3. MATHEMATICAL MODELING

which can be interpreted in the usual way: the variation of a physical quantity f associated to a given particle \mathbf{X} is the local variation with respect to the ALE reference configuration plus a convective term that takes into account the relative motion of a particle with respect to the ALE reference system. For the material acceleration we have

$$\frac{d\mathbf{v}}{dt} = \frac{\partial\mathbf{v}}{\partial t}\Big|_{\mathbf{x}} = \frac{\partial\mathbf{v}}{\partial t}\Big|_{\mathbf{x}} + \mathbf{v} \cdot \nabla\mathbf{v} = \frac{\partial\mathbf{v}}{\partial t}\Big|_{\mathcal{L}} + \mathbf{c} \cdot \nabla\mathbf{v}. \quad (3.16)$$

In the next section we are going to describe the deformation and strain fields in according to the finite elasticity theory.

3.2.2 Deformation and strain

In the finite elasticity theory a continuum body is said to be deformable if it is able to change its shape under the effects of internal and external forces. An important quantity in the finite elasticity theory is the deformation gradient which is defined as the derivative with respect to the material coordinates of the invertible, twice continuously differentiable map \mathcal{X}

$$\mathbf{F} = \frac{\partial\mathcal{X}}{\partial\mathbf{X}} = \text{Grad}\mathbf{x} = \nabla_{\mathbf{X}}\mathbf{x}. \quad (3.17)$$

Local invertibility of the mapping \mathcal{X} needs that \mathbf{F} be non-singular, which means that $\det\mathbf{F} \neq 0$. The deformation gradient appears into the following equation

$$d\mathbf{x} = \mathbf{F}d\mathbf{X}, \quad (3.18)$$

that give us a measure of how much the infinitesimal line element $d\mathbf{X}$ of material at the point \mathbf{X} transforms linearly into the line element $d\mathbf{x}$ under deformation represented mathematically by the the tensor \mathbf{F} . The determinant of \mathbf{F} , denoted by the symbol $J = \det\mathbf{F}$ and called Jacobian of the transformation, is everywhere strictly positive in order to have an orientation preserving deformation mapping. This property is related to the invertibility of \mathbf{F} . The mathematical condition $J > 0$ is also a physical requirement since volume cannot be negative. The relation between the infinitesimal volume element $d\mathbf{V}$ in the reference configuration Ω and

the infinitesimal volume element $d\mathbf{v}$ of the current configuration is related by

$$d\mathbf{v} = Jd\mathbf{V}. \quad (3.19)$$

The deformation is called *isochoric* or *volume preserving* if $J = \det \mathbf{F} = 1$ and the material that undergoes only isochoric transformation is said to be *incompressible*. The deformation gradient is related to the displacement gradient by the following equations

$$\nabla_{\mathbf{X}} \mathbf{U} = \mathbf{F} - \mathbf{I}, \quad \nabla_{\mathbf{x}} \mathbf{u} = \mathbf{I} - \mathbf{F}^{-1}. \quad (3.20)$$

Now we are going to establish the relation between the infinitesimal surface area element in the material and spatial region. Let $d\mathbf{A} = \mathbf{N}dA$ be a vector surface area element on $\partial\Omega$, where \mathbf{N} is the outward unit normal to the surface, and $d\mathbf{a} = \mathbf{n}da$ the corresponding area element on $\partial\Omega_t$. Then, the area elements in the material and spatial region are related each other by using Nanson's formula:

$$\int_{\partial\Omega_t} \mathbf{n}da = \int_{\partial\Omega} J\mathbf{F}^{-T}\mathbf{N}dA, \quad (3.21)$$

where $\mathbf{F}^{-T} = (\mathbf{F}^{-1})^T$ and $()^T$ is for transpose. Recalling the definition of the cofactor matrix of an invertible matrix \mathbf{A} , $\text{cof}\mathbf{A} = (\det\mathbf{A})\mathbf{A}^{-T}$, we can state the Nanson's theorem on normals:

Theorem 3.2.1 (Nanson's formula). *The measure of a surface element in the reference configuration is related to that of the corresponding element in the current configuration*

$$\mathbf{n}d(\partial\Omega_t) = \text{cof}\mathbf{F}_{\mathcal{X}}\mathbf{N}d(\partial\Omega). \quad (3.22)$$

An important role in this context is played by the *Piola transformation*. Let assume that we have a sufficiently regular second order tensor field $\boldsymbol{\sigma} : \Omega_t \rightarrow \mathbb{R}^{3 \times 3}$ defined on the deformed configuration. The Piola transformation of $\boldsymbol{\sigma}$ associated to the mapping \mathcal{X} is the second order tensor field $\boldsymbol{\Pi} : \Omega \rightarrow \mathbb{R}^{3 \times 3}$ defined over the material configuration as

$$\boldsymbol{\Pi}(\mathbf{X}) = J(\mathbf{X})\boldsymbol{\sigma}(\mathcal{X}(\mathbf{X}))\mathbf{F}^{-T}(\mathbf{X}), \quad (3.23)$$

for every $\mathbf{X} \in \Omega$. The *inverse Piola transformation* of $\boldsymbol{\Pi}$ returns the tensor $\boldsymbol{\sigma}(\mathbf{x})$

3. MATHEMATICAL MODELING

according to

$$\boldsymbol{\sigma}(\mathbf{x}) = J^{-1}(\mathcal{X}^{-1}(\mathbf{x}))\boldsymbol{\Pi}(\mathcal{X}^{-1}(\mathbf{x}))\mathbf{F}^T(\mathcal{X}^{-1}(\mathbf{x})). \quad (3.24)$$

The main property of the Piola transformation is given by the following important theorem

Theorem 3.2.2 (Piola transformation). *Let $\boldsymbol{\sigma}$ be a regular tensor field in Ω and $\boldsymbol{\Pi}$ its Piola transformation, we have*

$$\nabla_{\mathbf{X}} \cdot \boldsymbol{\Pi} = J \nabla \cdot \boldsymbol{\sigma}, \quad (3.25)$$

where $\nabla_{\mathbf{X}}$ is the divergence with respect to the \mathbf{X} coordinates and the equality has to be understood on corresponding points in Ω_t and Ω , respectively.

As a result, by the application of the divergence theorem, we have

$$\int_{\partial\Omega} \boldsymbol{\Pi} \mathbf{N} d(\partial\Omega) = \int_{\partial\Omega_t} \boldsymbol{\sigma} \mathbf{n} d(\partial\Omega_t). \quad (3.26)$$

Also the *Piola identity* will be used

Theorem 3.2.3 (Piola identity).

$$\mathbf{0} = \nabla \cdot (J\mathbf{F}^{-T}) = \nabla \cdot \text{cof}\mathbf{F}. \quad (3.27)$$

Remark 3.2.1. *The results just proved in the theorem 3.22, 3.25 and 3.27 are useful when we will push back the integrals in the conservations equations involving the divergence of a tensor from the current configuration to the reference configuration and viceversa.*

As a general measure of deformation, let consider the change in the scalar product of the two elemental vectors $d\mathbf{X}_1$ and $d\mathbf{X}_2$ as they deform to $d\mathbf{x}_1$ and $d\mathbf{x}_2$. This change involves both the stretching of the elemental vectors and changes of the enclosed angle between the two vectors. Recalling (3.18), the spatial dot scalar product $d\mathbf{x}_1 \cdot d\mathbf{x}_2$ is related to the correspondent material vectors $d\mathbf{X}_1$ and $d\mathbf{X}_2$ as

$$d\mathbf{x}_1 \cdot d\mathbf{x}_2 = d\mathbf{X}_1 \cdot \mathbf{C} \cdot d\mathbf{X}_2, \quad (3.28)$$

where \mathbf{C} is the *right Cauchy-Green deformation tensor*, which is given in terms of the deformation gradient as

$$\mathbf{C} = \mathbf{F}^T \mathbf{F}. \quad (3.29)$$

Note that since the tensor \mathbf{C} operates on the material vectors $d\mathbf{X}_1$ and $d\mathbf{X}_2$, this tensor is called a material tensor quantity. If the deformation map \mathcal{X} describes a rigid body rotation, the deformation gradient is represented by a rotation tensor \mathbf{Q} . Since a rotation tensor is described by an orthogonal matrix, the Cauchy-Green strain tensor \mathbf{C} coincides with the identity matrix:

$$\mathbf{C} = \mathbf{F}^T \mathbf{F} = \mathbf{Q}^T \mathbf{Q} = \mathbf{Q}^{-1} \mathbf{Q} = \mathbf{I}. \quad (3.30)$$

Alternatively, the initial material scalar product $d\mathbf{X}_1 \cdot d\mathbf{X}_2$ can be obtained in terms of the spatial vectors $d\mathbf{x}_1$ and $d\mathbf{x}_2$ via the *left Cauchy-Green deformation tensor* \mathbf{b} as

$$d\mathbf{X}_1 \cdot d\mathbf{X}_2 = d\mathbf{x}_1 \cdot \mathbf{b}^{-1} \cdot d\mathbf{x}_2, \quad (3.31)$$

where \mathbf{b} is

$$\mathbf{b} = \mathbf{F} \mathbf{F}^T. \quad (3.32)$$

Note that since the tensor \mathbf{b}^{-1} operates on the spatial vectors $d\mathbf{x}_1$ and $d\mathbf{x}_2$, \mathbf{b}^{-1} or \mathbf{b} itself, is called a material tensor quantity.

The change in scalar product can be found in terms of the material vectors $d\mathbf{X}_1$ and $d\mathbf{X}_2$ and the *Lagrangian* or *Green strain tensor* \mathbf{E} as

$$\frac{1}{2}(d\mathbf{x}_1 \cdot d\mathbf{x}_2 - d\mathbf{X}_1 \cdot d\mathbf{X}_2) = d\mathbf{X}_1 \cdot \mathbf{E} \cdot d\mathbf{X}_2, \quad (3.33)$$

where the material tensor \mathbf{E} is

$$\mathbf{E} = \frac{1}{2}(\mathbf{C} - \mathbf{I}). \quad (3.34)$$

Observe that this tensor vanishes for unstrained material since $\mathbf{C} = \mathbf{I}$ if no deformations are involved. Therefore the Green strain tensor \mathbf{E} represents the natural strain measure. The Green strain tensor \mathbf{E} can also be written in terms of dis-

3. MATHEMATICAL MODELING

placements as

$$\mathbf{E} = \frac{1}{2}(\nabla \mathbf{u} + \nabla \mathbf{u}^T + \nabla \mathbf{u}^T \nabla \mathbf{u}). \quad (3.35)$$

Alternatively, the same change in scalar product can now be found in terms of the spatial vectors $d\mathbf{x}_1$ and $d\mathbf{x}_2$ and the *eulerian* or *Almansi strain tensor* \mathbf{e}

$$\frac{1}{2}(d\mathbf{x}_1 \cdot d\mathbf{x}_2 - d\mathbf{X}_1 \cdot d\mathbf{X}_2) = d\mathbf{x}_1 \cdot \mathbf{e} \cdot d\mathbf{x}_2, \quad (3.36)$$

where the material tensor \mathbf{e} is

$$\mathbf{e} = \frac{1}{2}(\mathbf{I} - \mathbf{b}^{-1}). \quad (3.37)$$

3.2.3 Stress tensors

Consider a general deformable body at its current position as shown in 3.5. In order to develop the concept of stress it is necessary to study the action of the forces applied by one region R_1 of the body on the remaining part R_2 of the body with which is in contact. These forces are called *interior forces* or *contact forces* and they are due to the mutual interaction of particles. For this purpose consider the element of area Δa of normal \mathbf{n} in the neighborhood of spatial point P as shown 3.5. If the resultant force on this area is $\Delta \mathbf{f}$, the stress vector \mathbf{t} corresponding to the normal \mathbf{n} at P is defined as

$$\mathbf{t}(\mathbf{n}) = \lim_{\Delta a \rightarrow 0} \frac{\Delta \mathbf{f}}{\Delta a}, \quad (3.38)$$

where the relationship between \mathbf{t} and \mathbf{n} must be such that satisfies Newton third's law of action and reaction, which is expressed as

$$\mathbf{t}(-\mathbf{n}) = -\mathbf{t}(\mathbf{n}). \quad (3.39)$$

A fundamental result, given by the Cauchy theorem, states that the stress vector \mathbf{t} at a point P of a surface depends only through the normal direction of the surface at P.

Theorem 3.2.4 (Cauchy Theorem). *Continuum mechanics is based on three fundamental assumptions concerning the interior forces:*

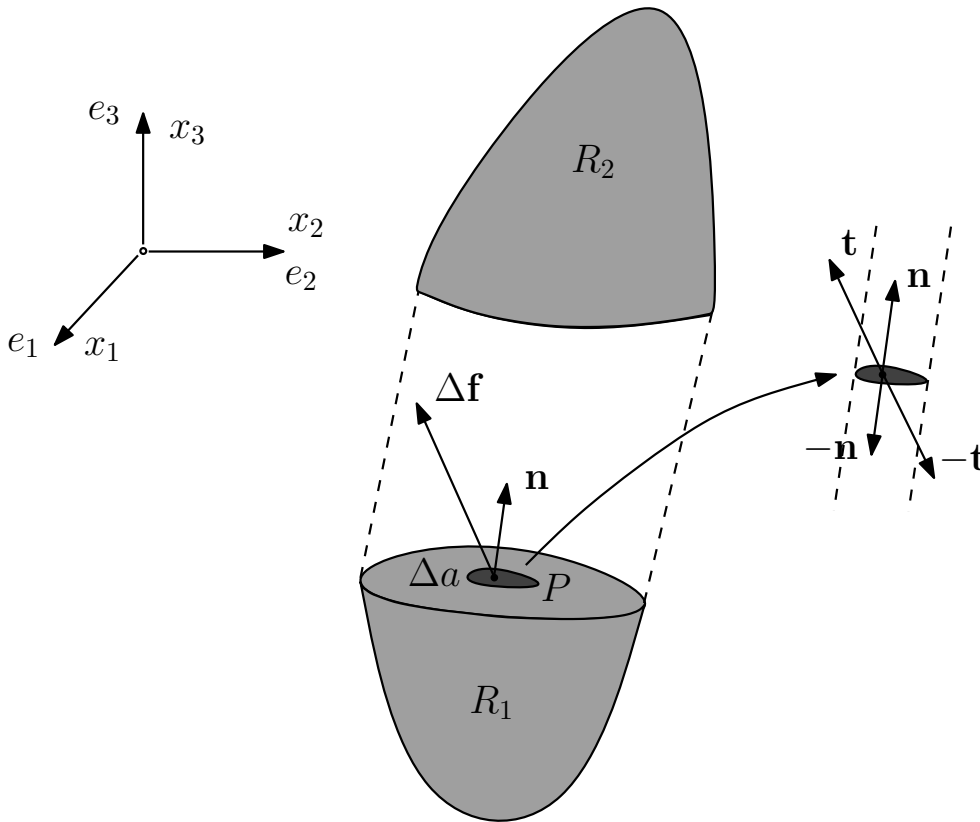


Figure 3.5: Traction vector.

- interior forces act via the surface of a volume (i.e. the surface Δa of the volume R_1),
- interior forces only depend on the normal direction of the surface of the volume,
- interior forces are additive and continuous.

Due to the Cauchy theorem these assumptions imply that the interior forces must be of the form

$$\mathbf{t}(\mathbf{n}) = \boldsymbol{\sigma} \mathbf{n}, \quad (3.40)$$

where $\boldsymbol{\sigma}$ is called Cauchy stress tensor which is independent of \mathbf{n} .

3. MATHEMATICAL MODELING

Cauchy stress tensor can be written in matrix form

$$\boldsymbol{\sigma} = \begin{pmatrix} \sigma_{11} & \sigma_{12} & \sigma_{13} \\ \sigma_{21} & \sigma_{22} & \sigma_{23} \\ \sigma_{31} & \sigma_{32} & \sigma_{33} \end{pmatrix} = \begin{pmatrix} \sigma_x & \tau_{xy} & \tau_{xz} \\ \tau_{yx} & \sigma_y & \tau_{yz} \\ \tau_{zx} & \tau_{zy} & \sigma_z \end{pmatrix}, \quad (3.41)$$

where σ_x , σ_y and σ_z are normal stresses, and τ_{xy} , τ_{xz} , σ_{yx} , σ_{yz} , σ_{zx} and σ_{zy} are shear stresses. For 2D computations we consider only plane stress approximation.

In finite deformation problems care must be taken to the choice of the configuration to which stress is measured. The Cauchy stress is a symmetric measure of stress defined with respect to the current configuration. Cauchy stress is often used to define general constitutive equations for material. The *second Piola-Kirchhoff* stress \mathbf{S} is a symmetric stress measure with respect to the reference configuration and is related to the Cauchy stress tensor through the deformation gradient as

$$\mathbf{S} = J\mathbf{F}^{-1}\boldsymbol{\sigma}\mathbf{F}^{-T}. \quad (3.42)$$

Finally, one can introduce the (unsymmetric) *first Piola-Kirchhoff* stress \mathbf{P} , which is related to \mathbf{S} by the relation $\mathbf{P} = \mathbf{F}\mathbf{S}$.

Because the Cauchy stress tensor plays an important role in any equilibrium equation, it is important to inquire whether $\boldsymbol{\sigma}$ is objective. An objective quantity is a quantity that is independent of the observer, i.e., with respect to different frames. For this purpose let consider the transformations of the normals and internal forces \mathbf{t} implied by the superimposed rigid body rotation \mathbf{Q} as

$$\tilde{\mathbf{t}}(\tilde{\mathbf{n}}) = \mathbf{Q}\mathbf{t}(\mathbf{n}), \quad \tilde{\mathbf{n}} = \mathbf{Q}\mathbf{n}. \quad (3.43)$$

Using the relationship between force and stress tensor given by (3.40) in conjunction with the above equation gives

$$\tilde{\boldsymbol{\sigma}} = \mathbf{Q}\boldsymbol{\sigma}\mathbf{Q}^T. \quad (3.44)$$

The above equation conforms with the definition of objectivity, hence $\boldsymbol{\sigma}$ is a valid candidate for inclusion in a material description.

3.3 Balance Laws

In this section we will formulate the balance equations for mass and momentum in three forms: the Eulerian, the Lagrangian and the arbitrary Eulerian-Lagrangian (ALE) description. The balance equation for energy is reported at end of this paragraph for reasons of completeness. We assume in our simulations that the fluid-structure interaction process is isothermal and that the energy balance equation is always satisfied.

For the formulation of the balance laws we will need to handle a time derivative of some integrals which support changes in time. The following theorems will be useful for our purposes.

An interesting property of the Jacobian J is that its time derivative is linked to the divergence of the velocity field \mathbf{v} .

Theorem 3.3.1. *Let J denote the Jacobian in the Eulerian frame. We have the relation*

$$\frac{d}{dt}J = J\nabla \cdot \mathbf{v}, \quad (3.45)$$

sometimes called the Eulerian expansion formula.

This theorem allows to obtain the following fundamental result.

Theorem 3.3.2 (Reynolds transport formula). *Let Ω_t be a material domain, i.e. $\Omega_t = \{\mathbf{x} : \mathbf{x} = \mathcal{X}(\mathbf{X}, t), \mathbf{X} \in \Omega\}$. The following transport theorem holds for all differentiable mapping φ*

$$\frac{d}{dt} \int_{\Omega_t} \varphi d\mathbf{v} = \int_{\Omega_t} \left(\frac{\partial \varphi}{\partial t} + \nabla \cdot (\varphi \mathbf{v}) \right) d\mathbf{v}. \quad (3.46)$$

When working with the ALE formulation it will be useful to consider the *Reynolds formula* acting on the moving computational domain.

Theorem 3.3.3 (ALE Reynolds transport formula). *Let $\mathcal{L}_0 \subset \mathcal{L}$ be a subdomain in the ALE reference configuration and $\mathcal{L}_{0,t} = \{\mathbf{x} : \mathbf{x} = \mathcal{A}(\tilde{\mathbf{x}}, t), \tilde{\mathbf{x}} \in \mathcal{L}_0\}$. Clearly, $\mathcal{L}_{0,t}$ is always contained in the computational domain \mathcal{L}_t . The following transport*

3. MATHEMATICAL MODELING

theorem holds for all differentiable mapping φ

$$\frac{d}{dt} \int_{\mathcal{Z}_{0,t}} \varphi d\mathbf{v} = \int_{\mathcal{Z}_{0,t}} \left(\frac{\partial \varphi}{\partial t} + \nabla \cdot (\varphi \mathbf{v}_{\mathcal{Z}}) \right) d\mathbf{v}. \quad (3.47)$$

Here $\mathbf{v}_{\mathcal{Z}}$ indicates the domain velocity.

Another important result is the *Gauss Divergence Theorem* that allows to transform a volume integral into a surface integral.

Theorem 3.3.4 (Gauss Divergence Theorem). *The Gauss divergence theorem states that for all differentiable mapping φ*

$$\int_{\Omega_t} \nabla \cdot (\varphi \mathbf{v}) d\mathbf{v} = \int_{\partial\Omega_t} \varphi \mathbf{v} \cdot \mathbf{n} da. \quad (3.48)$$

3.3.1 Balance of mass

The mass m of a fixed region $V \subset \mathbb{R}^3$ in space with boundary ∂V is

$$m = \int_V \rho(\mathbf{x}, t) d\mathbf{v}, \quad V \subset \Omega_t, \quad \forall t > 0, \quad (3.49)$$

where $\rho(\mathbf{x}, t)$ is the Eulerian material density. The arbitrary volume V is the control volume which is independent of time. The fundamental principle of conservation of mass states that the mass inside the control volume does not change in time. Then the balance of mass in the region V can be written as

$$\frac{dm}{dt} = \frac{d}{dt} \int_V \rho(\mathbf{x}, t) d\mathbf{v} = 0, \quad \forall t > 0. \quad (3.50)$$

Equation (3.50) is also known as conservation of mass in integral form. Making use of the Reynolds transport formula (3.46) it becomes

$$\frac{\partial}{\partial t} \int_V \rho d\mathbf{v} + \frac{\partial}{\partial t} \int_{\partial V} \rho \mathbf{v} \cdot \mathbf{n} da = 0. \quad (3.51)$$

After applying the Gauss divergence theorem we obtain

$$\int_V \left(\frac{\partial \rho}{\partial t} + \nabla \cdot (\rho \mathbf{v}) \right) d\mathbf{v} = 0, \quad \forall t > 0, \quad (3.52)$$

which is the global (integral) form of the conservation of mass with respect to the current configuration. If all the fields are sufficiently smooth this equation can be written in local (differential) form with respect to the same configuration as

$$\frac{\partial \rho}{\partial t} + \nabla \cdot (\rho \mathbf{v}) = 0. \quad (3.53)$$

If the fluid has *constant density* we recover the well known *incompressibility equation*

$$\nabla \cdot \mathbf{v} = 0. \quad (3.54)$$

It will be useful to obtain the mass balance equation in the Lagrangian frame. Let $\hat{V} \subset \Omega$ be a fixed set of particles. Mapping back the continuity equation in integral form (3.50) to the reference domain we obtain

$$\frac{d}{dt} \int_{\hat{V}} J \rho d\mathbf{V} = \int_{\hat{V}} \frac{\partial(J\rho)}{\partial t} d\mathbf{V} = 0. \quad (3.55)$$

If we set

$$\rho_0 = J\rho, \quad (3.56)$$

from the arbitrariness of \hat{V} and smoothness of the density and of the Jacobian we derive the continuity equation in the Lagrangian frame, namely

$$\frac{\partial}{\partial t} \rho_0 = 0, \quad \text{in } \Omega, \quad \forall t > 0. \quad (3.57)$$

In the case of arbitrary Lagrangian-Eulerian description we take a region $\mathcal{Z} \in \mathbb{R}^3$ which is itself moving independently of the motion of the body. Let the motion of the control region \mathcal{Z} be described by a given mapping

$$\zeta_{\mathcal{Z}} : \mathcal{Z} \times [0, T] \rightarrow \mathcal{Z}_t, \quad \mathcal{Z}_t \subset \Omega_t, \quad \forall t \in [0, T], \quad (3.58)$$

with the corresponding velocity $\mathbf{v}_{\mathcal{Z}} = \frac{\partial \zeta_{\mathcal{Z}}}{\partial t}$, deformation gradient $\mathbf{F}_{\mathcal{Z}} = \frac{\partial \zeta_{\mathcal{Z}}}{\partial \mathbf{X}}$ and its determinant $J_{\mathcal{Z}} = \det \mathbf{F}_{\mathcal{Z}}$. The balance equation in the ALE global formulation can be written as

$$\frac{\partial}{\partial t} \int_{\mathcal{Z}_t} \rho d\mathbf{v} + \int_{\partial \mathcal{Z}_t} \rho (\mathbf{v} - \mathbf{v}_{\mathcal{Z}}) \cdot \mathbf{n} da = 0. \quad (3.59)$$

3. MATHEMATICAL MODELING

This equation can be alternatively viewed as an Eulerian description with moving spatial coordinate system. In order to obtain a local form of the balance equation, we need to push back the integrals to the fixed region \mathcal{Z}

$$\frac{\partial}{\partial t} \int_{\mathcal{Z}} \rho J_{\mathcal{Z}} d\mathbf{v} + \int_{\partial\mathcal{Z}} \rho (\mathbf{v} - \mathbf{v}_{\mathcal{Z}}) \cdot \mathbf{F}_{\mathcal{Z}}^{-T} \mathbf{n} J_{\mathcal{Z}} d\mathbf{a} = 0, \quad (3.60)$$

then the local form is

$$\frac{\partial}{\partial t} (\rho J_{\mathcal{Z}}) + \nabla \cdot (\rho J_{\mathcal{Z}} (\mathbf{v} - \mathbf{v}_{\mathcal{Z}}) \mathbf{F}_{\mathcal{Z}}^{-T}) = 0. \quad (3.61)$$

If the fluid has constant density and is motionless, (3.61) is reduced to

$$\frac{\partial}{\partial t} (J_{\mathcal{Z}}) - \nabla \cdot (J_{\mathcal{Z}} \mathbf{v}_{\mathcal{Z}} \mathbf{F}_{\mathcal{Z}}^{-T}) = 0, \quad (3.62)$$

which is an identity that is valid for every reference configuration we choose. By using (3.62) and the constant density hypothesis, we get from (3.61)

$$\nabla \cdot (J_{\mathcal{Z}} \mathbf{v}_{\mathcal{Z}} \mathbf{F}_{\mathcal{Z}}^{-T}) = 0. \quad (3.63)$$

By applying (3.27) to (3.63) we have

$$J_{\mathcal{Z}} \nabla \mathbf{v} : \mathbf{F}_{\mathcal{Z}}^{-T} = 0. \quad (3.64)$$

At this point, we can show that the balance of mass in the Eulerian and Lagrangian frame can be recovered from the more general balance of mass in the ALE frame. If the region \mathcal{Z} is fixed in space, i.e. $\mathcal{Z} = \mathcal{Z}_t, \forall t \in [0, T]$, then $\zeta_{\mathcal{Z}}$ is the identity mapping, $\mathbf{F}_{\mathcal{Z}} = \mathbf{I}$, $J_{\mathcal{Z}} = 1$, $\mathbf{v}_{\mathcal{Z}} = \mathbf{0}$, and (3.61) reduces to (3.53). Alternatively, if the region \mathcal{Z} moves exactly as the material, i.e. $\zeta_{\mathcal{Z}} = \mathcal{X}$, $\mathbf{F}_{\mathcal{Z}} = \mathbf{F}$, $J_{\mathcal{Z}} = J$, $\mathbf{v}_{\mathcal{Z}} = \mathbf{v}$, and (3.61) reduces to (3.57).

3.3.2 Balance of Momentum

The conservation of momentum is in fact the well known second Newton's law. This principle states that the rate of change of the momentum of a material domain $V(t)$, given by $\int_{V(t)} \rho \mathbf{v} d\mathbf{v}$, is equal to the resultant of the external forces

acting on it, i.e.

$$\frac{d}{dt} \int_{V(t)} \rho \mathbf{v} d\mathbf{v} = \mathbf{F}_v + \mathbf{F}_s, \quad (3.65)$$

where \mathbf{F}_v is the resultant of the volume forces and \mathbf{F}_s is the resultant of the surface forces. The former acts on the whole domain $V(t)$ (e.g. the gravity force) and can be expressed as the integral of the density multiplied by a specific force (i.e. force per unit of weight) which has dimension of an acceleration. The latter is instead responsible of the mutual interaction between the material particles contained in $V(t)$ and the exterior through the boundary $\partial V(t)$. To be precise, \mathbf{F}_s is equal to the integral over the external surface $\partial V(t)$ of the Cauchy stress \mathbf{t} previously defined, that is

$$\mathbf{F}_s = \int_{\partial V(t)} \mathbf{t} da. \quad (3.66)$$

The momentum conservation law can then be expressed by the following equation, valid for all material domains $V(t)$

$$\frac{d}{dt} \int_{V(t)} \rho \mathbf{v} d\mathbf{v} = \int_{V(t)} \rho \mathbf{f} d\mathbf{v} + \int_{\partial V(t)} \boldsymbol{\sigma} \mathbf{n} da = \int_{V(t)} \rho \mathbf{f} d\mathbf{v} + \int_{V(t)} \nabla_{\mathbf{x}} \cdot \boldsymbol{\sigma} d\mathbf{v}, \quad (3.67)$$

where we have used the divergence theorem to obtain the last equality. By exploiting the Reynolds transport formula we obtain the balance of momentum in conservation form

$$\int_{V(t)} \frac{\partial \rho \mathbf{v}}{\partial t} d\mathbf{v} + \int_{V(t)} \nabla \cdot (\rho \mathbf{v} \otimes \mathbf{v}) d\mathbf{v} = \int_{V(t)} \nabla \cdot \boldsymbol{\sigma} d\mathbf{v} + \int_{V(t)} \rho \mathbf{f} d\mathbf{v}, \quad (3.68)$$

where the symbol \otimes indicates the diadic product. If all fields in (3.68) are sufficiently smooth, by making use of (3.53) and the arbitrariness of $V(t)$, the local formulation of the balance of momentum in the Eulerian frame can be obtained from (3.68) as

$$\rho \frac{\partial \mathbf{v}}{\partial t} + \rho (\mathbf{v} \cdot \nabla) \mathbf{v} = \nabla \cdot \boldsymbol{\sigma} + \rho \mathbf{f} \quad \text{in } \Omega_t, \quad t > 0. \quad (3.69)$$

The momentum equation in integral form (3.67) can also be rewritten in the Lagrangian frame by mapping all integrals back on the reference domain Ω to

3. MATHEMATICAL MODELING

obtain

$$\frac{d}{dt} \int_{\Omega} \rho J \mathbf{v} d\mathbf{v} = \int_{\Omega} J \nabla_{\mathbf{x}} \cdot \boldsymbol{\sigma} d\mathbf{v} + \int_{\Omega} \rho J \mathbf{f} d\mathbf{v}. \quad (3.70)$$

Yet, thanks to (3.56) and (3.57) we have

$$\frac{d}{dt} \int_{\Omega} \rho J \mathbf{v} d\mathbf{v} = \int_{\Omega} \rho_0 \frac{\partial \mathbf{v}}{\partial t} d\mathbf{v} \quad (3.71)$$

Thus, by considering the arbitrariness of Ω and (3.71) we obtain the following differential equation

$$\rho_0 \frac{\partial \mathbf{v}}{\partial t} = J \nabla_{\mathbf{x}} \cdot \boldsymbol{\sigma} + \rho_0 \mathbf{f} \quad \text{in } \Omega, \quad t > 0. \quad (3.72)$$

This form is still not satisfactory because the divergence is still taken with respect to the spatial coordinates \mathbf{x} . If we use the Piola transform (3.25) we get

$$\rho_0 \frac{\partial \mathbf{v}}{\partial t} = \nabla \cdot \mathbf{P} + \rho_0 \mathbf{f} \quad \text{in } \Omega, \quad t > 0, \quad (3.73)$$

where \mathbf{P} is the first Piola-Kirchhoff stress tensor.

In the arbitrary Lagrangian-Eulerian formulation, by using the ALE Reynolds transport formula (3.47), the balance of momentum is given by

$$\begin{aligned} \frac{d}{dt} \int_{\mathcal{Z}_t} \rho \mathbf{v} d\mathbf{v} + \int_{\mathcal{Z}_t} \nabla_{\mathbf{x}} \cdot (\rho \mathbf{v} \otimes (\mathbf{v} - \mathbf{v}_{\mathcal{Z}})) d\mathbf{v} = \\ \int_{\mathcal{Z}_t} \nabla_{\mathbf{x}} \cdot \boldsymbol{\sigma} d\mathbf{v} + \int_{\mathcal{Z}_t} \rho \mathbf{f} d\mathbf{v}, \end{aligned} \quad (3.74)$$

where \mathcal{Z}_t is the image by the ALE map $\zeta_{\mathcal{Z}}$ of a subdomain in the ALE reference configuration. The momentum equation in integral form (3.74) can also be rewritten in the ALE frame by mapping all integrals back on the reference domain $\Omega_{\mathcal{Z}}$ making use of the Piola-Kirchhoff theorem to obtain

$$\begin{aligned} \int_{\mathcal{Z}} \frac{\partial \rho J_{\mathcal{Z}} \mathbf{v}}{\partial t} d\mathbf{v} + \int_{\mathcal{Z}} \nabla \cdot (\rho J_{\mathcal{Z}} \mathbf{v} \otimes (\mathbf{v} - \mathbf{v}_{\mathcal{Z}}) \mathbf{F}_{\mathcal{Z}}^{-T}) d\mathbf{v} = \\ \int_{\mathcal{Z}} \nabla \cdot (J_{\mathcal{Z}} \boldsymbol{\sigma} \mathbf{F}_{\mathcal{Z}}^{-T}) d\mathbf{v} + \int_{\mathcal{Z}} \rho J_{\mathcal{Z}} \mathbf{f} d\mathbf{v}, \end{aligned} \quad (3.75)$$

which in the conservative local form gives

$$\frac{\partial \rho J_{\mathcal{X}} \mathbf{v}}{\partial t} + \nabla \cdot (\rho J_{\mathcal{X}} \mathbf{v} \otimes (\mathbf{v} - \mathbf{v}_{\mathcal{X}}) \mathbf{F}_{\mathcal{X}}^{-T}) = \nabla \cdot (J_{\mathcal{X}} \boldsymbol{\sigma} \mathbf{F}_{\mathcal{X}}^{-T}) + \rho J_{\mathcal{X}} \mathbf{f}. \quad (3.76)$$

Using Eq. (3.61) the momentum balance equation can also be written in the non-conservative local form as

$$\rho J_{\mathcal{X}} \frac{\partial \mathbf{v}}{\partial t} + \rho J_{\mathcal{X}} (\nabla \mathbf{v}) \mathbf{F}_{\mathcal{X}}^{-1} (\mathbf{v} - \mathbf{v}_{\mathcal{X}}) = \nabla \cdot (J_{\mathcal{X}} \boldsymbol{\sigma} \mathbf{F}_{\mathcal{X}}^{-T}) + \rho J_{\mathcal{X}} \mathbf{f}. \quad (3.77)$$

3.3.3 Balance of Angular Momentum

For the angular momentum balance we assume that there are no external or internal sources of angular momentum, then it follows that the Cauchy stress tensor has to be symmetric, i.e.

$$\boldsymbol{\sigma} = \boldsymbol{\sigma}^T. \quad (3.78)$$

3.3.4 Balance of Energy

Denoting the total energy per mass as $E = e + \frac{1}{2}|\mathbf{v}|^2$, where e be the internal energy per unit of mass, \mathbf{q} be the heat flux per unit of area, r be the heat source per unit of mass. Then, the balance of energy states that the change of total energy of a material region V is equal to the heat generated into the system and the heat that enters the system through the boundary, that is

$$\frac{d}{dt} \int_{V(t)} \rho E d\mathbf{v} = \int_{V(t)} (\rho \mathbf{f} \cdot \mathbf{v} + \rho r) d\mathbf{v} + \int_{\partial V(t)} (\boldsymbol{\sigma} \mathbf{v} - \mathbf{q}) \cdot \mathbf{n} da. \quad (3.79)$$

Making use of the mass and momentum balance equations (3.53) and (3.69), the Reynolds transport formula and the arbitrariness of the volume $V(t)$, the equation for the conservation of energy in local form in the Eulerian frame becomes

$$\frac{\partial \rho e}{\partial t} + \nabla \cdot (\rho e \mathbf{v}) = \boldsymbol{\sigma} : \nabla \mathbf{v} - \nabla \cdot \mathbf{q} + \rho r. \quad (3.80)$$

3. MATHEMATICAL MODELING

3.4 Fluid Structure Interaction problem formulation

In this paragraph we are going to introduce the fluid-structure interaction problem formulation together with some few assumptions that allow us to deal with more appropriately. We consider a mechanical system composed by a laminar fluid and a solid occupying a moving domain Ω_t . In the rest of this work we will use the superscripts s and f to denote quantities that belong to solid and fluid, respectively. The description of the mechanical interaction between fluid and solid is given in terms of the classical conservation laws of continuum mechanics showed in the previous paragraph, endowed with the appropriate constitutive equations and boundary conditions at the interface. The fluid equations will be formulated in the ALE frame while the solid equations in the Lagrangian frame. Let assume that both solid and fluid are incompressible, which is a well accepted approximation in biomechanics. In addition we assume that all physical processes are isothermal, which means that the temperature of the system is constant everywhere. This approximation is also well accepted for many biomechanical problems. The advantage of this approximation relies on the fact that we do not need to solve the energy equation.

3.4.1 Continuum description

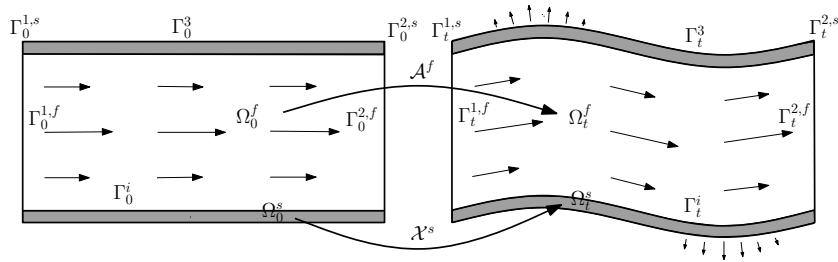


Figure 3.6: Undeformed (reference) and deformed (current) configurations of a system in which a vessel wall interacts with a fluid.

Let Ω_t^f and Ω_t^s be the region occupied by the fluid and the solid at the time $t \in (0, T]$, respectively. At the time $t = 0$ the fluid and solid region are therefore

defined by Ω_0^f and Ω_0^s . Let $\Gamma_t^i = \Omega_t^f \cap \Omega_t^s$ and $\Gamma_0^i = \Omega_0^f \cap \Omega_0^s$ be the interface where solid and fluid interact and $\Gamma_t^k, k = 1, 2, 3$ and $\Gamma_0^k, k = 1, 2, 3$ be the remaining external boundaries at the time $t \in (0, T]$ and $t = 0$, respectively. The evolution of the domain $\Omega_t = \Omega_t^f \cup \Omega_t^s$ can be described by considering the evolution of the solid and fluid parts Ω_0^f and Ω_0^s defined by these two applications

$$\begin{aligned}\mathcal{X}^s &: \Omega_0^s \times \mathbb{R}^+ \rightarrow \mathbb{R}^3, \\ \mathcal{A}^f &: \Omega_0^f \times \mathbb{R}^+ \rightarrow \mathbb{R}^3,\end{aligned}$$

such that $\text{Im}(\mathcal{X}^s(\cdot, t)) = \Omega_t^s$, $\text{Im}(\mathcal{A}^f(\cdot, t)) = \Omega_t^f$. The application \mathcal{X}^s maps the position of any material point \mathbf{x}_0^s from the given fixed reference configuration Ω_0^s to the current solid material configuration Ω_t^s . The solid displacement is then defined as

$$\mathbf{u}^s(\mathbf{x}_0^s, t) = \mathcal{X}(\mathbf{x}_0^s, t) - \mathbf{x}_0^s. \quad (3.81)$$

The application \mathcal{A}^f is such that $\mathcal{A}^f(\mathbf{x}_0^f, t) = \mathbf{x}_0^f + \mathbf{u}^f(\mathbf{x}_0^f, t)$, where $\mathbf{u}^f(\mathbf{x}_0^f, t)$ is defined as an arbitrary extension over the fluid domain Ω_0^f of the interface solid displacement $\mathbf{u}^s|_{\Gamma_0^i}$

$$\mathbf{u}^f(\mathbf{x}_0^f, t) = \text{Ext}(\mathbf{u}^s|_{\Gamma_0^i}) \quad \text{in } \Omega_0^f. \quad (3.82)$$

The more commonly extension operator used in practice is the harmonic or Laplace operator. This implies that \mathbf{u}^f is defined as the solution of the elliptic problem

$$\begin{aligned}-k\Delta\mathbf{u}^f &= \mathbf{0} & \text{in } \Omega_0^f, \\ \mathbf{u}^f &= \mathbf{u}^s & \text{on } \Gamma_0^i,\end{aligned} \quad (3.83)$$

where k is a diffusion coefficient. Other choices for the extension operator can be used, see for instance [Sackinger *et al.* \[1996\]](#) and [Tezduyar & Benney \[2003\]](#).

In selecting a category of mesh moving techniques, geometric complexity is one of the major determining factors. Sometimes, the overall problem geometry, including the interface geometry, is simple enough that the mesh can be updated without solving any additional equations to determine the motion of the mesh. However, in most practical problem, the overall problem geometry is so complex

3. MATHEMATICAL MODELING

that more advanced automatic mesh moving technique than the solution of an harmonic problem must be used in order to not much degrade the mesh quality. We used in the numerical examples described in Chapter 6 a techniques similar to that one described in [Tezduyar & Benney \[2003\]](#), where the motion of the nodes is governed by the following parabolic problem

$$\begin{aligned} \frac{\partial \mathbf{u}^f}{\partial t} - \nabla \cdot (k(\mathbf{x}) \nabla \mathbf{u}^f) &= \mathbf{0} & \text{in } \Omega_0^f, \\ \mathbf{u}^f &= \mathbf{u}^s & \text{on } \Gamma_0^i, \end{aligned} \quad (3.84)$$

and the mesh deformation is dealt with selectively based on the sizes of the elements. Selective treatment based on element sizes is implemented by simply altering the way we account for the Jacobian of the transformation from the element domain to the physical domain. In this case, we would like the smaller elements to be stiffened more than the larger ones. To describe this approach, we first write the global integrals generated by the terms in (3.84) as

$$\int_{\Omega} [\dots] d\Omega = \sum_e \int_{\Omega_e} [\dots]^e J^e d\Omega_e, \quad (3.85)$$

where [...] symbolically represents what is being integrated, Ω_e is the finite element parent domain, and the Jacobian for element Ω_e is defined as

$$J^e = \det \left(\frac{\partial \mathbf{x}}{\partial \boldsymbol{\xi}} \right). \quad (3.86)$$

Here \mathbf{x} represents the physical coordinates and $\boldsymbol{\xi}$ represents the element local coordinates. We alter the way we account for the Jacobian as follows

$$\int_{\Omega} [\dots] d\Omega = \sum_e \int_{\Omega_e} [\dots]^e \left(\frac{J^0}{J^e} \right)^{\chi} d\Omega_e, \quad (3.87)$$

where χ , a non-negative number, is the stiffening power, and J^0 , an arbitrary scaling parameter, is inserted into the formulation to make the alteration dimensionally consistent. In the following, the term $(\frac{J^0}{J^e})^{\chi}$ is taken into account in the finite element formulation through the parameter k . With $\chi = 0$, the method

reduces back to a parabolic problem with no Jacobian-based stiffening. With $\chi = 1.0$, the method is identical to the ones first introduced in [Tezduyar *et al.* \[1992c\]](#). In the general case of $\chi \neq 1.0$, the method stiffens each element by a factor of $(J^e)^{-\chi}$, and χ determines the degree by which the smaller elements are rendered stiffer than the larger ones. In all the simulations we used a value of $\chi = 1.0$.

In chapter 5 we will describe the selective multilevel domain decomposition algorithm for solving the fluid-structure interaction equations. The algorithm asks the user to select the region of selective refinement. If the regions where the mesh would undergo large distortions are selected to be refined, e.g. the region near the fluid-solid interface, we have smaller and stiffer elements where we need them in order to not degrade the mesh quality.

The fluid-structure interaction process is described mathematically by the balance equations of mass and momentum defined in the previous paragraph. The momentum (3.77) and mass (3.61) balance laws for the fluid in the ALE frame with the initial configuration $\Omega^f = \Omega_0^f$ as reference are

$$\begin{aligned} \rho J_{\mathcal{X}} \frac{\partial \mathbf{v}^f}{\partial t} + \rho J_{\mathcal{X}} (\nabla \mathbf{v}^f) \mathbf{F}_{\mathcal{X}}^{-1} (\mathbf{v}^f - \frac{\partial \mathbf{u}^f}{\partial t}) &= \nabla \cdot (J_{\mathcal{X}} \boldsymbol{\sigma} \mathbf{F}_{\mathcal{X}}^{-T}) + \rho J_{\mathcal{X}} \mathbf{f} && \text{in } \Omega^f, \\ \nabla \cdot (J_{\mathcal{X}} \mathbf{v}^f \mathbf{F}_{\mathcal{X}}^{-T}) &= 0 && \text{in } \Omega^f, \end{aligned}$$

together with the momentum (3.73) and mass (3.57) balance laws for the solid in the Lagrangian frame with the initial configuration $\Omega^s = \Omega_0^s$ as reference

$$\begin{aligned} \rho_0 \frac{\partial \mathbf{v}^s}{\partial t} &= \nabla \cdot \mathbf{P} + \rho_0 \mathbf{f} && \text{in } \Omega^s, \\ J - 1 &= 0 && \text{in } \Omega^s. \end{aligned}$$

The coupling between the fluid and the solid is due to the exchange of momentum through the common part of the boundary Γ^i and determines the interface boundary conditions, which consist of imposing the continuity of the velocity

3. MATHEMATICAL MODELING

(no-slip condition) and the stress at the interface $\Gamma^i = \Gamma_0^i$ in the following form

$$\mathbf{v}^f|_{\Gamma^i} = \mathbf{v}^s|_{\Gamma^i}, \quad (3.88)$$

$$J_{\mathcal{X}}\boldsymbol{\sigma}^f \mathbf{F}_{\mathcal{X}}^{-T} \cdot \mathbf{n}^f|_{\Gamma^i} + J_{\mathcal{X}}\boldsymbol{\sigma}^s \mathbf{F}_{\mathcal{X}}^{-T} \cdot \mathbf{n}^s|_{\Gamma^i} = \mathbf{0}. \quad (3.89)$$

In order to the fluid-structure interaction problem be well-posed we have to prescribe the boundary conditions on the fluid inflow and outflow part $\Gamma^{1,f} = \Gamma_0^{1,f}$ and $\Gamma^{2,f} = \Gamma_0^{2,f}$ for the fluid and the boundary conditions on the solid parts $\Gamma^{1,s} = \Gamma_0^{1,s}$ and $\Gamma^3 = \Gamma_0^3$. For example we can prescribe a Dirichlet type boundary condition on the inflow part $\Gamma^{1,f}$

$$\mathbf{v}^f = \mathbf{v}_A \quad \text{on} \quad \Gamma^{1,f}, \quad (3.90)$$

where \mathbf{v}_A is given, a Neumann boundary condition on the outflow part $\Gamma^{2,f}$

$$\boldsymbol{\sigma}^f = p_B \mathbf{n} \quad \text{on} \quad \Gamma^{2,f}, \quad (3.91)$$

where p_B is known, a homogeneous Dirichlet boundary condition for the solid displacement at the part $\Gamma^{1,s}$

$$\mathbf{u}^s = \mathbf{0} \quad \text{on} \quad \Gamma^{1,s}, \quad (3.92)$$

and a stress free boundary condition at the part Γ^3

$$J_{\mathcal{X}}\boldsymbol{\sigma}^s \mathbf{F}_{\mathcal{X}}^{-T} \cdot \mathbf{n}^s = \mathbf{0} \quad \text{on} \quad \Gamma^3. \quad (3.93)$$

For time-dependent flows, a set of initial conditions must be prescribed. We need to provide the initial velocity and displacement field, i.e.

$$\mathbf{v}(\mathbf{x}, 0) = \mathbf{v}_0(\mathbf{x}), \quad \mathbf{u}(\mathbf{x}, 0) = \mathbf{u}_0(\mathbf{x}), \quad (3.94)$$

and the elastic stress field. We assume that the elastic stress field both in the fluid and solid domain is completely relaxed in $t = 0$, i.e.

$$\boldsymbol{\sigma}(\mathbf{x}, 0) \cdot \mathbf{n} = \mathbf{0}. \quad (3.95)$$

We introduce the domain $\Omega = \Omega^f \cup \Omega^s$, where Ω^f and Ω^s are the domains occupied by the fluid and solid in the initial undeformed state, and two fields defined over this domain as

$$\mathbf{u} : \Omega \times [0, T] \rightarrow \mathbb{R}^3, \quad \mathbf{v} : \Omega \times [0, T] \rightarrow \mathbb{R}^3, \quad (3.96)$$

such that the field \mathbf{v} represents the velocity both in the solid and fluid part and \mathbf{u} represents the displacement in the solid part and the artificial displacement in the fluid part,

$$\mathbf{u} = \begin{cases} \mathbf{u}^s & \text{on } \Omega^s, \\ \mathbf{u}^f & \text{on } \Omega^f, \end{cases} \quad \mathbf{v} = \begin{cases} \mathbf{v}^s & \text{on } \Omega^s, \\ \mathbf{v}^f & \text{on } \Omega^f. \end{cases}$$

The complete set of equations can be written as

$$\frac{\partial \mathbf{u}}{\partial t} = \begin{cases} \mathbf{v} & \text{in } \Omega^s, \\ \nabla \cdot (k(\mathbf{x}) \nabla \mathbf{u}^f) & \text{in } \Omega^f, \end{cases} \quad (3.97)$$

$$\frac{\partial \mathbf{v}}{\partial t} = \begin{cases} \frac{1}{\rho_0} \nabla \cdot \mathbf{P} + \mathbf{f} & \text{in } \Omega^s, \\ -(\nabla \mathbf{v}) \mathbf{F}_{\mathcal{X}}^{-1} (\mathbf{v} - \frac{\partial \mathbf{u}}{\partial t}) + \frac{1}{\rho J_{\mathcal{X}}} \nabla \cdot (J_{\mathcal{X}} \boldsymbol{\sigma} \mathbf{F}_{\mathcal{X}}^{-T}) + \mathbf{f} & \text{in } \Omega^f, \end{cases} \quad (3.98)$$

$$0 = \begin{cases} J - 1 & \text{in } \Omega^s, \\ \nabla \cdot (J_{\mathcal{X}} \mathbf{v} \mathbf{F}_{\mathcal{X}}^{-T}) & \text{in } \Omega^f. \end{cases} \quad (3.99)$$

Given a characteristic length L and velocity V , the involved quantities and operators in system (3.97) - (3.99) can be non-dimensionalized as follows

$$\begin{aligned} \hat{t} &= t \frac{V}{L}, & \hat{\mathbf{x}} &= \frac{\mathbf{x}}{L}, \\ \hat{\nabla} &= \nabla L, & \hat{\Delta} &= \Delta L^2, \\ \hat{\mathbf{u}} &= \frac{\mathbf{u}}{L}, & \hat{\mathbf{v}} &= \frac{\mathbf{v}}{V}, \\ \hat{\mathbf{P}} &= \mathbf{P} \frac{L}{\rho^f V^2}, & \hat{\boldsymbol{\sigma}}^f &= \boldsymbol{\sigma}^f \frac{L}{\rho^f V^2}, \\ \hat{\mu}^f &= \frac{\mu^f}{\rho^f V L}, & \hat{\mathbf{f}} &= \mathbf{f} \frac{L}{\rho^f V^2}, \end{aligned}$$

3. MATHEMATICAL MODELING

Denoting by $\beta = \frac{\rho^s}{\rho^f}$ the density ratio and using the non-dimensional quantities and operators defined above, the non-dimensional system of equations reads

$$\frac{\partial \hat{\mathbf{u}}}{\partial \hat{t}} = \begin{cases} \hat{\mathbf{v}} & \text{in } \hat{\Omega}^s, \\ \hat{\nabla} \cdot (k(\hat{\mathbf{x}}) \nabla \hat{\mathbf{u}}^f) & \text{in } \hat{\Omega}^f, \end{cases} \quad (3.100)$$

$$\frac{\partial \hat{\mathbf{v}}}{\partial \hat{t}} = \begin{cases} \frac{1}{\beta} \hat{\nabla} \cdot \hat{\mathbf{P}} + \hat{\mathbf{f}} & \text{in } \hat{\Omega}^s, \\ -(\hat{\nabla} \hat{\mathbf{v}}) \mathbf{F}_{\mathcal{X}}^{-1} (\hat{\mathbf{v}} - \frac{\partial \hat{\mathbf{u}}}{\partial \hat{t}}) + \frac{1}{J_{\mathcal{X}}} \hat{\nabla} \cdot (J_{\mathcal{X}} \hat{\boldsymbol{\sigma}} \mathbf{F}_{\mathcal{X}}^{-T}) + \hat{\mathbf{f}} & \text{in } \hat{\Omega}^f, \end{cases} \quad (3.101)$$

$$0 = \begin{cases} J - 1 & \text{in } \hat{\Omega}^s, \\ \hat{\nabla} \cdot (J_{\mathcal{X}} \hat{\mathbf{v}} \mathbf{F}_{\mathcal{X}}^{-T}) & \text{in } \hat{\Omega}^f, \end{cases} \quad (3.102)$$

where $\hat{\Omega}^f$ and $\hat{\Omega}^s$ denotes the non - dimensional fluid and solid domain. In subsequent sections, the hat notation will be dropped and the same symbols, without the hat, will be used for dimensional and non-dimensional quantities.

3.5 Constitutive equations

Balance laws derived in the previous sections are general since no information on the material response have been prescribed. From a mathematical point of view it means that they represent an undetermined system. Therefore, we have to provide additional equations in the form of suitable constitutive laws in order to modeling from the macroscopic point of view the real mechanical behavior of the material in question. In the case of fluid-structure interaction problem we must establish the mathematical relationship between stress and strain and between strain and kinematics variables. In this work a comprehensive review of the constitutive theory will not be presented, we limit ourselves to presenting some constitutive equations for fluid and solid in the following subsections that are very used in literature.

3.5.1 Constitutive equations for incompressible fluid

In the FSI problem, fluid dynamics has been described by the incompressible Navier-Stokes equations derived in the ALE framework. For incompressible flow,

the density ρ^f of the fluid is considered to be constant in space and time while the stress tensor $\boldsymbol{\sigma}^f$ is defined by

$$\boldsymbol{\sigma}^f = -p^f \mathbf{I} + \mathbf{T}, \quad (3.103)$$

where p^f is the Lagrange multiplier associated to the incompressibility constraint 3.54. The former term is called the hydrostatic component of the Cauchy stress tensor while the latter one is called the viscous component. It is known that fluids react mechanically not to the deformation itself but on the rate of deformation. The viscous tensor \mathbf{T} is responsible for the fluid distortional rate of deformation.

The simplest viscous fluid model is that due to Newton. For a *Newtonian* fluid, the tensor \mathbf{T} is a linear isotropic function of the components of the velocity gradient, namely,

$$\mathbf{T} = 2\mu^f \mathbf{D}, \quad (3.104)$$

where μ^f is the dynamic viscosity of the fluid and

$$\mathbf{D} = \frac{1}{2}(\nabla \mathbf{v}^f + (\nabla \mathbf{v}^f)^T), \quad (3.105)$$

is the rate of strain (deformation) tensor. This simple model is commonly used with some justifications to describe blood flow in the heart and healthy arteries (Ku [1997]). Blood has nonetheless a non-Newtonian behavior and from experimental observations this non-Newtonian behavior becomes significant in segments of the venous system, in the sacs of some aneurysms and downstream of some stenosis where stable vortexes occurs. In the following, we will show some rheologically admissible constitutive equations with shear thinning viscosity under the name of *Generalized Newtonian Fluid* that are more suitable than Newtonian model in blood flow.

3.5.1.1 Generalized Newtonian Fluid

A fluid for which \mathbf{T} is independent of the history of deformation is known as the *generalized Newtonian fluid*. In order to derive a generalized Newtonian fluid model, we have to establish the mathematical relationship between the viscosity μ^f and the invariants of the strain tensor \mathbf{D} . This assures that the constitu-

3. MATHEMATICAL MODELING

tive model is independent of the coordinate system. Since \mathbf{D} is symmetric by definition, it can be diagonalized and its eigenvalues are real. The three principal invariants (I_D, II_D, III_D) of \mathbf{D} can be computed as the coefficients of the characteristic polynomial

$$\det(\mathbf{D} - \lambda \mathbf{I}) = -\lambda^3 + I_D \lambda^2 - II_D \lambda + III_D = 0, \quad (3.106)$$

and they can be expressed as a function of the eigenvalues λ_1, λ_2 and λ_3 of the matrix \mathbf{D}

$$\begin{aligned} I_D &= \text{tr}(\mathbf{D}) = \lambda_1 + \lambda_2 + \lambda_3, \\ II_D &= \frac{1}{2}((\text{tr}(\mathbf{D}))^2 - \text{tr}(\mathbf{D}^2)) = \lambda_1 \lambda_2 + \lambda_2 \lambda_3 + \lambda_1 \lambda_3, \\ III_D &= \det(\mathbf{D}) = \lambda_1 \lambda_2 \lambda_3. \end{aligned}$$

For the considerations above, the following relation between the viscous stress tensor and the rate of deformation tensor can be established

$$\mathbf{T} = 2\mu^f(I_D, II_D, III_D)\mathbf{D}. \quad (3.107)$$

We can notice that for incompressible flow the first invariant is null, i.e. $I_D = 0$. In addition, the dependence on the value of the third invariant is often considered negligible (Astarita & Marrucci [1974]). The incompressible generalized Newtonian fluid takes the following form

$$\mathbf{T} = 2\mu^f(II_D)\mathbf{D}, \quad (3.108)$$

where $\mu^f(\cdot)$ is the (nonlinear) viscosity function which depend in general on the second invariant of the strain rate tensor II_D .

Generalized Newtonian fluids are a special class of the most general incompressible constitutive model of the form $\mathbf{T} = \mathbf{T}(\nabla \mathbf{v})$ called *Reiner-Rivlin fluids*. For which class of fluids the constitutive equations is

$$\mathbf{T} = \mu_1(II_D, III_D)\mathbf{D}(\mathbf{v}) + \mu_2(II_D, III_D)\mathbf{D}(\mathbf{v})^2. \quad (3.109)$$

Table 3.1: Various generalized Newtonian models for blood.

Model	$\frac{\mu(\dot{\gamma}) - \mu_\infty}{\mu_0 - \mu_\infty}$
Powell-Eyring	$\frac{\sinh^{-1}(\lambda\dot{\gamma})}{\lambda\dot{\gamma}}$
Cross	$\frac{1}{1+(\lambda\dot{\gamma})^m}$
Modified Cross	$\frac{1}{(1+(\lambda\dot{\gamma})^m)^a}$
Carreau	$(1 + (\lambda\dot{\gamma})^2)^{\frac{n-1}{2}}$
Carreau-Yasuda	$(1 + (\lambda\dot{\gamma})^a)^{\frac{n-1}{a}}$

Since the behavior of Reiner-Rivlin fluids with non zero values of μ_2 in simple shear flow does not match experimental results on real fluids (Astarita & Marrucci [1974]), attention is typically confined to the more specific generalized Newtonian model.

The quantity II_D is not a positive quantity, so it is useful to introduce a metric of the rate of deformation, denoted by $\dot{\gamma}$,

$$\dot{\gamma} = \sqrt{2\text{tr}(\mathbf{D}(\mathbf{v})^2)} = \sqrt{-4II_D}. \quad (3.110)$$

Using (3.110), the generalized Newtonian model (3.108) takes the useful form

$$\mathbf{T} = 2\mu^f(\dot{\gamma})\mathbf{D}. \quad (3.111)$$

The most common generalized Newtonian models that have been considered in the literature for the shear dependent viscosity of human blood are summarized in table 3.1 and are the Power-law type model, Powell-Eyring model, Cross model, Modified Cross model, Carreau fluid model and the Carreau-Yasuda Model.

A simple example of a generalized Newtonian fluid is that of the power-law fluid, which has viscosity function given by

$$\mu = k\dot{\gamma}^{(n-1)}, \quad (3.112)$$

where k is a positive constant and is called consistency and n is the law index

3. MATHEMATICAL MODELING

which maximum value is 1. If $n = 1$ we recover the Newtonian model with its constant viscosity, but if $n < 1$ the viscosity is a decreasing function of the shear rate (*shear thinning fluid*) and if $n > 1$ it is an increasing function of the shear rate (*shear thickening fluid*). One of the major advantage of this model is the possibility to obtain analytical solutions to the Navier-Stokes equations. The two major drawbacks for the shear-thinning case are that the zero shear rate viscosity is unbounded and the asymptotic limit as $\dot{\gamma} \rightarrow \infty$ is zero. Both these asymptotic behavior are unphysical and limit the range of shear rates over which the power-law model is valid for blood.

One of the more successful viscosity laws for blood is an extension of the power-law model due to Walburn and Schneck (Walburn & Schneck [1976]). In addition to the shear rate, they considered the dependance of the viscosity on the haematocrit (Ht) and total protein minus albumin (TPMA) content through the parameters k and n .

Yasuda proposed a five parameter ($\eta_0, \eta_\infty, \lambda, n, a$) model similar to the modified Cross model, see Table 3.1, but he added an extra material constant a giving more flexibility in order to fit experimental data. It has been proven to be very useful for realistic numerical simulation. In the model η_0 is the zero-shear-rate viscosity, η_∞ is the infinite-shear-rate viscosity, λ is a time constant, n is the power-law exponent and a is a dimensionless parameter that describes the behavior of the non linear curve between the zero-shear-rate region and power-law region. Several special cases of the Yasuda model can be obtained. For instance, if $a = 2$ we recover the Carreau model, if $n = a + 1 = m + 1$ we recover the Cross model and if $m = a$ and $n = a^2 + 1$ we recover the modified Cross model.

3.5.2 Constitutive equations for solid

The constitutive equations for solid establish the mathematical relationship between the strain \mathbf{E} and the stress \mathbf{S} and between the strain \mathbf{E} and the displacement \mathbf{u} . In this thesis we will consider only the St. Venant-Kirchhoff material and the Neo-Hookean model. Both models share the isotropic and homogeneous properties, and both can be used for the computation of large deformations. However, the St. Venant Kirchhoff model does not allow for large strain computations,

while the Neo-Hookean model is also valid for large strains.

3.5.2.1 Elastic Material

Materials for which the stress field depends only on the current state of deformation and not on the deformation history are called *elastic*. Under such conditions, any stress measure at a particle \mathbf{X} is a function of the deformation gradient \mathbf{F} associated with that particle. In the following, the deformation gradient \mathbf{F} and the first Piola-Kirchhoff stress tensor \mathbf{P} will be used to define the material relationships. Consequently, we may express the constitutive equation as

$$\mathbf{P} = \mathbf{P}(\mathbf{F}(\mathbf{X}, t), \mathbf{X}). \quad (3.113)$$

If the first Piola-Kirchhoff stress tensor \mathbf{P} and the reference mass density ρ_0 are independent of the particle position \mathbf{X} we have

$$\mathbf{P} = \mathbf{P}(\mathbf{F}(\mathbf{X}, t)). \quad (3.114)$$

Such materials are called *homogeneous*. If the material has the same response to deformation in all directions, it is called *isotropic*. The constitutive equation for an isotropic material satisfies the following relation

$$\mathbf{P}(\mathbf{F}\mathbf{Q}) = \mathbf{Q}^T \mathbf{P}(\mathbf{F}) \mathbf{Q}, \quad (3.115)$$

which is the material isotropic condition and \mathbf{Q} is an orthogonal matrix associated to a rigid body rotation. In the rest of this thesis we restrict our attention to materials that are homogeneous, isotropic and frame indifference. Finally, if we want that the reference configuration is stress free, we have to ensure that the *residual stress* is zero, i.e.

$$\mathbf{P}(\mathbf{I}) = \mathbf{0}. \quad (3.116)$$

3.5.2.2 Hyperelastic material

If the work done by the stress during a deformation process is dependent only on the initial and final state, the behavior of the material is said to be path-

3. MATHEMATICAL MODELING

independent and the material is termed *hyperelastic*. As a consequence of the path-independent behavior, a *stored strain energy function* or *elastic potential* Ψ per unit undeformed volume can be established as the work done by the stress tensor from the the initial position at time t_0 to the current position at time t as,

$$\Psi(\mathbf{F}(\mathbf{X}), \mathbf{X}) = \int_{t_0}^t \mathbf{P}(\mathbf{F}(\mathbf{X}), \mathbf{X}) : \dot{\mathbf{F}} dt, \quad \dot{\Psi} = \mathbf{P} : \dot{\mathbf{F}}. \quad (3.117)$$

Presuming that from physical experiments it is possible to construct the function Ψ , which defines a given material, then the rate of change of the potential can be alternatively expressed as,

$$\dot{\Psi} = \sum_{i,j=0}^3 \frac{\partial \Psi}{\partial \dot{F}_{i,j}} \dot{F}_{i,j}. \quad (3.118)$$

Comparing this equation with equation (3.117) the components of the Piola-Kirchhoff stress tensor \mathbf{P} are given by

$$P_{i,j} = \frac{\partial \Psi_{i,j}}{\partial F_{i,j}}. \quad (3.119)$$

For notational convenience this expression is rewritten in a more compact form

$$\mathbf{P}(\mathbf{F}(\mathbf{X}), \mathbf{X}) = \frac{\partial \Psi(\mathbf{F}(\mathbf{X}), \mathbf{X})}{\partial \mathbf{F}}. \quad (3.120)$$

For a homogeneous, isotropic and frame indifference material, the potential energy depends only upon the deformation gradient \mathbf{F} . Besides we require for convenience that the strain-energy function vanishes in the reference configuration, i.e.

$$\Psi(\mathbf{I}) = 0. \quad (3.121)$$

From physical observations we know that the strain-energy function Ψ increases with deformation. Therefore, in addition to (3.121) we require that

$$\Psi(\mathbf{F}) \geq 0. \quad (3.122)$$

Finally we have to prescribe the behavior of the scalar-valued function Ψ when

$J = \det \mathbf{F}$ approaches $+\infty$ or 0^+

$$\begin{aligned}\Psi(\mathbf{F}) &\rightarrow +\infty & \text{as} & & J &\rightarrow +\infty, \\ \Psi(\mathbf{F}) &\rightarrow +\infty & \text{as} & & J &\rightarrow 0^+.\end{aligned}$$

These mathematical assumptions mean that it is required an infinite amount of energy to expand a continuum body to an infinite dimension or to compress it to a material point.

The frame indifference assumption imposes that Ψ must be invariant if a body undergoes a rigid body rotation. This implies that Ψ depends on \mathbf{F} only via its stretch component \mathbf{U} and must be independent of the rotation component \mathbf{Q} . For convenience, Ψ is often expressed as a function of the right Cauchy-Green deformation tensor $\mathbf{C} = \mathbf{F}^T \mathbf{F}$

$$\hat{\Psi}(\mathbf{C}(\mathbf{X}, t), \mathbf{X}) = \Psi(\mathbf{F}(\mathbf{X}, t), \mathbf{X}). \quad (3.123)$$

Remembering that $\mathbf{S} = \mathbf{F}\mathbf{P}$ and $\mathbf{C} = \frac{1}{2}(\mathbf{F}\mathbf{F}^T - \mathbf{I})$, Equations (3.117)-b and (3.120) become

$$\dot{\hat{\Psi}} = \frac{1}{2} \mathbf{S} : \dot{\mathbf{C}} = \frac{\partial \hat{\Psi}}{\partial \mathbf{C}} : \dot{\mathbf{C}}, \quad \mathbf{S}(\mathbf{C}(\mathbf{X}), \mathbf{X}) = 2 \frac{\partial \hat{\Psi}}{\partial \mathbf{C}}. \quad (3.124)$$

3.5.2.3 Incompressible and nearly incompressible hyperelastic material

Materials can be classified as compressible, nearly - incompressible and incompressible. Most practical large strain processes take place under incompressible or nearly - incompressible conditions. Incompressible materials do not allow changes of volume but only of the shape while compressible materials can undergoes changes of volume. The terminology “nearly - incompressible” used here indicates a material which is truly incompressible but its numerical treatment allow a small change of volumetric distortion.

In order to determine the constitutive equation for an incompressible hyper-

3. MATHEMATICAL MODELING

elastic material, recall equation (3.124)-a rearranged as

$$\left(\frac{1}{2}\mathbf{S} - \frac{\partial\hat{\Psi}}{\partial\mathbf{C}}\right) : \dot{\mathbf{C}} = 0. \quad (3.125)$$

Previously, the fact that \mathbf{C} in this equation was arbitrary implied that $\mathbf{S} = \frac{\partial\hat{\Psi}}{\partial\mathbf{C}}$. In the incompressible case, it is no more true because the term in brackets is not guaranteed to vanish since \mathbf{C} is no longer arbitrary. In fact, given that $J = 1$ during the deformation process and therefore $\dot{J} = 0$, by using the identity $\dot{J} = \frac{1}{2}J\mathbf{C}^{-1} : \dot{\mathbf{C}}$, we have

$$\frac{1}{2}J\mathbf{C}^{-1} : \dot{\mathbf{C}} = 0. \quad (3.126)$$

The fact that Equation (3.125) has to be satisfied for any \mathbf{C} satisfying the constraint (3.126) implies that

$$\frac{1}{2}\mathbf{S} - \frac{\partial\hat{\Psi}}{\partial\mathbf{C}} = \gamma\frac{J}{2}\mathbf{C}^{-1}, \quad (3.127)$$

where γ is an unknown scalar that will, under certain circumstances that we will discuss later, coincide with the hydrostatic pressure and will be determined by using an additional equation given by the incompressibility constraint $J = 1$. From Equation (3.127) we obtain the following general incompressible hyperelastic constitutive equation

$$\mathbf{S} = 2\frac{\partial\hat{\Psi}(\mathbf{C})}{\partial\mathbf{C}} + \gamma J\mathbf{C}^{-1}. \quad (3.128)$$

The determinant J in the above equation may seem unnecessary in the case of incompressibility where $J = 1$, but retaining J has the advantage that Equation (3.128) is also applicable in the nearly incompressible case.

Remembering the deviatoric - hydrostatic decomposition of the second Piola - Kirchhoff tensor $\mathbf{S} = \mathbf{S}' + pJ\mathbf{C}^{-1}$ and the identity $p = \frac{1}{3}J^{-1}\mathbf{S} : \mathbf{C}$, where p is defined as the trace of the Cauchy stress tensor multiplied by one third, it can be proved that p and γ coincide if the following relation is satisfied,

$$\frac{\partial\hat{\Psi}}{\partial\mathbf{C}} : \mathbf{C} = 0. \quad (3.129)$$

This implies that the function $\hat{\Psi}(\mathbf{C})$ must be homogeneous of order 0, i.e. $\hat{\Psi}(\mathbf{C}) = \hat{\Psi}(\alpha\mathbf{C})$ for any arbitrary constant α . This result can be achieved by recognizing that for incompressible materials $\det\mathbf{C} = J^2 = 1$. We can therefore express the energy function $\hat{\Psi}$ in terms of the distortional component of the right Cauchy - Green tensor $\hat{\mathbf{C}} = J^{-\frac{2}{3}}\mathbf{C}$ to obtain a formally modied energy function $\hat{\Psi}(\mathbf{C}) = \hat{\Psi}(\hat{\mathbf{C}})$. It can be easily proved the function $\hat{\Psi}(\mathbf{C})$ is homogeneous.

Accepting that for the case of incompressible materials $\hat{\Psi}(\hat{\mathbf{C}})$ can be replaced by $\hat{\Psi}(\mathbf{C})$, condition (3.129) is satisfied and Equation (3.128) becomes,

$$\mathbf{S} = 2\frac{\partial\hat{\Psi}(\mathbf{C})}{\partial\mathbf{C}} + \gamma J\mathbf{C}^{-1}. \quad (3.130)$$

If we compare this relation with the deviatoric - hydrostatic decomposition of the second Piola - Kirchhoff stress tensor, we obtain the following relation for the deviatoric component of the second Piola - Kirchhoff stress tensor

$$\mathbf{S}' = 2\frac{\partial\hat{\Psi}(\mathbf{C})}{\partial\mathbf{C}}. \quad (3.131)$$

Remark 3.5.1. Note that the derivative $\frac{\partial\hat{\Psi}(\mathbf{C})}{\partial\mathbf{C}}$ is not equal to the derivative $\frac{\partial\hat{\Psi}(\hat{\mathbf{C}})}{\partial\hat{\mathbf{C}}}$, despite the fact that $\hat{\mathbf{C}} = \mathbf{C}$ for incompressibility. This is because $J^{-\frac{2}{3}}$ remains a function of \mathbf{C} while the derivative of $\hat{\mathbf{C}}$ is being executed.

Typical examples for the elastic potential used for homogenous, isotropic and incompressible materials are the *Neo-Hookean* model given by

$$\hat{\Psi} = \mu_1^s(I_{\hat{\mathbf{C}}} - 3), \quad (3.132)$$

or the *Mooney-Rivlin* material

$$\hat{\Psi} = \mu_1^s(I_{\hat{\mathbf{C}}} - 3) + \mu_2^s(II_{\hat{\mathbf{C}}} - 3), \quad (3.133)$$

where $I_{\hat{\mathbf{C}}} = \text{tr}\hat{\mathbf{C}}$, $II_{\hat{\mathbf{C}}} = \frac{1}{2}((\text{tr}\hat{\mathbf{C}})^2 - \text{tr}(\hat{\mathbf{C}}^2))$ and $III_{\hat{\mathbf{C}}} = \det\hat{\mathbf{C}}$ are the invariants of the right Cauchy - Green deformation tensor $\hat{\mathbf{C}}$ and μ_i^s are some material constants. In particular for the Neo-Hookean incompressible model, making use

3. MATHEMATICAL MODELING

of (3.132) and (3.130), the second Piola - Kirchhoff stress tensor is given by

$$\mathbf{S}^s = p^s J \mathbf{C}^{-1} + \mu_1^s J^{-\frac{2}{3}} (\mathbf{I} - \frac{1}{3} I_C \mathbf{C}^{-1}). \quad (3.134)$$

The corresponding Cauchy stress tensor can now be obtained from (3.134) by using Equation (3.42)

$$\boldsymbol{\sigma}^s = p^s \mathbf{I} + \mu_1^s J^{-\frac{5}{3}} (\mathbf{b} - \frac{1}{3} I_b \mathbf{I}), \quad (3.135)$$

where we have used the identity $I_b = I_C$.

By relaxing the incompressibility constraint $J = 1$ in

$$-\frac{p^s}{\lambda^s} + \frac{1}{2} (J - \frac{1}{J}) = 0, \quad (3.136)$$

but still using the Neo-Hookean incompressible constitutive relation for the Cauchy stress tensor

$$\boldsymbol{\sigma}^s = p^s \mathbf{I} + \mu_1^s (\mathbf{b} - \mathbf{I}), \quad (3.137)$$

we recover the Neo-Hookean mixed formulation that can be used for nearly incompressible and incompressible (for $\nu^s = 1/2 \Rightarrow \lambda^s \rightarrow \infty$) material at the same time through the Poisson ratio ν^s . In addition, the formulation can also be applied to the compressible case ($\nu^s \approx 0.4$)

$$\boldsymbol{\sigma}^s = \lambda^s (J - \frac{1}{J}) \mathbf{I} + \frac{\mu^s}{J} (\mathbf{b} - \mathbf{I}). \quad (3.138)$$

Alternative formulations of the compressible Neo-Hookean model exist and can be easily found in literature (e.g. $\boldsymbol{\sigma}^s = \lambda^s \log(J) \mathbf{I} + \frac{\mu^s}{J} (\mathbf{b} - \mathbf{I})$ or $\boldsymbol{\sigma}^s = \lambda^s (J - 1) \mathbf{I} + \frac{\mu^s}{J} (\mathbf{b} - \mathbf{I})$). They show a similar behavior for small volumetric changes.

Remark 3.5.2. *All these models when restricted to small deformations can be linearized leading to the Hooke's law*

$$\boldsymbol{\sigma}^s = \lambda^s (\nabla \cdot \mathbf{u}^s) \mathbf{I} + \mu^s (\nabla \mathbf{u}^s + (\nabla \mathbf{u}^s)^T), \quad (3.139)$$

which is also known as the Navier-Lamé equation.

Chapter 4

Discretization procedure

In this chapter, a monolithic ALE formulation of the fluid-structure interaction problem derived in Chapter 3 will be numerically discretized by the classical Galerkin finite element method in space firstly and time discretization is done next by using one of the time-stepping techniques described in the follow. Before derivations, a short presentation of the Galerkin finite element is given. The issues of appropriate space and time discretization techniques will be addressed.

4.1 The Galerkin Method

4.1.1 Introduction

The *Galerkin Method* is an approximated method that employs the variational statements (i.e., either variational principles or weak formulations) to determine continuous solutions of PDE problems that can be found in engineering or applied sciences. This method seeks a solution to the given problem in terms of adjustable parameters that are determined by minimizing a functional or by solving the weak form of the original problem. This method belongs to a wide class of methods that are called *direct methods* because the approximated solutions are obtained directly by using a variational formulation equivalent to the original problem. The Least Squares, Petrov-Galerkin, generalized Galerkin, collocation method and subdomain methods are other examples of direct methods that can be used for numerical approximation of PDEs.

4. DISCRETIZATION PROCEDURE

The solutions that can be obtained by using a direct method are in the form of a finite linear combination of functions from an appropriate functional space. This means that we are looking for a solution that belongs to a finite-dimensional subspace V_N of the solution space V of the original problem. Since in general the solution of the original problem lies in an infinite-dimensional space V which cannot be represented exactly by a finite linear combination of functions, an approximation error is introduced in the method. In other words, the solution obtained by using this procedure is an approximation of the true solution of the PDE problem. As the number of linear-independent vector functions in the approximated solution is increased (i.e., the dimension of the space V_N is increased), the approximation error is reduced and the approximated solution converges to the desired solution of the given partial differential equations.

In this thesis the classical Galerkin method has been adopted for spatial discretization of the FSI equations. This method can be directly applied to a Boundary Value Problem (BVP) irrespective of the existence of an extremal formulation. In this subsection the general procedure of the Galerkin method is presented following the presentation of [Quarteroni & Valli \[1994\]](#).

4.1.2 An abstract reference Boundary Value Problem

As usual, Ω denotes a bounded domain of \mathbb{R}^n , $n = 2, 3$, whose boundary is $\partial\Omega$. We consider a boundary value problem of the form

$$\begin{cases} Au = f & \text{in } \Omega, \\ Bu = 0 & \text{on } \partial\Omega^*, \end{cases} \quad (4.1)$$

where f is a given function, u is the solution unknown, A is a linear differential operator and B is an affine boundary operator. Finally, $\partial\Omega^*$ is a subset of $\partial\Omega$ (otherwise it can be the whole boundary). Most often, L is an unbounded operator in a space H that can be either $L^2(\Omega)$ or $L^2_w(\Omega)$. The latter is the weighted Hilbert space. The solution u is looked for in a space $X \subset H$, such that L and B have a meaning for functions belonging to X .

Problem (4.1) can generally be reformulated in a weak (or variational) form.

From one hand, this approach allows weak solutions to be founded, which means that the equations in (4.1) are not in general satisfied in a pointwise manner. This is a good aspect because it increases the number of physical applications including problems with non-smooth data. From the other hand, the weak formulation is the form that is employed by approximation methods like the Ritz-Galerkin methods and its extensions (Petrov-Galerkin, generalized Galerkin, etc.).

Formally speaking, the weak formulation can be derived after multiplication of the given differential problem by a suitable set of test functions and performing an integration over the domain. Most often, the Green formula of integration by parts (2.27) is used at this stage in order to reduce the order of differentiation for the solution u . As a result, we obtain a problem that reads

$$\text{find } u \in W : \mathcal{A}(u, v) = \mathcal{F}(v) \quad \forall v \in V, \quad (4.2)$$

where W is the space of admissible solutions and V is the space of test functions. Both W and V can be assumed to be Hilbert spaces. \mathcal{F} is a linear functional on V that accounts for the right hand side f as well as for possible non-homogeneous boundary terms. Finally \mathcal{A} is a bilinear form corresponding to the differential operator A . The boundary conditions on the solution u can be enforced directly in the definition of the space W (this is the case of the so-called *essential* boundary conditions) or can be achieved indirectly by modifying suitably the bilinear form \mathcal{A} as well as the functional \mathcal{F} (*natural* boundary conditions).

The existence and uniqueness issues are addressed in the following theorem, referring to the special case $W = V$.

Theorem 4.1.1 (Lax-Milgram lemma). *Let V be a (real) Hilbert space, endowed with the norm $\|\cdot\|$, $\mathcal{A}(u, v): V \times V \rightarrow \mathbb{R}$ a bilinear form and $\mathcal{F}(v): V \rightarrow \mathbb{R}$ a linear continuous functional, i.e., $\mathcal{F} \in V'$, where V' denotes the dual space of V . Assume moreover that $\mathcal{A}(\cdot, \cdot)$ is continuous, i.e.,*

$$\exists \gamma > 0 : |\mathcal{A}(w, v)| \leq \gamma \|w\| \|v\| \quad \forall w, v \in V, \quad (4.3)$$

4. DISCRETIZATION PROCEDURE

and coercive, i.e.,

$$\exists \alpha > 0 : \mathcal{A}(v, v) \geq \alpha \|v\|^2 \quad \forall v \in V. \quad (4.4)$$

Then, there exists a unique $u \in V$ solution to (4.2) and

$$\|u\| \leq \frac{1}{\alpha} \|\mathcal{F}\|_{V'}. \quad (4.5)$$

If the bilinear form is symmetric, i.e.,

$$\mathcal{A}(w, v) = \mathcal{A}(v, w) \quad \forall w, v \in V, \quad (4.6)$$

then $\mathcal{A}(\cdot, \cdot)$ defines a scalar product on V , and the Riesz representation theorem is sufficient to infer existence and uniqueness for the solution of (4.2). We recall that in the symmetric case the solution of (4.2) can be regarded as the unique solution to the *minimization problem*

$$\text{find } u \in V : J(u) \leq J(v) \quad \forall v \in V \quad (4.7)$$

where

$$J(v) := \frac{1}{2} \mathcal{A}(v, v) - \mathcal{F}(v) \quad (4.8)$$

is a quadratic functional.

4.1.3 Description of the method

Let consider the case where $W = V$ and the problem at hand (4.2). This case corresponds to the so-called (Bubnov-)Galerkin method or classical Galerkin method. If $W \neq V$ we consider the case under the name of Petrov-Galerkin method which leads to upwind-type discretizations. Let $h > 0$ be a parameter characteristic of the approximation that can be reduced in the application. In the finite element context, h denotes the mesh spacing. Let

$$\{V_h \mid h > 0\} \quad (4.9)$$

denote a family of finite-dimensional subspaces of V that are dependent from the parameter h . We assume that

$$\text{for all } v \in V, \inf_{v_h \in V_h} \|v - v_h\| \rightarrow 0 \text{ as } h \rightarrow 0. \quad (4.10)$$

The Galerkin approximation of the weak problem (4.2) reads: given $\mathcal{F} \in V'$

$$\text{find } u_h \in V_h : \mathcal{A}(u_h, v_h) = \mathcal{F}(v_h) \quad \forall v_h \in V_h, \quad (4.11)$$

It is therefore an *internal* approximation of the weak problem (4.2).

Let $\{\phi_j | j = 1, \dots, N_h\}$ be a basis for the vector space V_h and N_h its dimension, so the approximate solution can be written as

$$u_h(\mathbf{x}) = \sum_{j=1}^{N_h} \xi_j \phi_j(\mathbf{x}). \quad (4.12)$$

Then, the Galerkin approximation (4.11) can be rewritten from the algebraic point of view as a linear system of dimension N_h :

$$\mathbf{A}\boldsymbol{\xi} = \mathbf{F} \quad (4.13)$$

where $\boldsymbol{\xi} = (\xi_j)$, $\mathbf{F} := (\mathcal{F}(\phi_i))$, $A_{ij} = \mathcal{A}(\phi_j, \phi_i)$ for $i, j = 1, \dots, N_h$. The matrix A is called the *stiffness matrix*. The matrix A is positive definite, i.e., for any $\boldsymbol{\eta} \in \mathbb{R}^{N_h}$, $\boldsymbol{\eta} \neq \mathbf{0}$, $(A\boldsymbol{\eta}, \boldsymbol{\eta}) > 0$. If the bilinear form \mathcal{A} is symmetric, it is easy to verify that \mathbf{A} is also symmetric.

The following theorem deals with the convergence and stability of the Galerkin method.

Theorem 4.1.2. *Under the assumptions of Theorem 4.1.1 there exists a unique solution u_h to (4.11), which furthermore is stable since*

$$\|u_h\| \leq \frac{\|\mathcal{F}\|_{V'}}{\alpha}. \quad (4.14)$$

4. DISCRETIZATION PROCEDURE

Moreover, if u is the solution to (4.2), it follows

$$\|u - u_h\| \leq \frac{\gamma}{\alpha} \inf_{v_h \in V_h} \|u - v_h\|, \quad (4.15)$$

hence u_h converges to u , owing to (4.10).

Estimate (4.15) is usually referred to as *Céa lemma*. When $\mathcal{A}(\cdot, \cdot)$ is symmetric, Galerkin method is referred to as the Ritz method. In this case existence and uniqueness results can be obtained by using the Riesz representation theorem.

4.2 The Galerkin Finite Element Method

4.2.1 Introduction

The finite element method is a variational procedure in which the approximating functions are algebraic piecewise-polynomials developed for subdomains into which a given domain is divided. The subdomains, called *finite elements*, are geometrically simple shapes that allow a systematic construction of the basis functions using concepts from interpolation theory. Since the approximating functions are algebraic polynomials, the computation of the coefficient matrices of the algebraic equations (4.13) can be easily automatized and computed.

The finite element method has emerged as one of the most powerful numerical tools for numerical approximation of PDE. It can be used for problems that are geometrically complex, have discontinuous load, or involve discontinuous material or geometric properties. The accuracy of the numerical solution can be improved either by mesh refinement or by increasing the degree of the FEM basis polynomials. The FEM method revealed to be well-suited for the development of general-purpose computational codes.

The standard finite element approximations are based upon the Galerkin approximation of the variational statement of the physical problem at hand. In the next subsection we present the basic concepts of the finite element approximation.

4.2.2 Triangulation

One of the main features of the finite element method is the representation of a given domain as a collection of “simple” subdomains. There are two reasons for this. First, the derivation of the finite element basis functions using algebraic polynomials is possible only for simple and well-defined geometries, such as line in one-dimension, triangles and rectangles in two-dimension and hexahedron, tetrahedron, wedge and pyramid in three-dimension. Second, since the approximating functions are defined element-wise, the accuracy of the numerical approximation can be improved by simply increasing the number of elements of the subdivision. The representation of a domain by a collection of elements is called *mesh generation* and the collection is called the *finite element mesh* Ω_h . A further subdivision of a generic finite element mesh is called the *mesh refinement*.

All of the above discussion can be expressed in mathematical terms as follows. Let the set $\Omega \subset \mathbb{R}^n$, $n = 2, 3$, be a polygonal domain, i.e., Ω is an open bounded connected subset such that $\bar{\Omega}$ is the union of a finite number of polyhedra. Let consider the following finite decomposition

$$\bar{\Omega} = \bigcup_{K \in \mathcal{T}_h} K, \quad (4.16)$$

where:

- each K is a polyhedron with $\dot{K} \neq \emptyset$;
- $\dot{K}_1 \cap \dot{K}_2 = \emptyset$ for each distinct $K_1, K_2 \in \mathcal{T}_h$;
- if $F = K_1 \cap K_2 \neq \emptyset$, (K_1 and K_2 distinct elements of \mathcal{T}_h) then F is a common face, side, or vertex of K_1 and K_2 ;
- $\text{diam}(K) \leq h$ for each $K \in \mathcal{T}_h$.

\mathcal{T}_h is called a *triangulation* of $\bar{\Omega}$. Every element K of the triangulation \mathcal{T}_h can be obtained as $K = T_K(\hat{K})$, where \hat{K} is a reference polyhedron and T_K a suitable invertible linear or non-linear map.

If the domain Ω cannot be expressed as a polygonal domain, the union of all elements $\bigcup_{K \in \mathcal{T}_h} K$ is not equal to the total domain Ω and an additional error to

4. DISCRETIZATION PROCEDURE

the finite element solution is introduced due to the inexact representation of the domain.

In general applications where the geometry is not too complex and irregular, quadrilateral elements are better than triangular ones. The advantages of quadrilateral elements over triangular elements are that the computation time for the construction of matrices and vectors are reduced because only one half of the number of elements is needed, and solutions are in general more accurate with respect to the same number of unknowns, especially on orthogonal elements. These advantages are more evident in 3D calculations (Turek [1999]).

4.2.3 Finite element interpolation

The second basic feature of the finite element method is the construction of a finite dimensional space V_h that is a suitable approximation of the infinite dimensional space V . In the finite element method the functions $v_h \in V_h$ are piecewise-polynomials, i.e., for each $K \in \mathcal{T}_h$ the space

$$P_K := \{v_{h|K} \mid v_h \in V_h\}$$

consists of algebraic polynomials.

To be precise, let us denote by $\mathbb{P}_k, k \geq 0$, the space of polynomials of degree less than or equal to k in the variables x_1, \dots, x_d , and by \mathbb{Q}_k the space of polynomials that are of degree less than or equal to k with respect to each variable x_1, \dots, x_d .

We can now define the most commonly used spaces V_h . If we consider the case where the reference polyhedrons are n-simplex we set

$$V_h = V_h^k := \{v_h \in C^0(\bar{\Omega}) \mid v_{h|K} \in \mathbb{P}_k \quad \forall K \in \mathcal{T}_h\}, \quad k \geq 1, \quad (4.17)$$

which will be called the space of *triangular finite elements*. Alternatively, we can drop the additional constraint that $v_h \in C^0(\bar{\Omega})$ and set

$$V_h = Y_h^k := \{v_h \in L^2(\Omega) \mid v_{h|K} \in \mathbb{P}_k \quad \forall K \in \mathcal{T}_h\}. \quad (4.18)$$

In the case where the reference polyhedrons are n-cube we set

$$V_h = V_h^k := \{v_h \in C^0(\bar{\Omega}) \mid v_h|_K \circ T_K \in \mathbb{Q}_k \quad \forall K \in \mathcal{T}_h\} \quad , \quad k \geq 1, \quad (4.19)$$

which is the space of *parallelepipedal finite elements*.

In both cases, (4.17) and (4.19), it is worthwhile to notice that

$$V_h^k \subset H^1(\Omega) \quad \forall k \geq 1. \quad (4.20)$$

This result is a consequence of the following theorem

Theorem 4.2.1. *A function $v: \Omega \rightarrow \mathbb{R}$ belongs to $H^1(\Omega)$ if and only if*

- $v|_K \in H^1(K)$ for each $K \in \mathcal{T}_h$;
- for each common face $F = K_1 \cap K_2$, $K_1, K_2 \in \mathcal{T}_h$, the trace on F of $v|_{K_1}$ and $v|_{K_2}$ is the same.

This is an important result since the displacement and velocity unknowns of the FSI equations belong to the Sobolev space H^1 and consequently can be approximated by means of functions in the spaces (4.17) or (4.19). Instead, in the case (4.18) we have

$$Y_h^1 \subset L^2(\Omega). \quad (4.21)$$

As we will see further, the pressure unknown of the FSI equations belongs to the more bigger space L^2 . This implies that the space Y_h^1 is the natural finite dimensional space for the approximation of the FSI pressure solution.

An important point is concerned with the choice of a set of *degrees of freedom* on each element K (i.e., the parameters that allow to uniquely identify a function in \mathbb{P}_k or \mathbb{Q}_k). This choice depends on the space of polynomials (e.g., the space of triangular or parallelepipedal finite elements) and its degree. For instance, if we consider the space V_h^1 defined in (4.17) or (4.19) the degrees of freedom on each element K are the values of v_h at the vertices of each K . In the next subsection we will describe the properties and the location of the degrees of freedom of the finite element that will be used in this thesis to approximate the FSI solution.

We are now in the position to construct a *Lagrangian basis* for V_h^k . In particular, by denoting \mathbf{x}_j , $j = 1, \dots, N_h$, the global set of nodes in $\bar{\Omega}$, a sufficient

4. DISCRETIZATION PROCEDURE

condition to determine a basis for V_h^k is to select those functions $\phi_i \in V_h^k$ such that

$$\phi_i(\mathbf{x}_j) = \delta_{ij}, \quad i, j = 1, \dots, N_h. \quad (4.22)$$

The restriction of a basis function ϕ_i to an element that owns the node \mathbf{x}_i is called *shape function*. It is important to notice that the support of each shape function is relatively small since it is given by a few elements of the triangulation. This is good for computational efficiency because it leads to sparse stiffness matrices.

Once we have identified the degrees of freedom and the shape functions, the set of basis functions $\{\phi_i\}_{i=1}^{N_h}$ can be used to expand the approximate solution over the whole domain in terms of the degrees of freedom u_i

$$u_h(\mathbf{x}, t) = \sum_{i=1}^{N_h} u_i(t) \phi_i(\mathbf{x}) \quad \forall \mathbf{x} \in \Omega, \quad (4.23)$$

where N_h is the total number of degrees of freedom. If we consider the degrees of freedom u_i that belongs to the generic element K the solution u can be locally interpolated by means of local basis functions $\phi_i^{(k)}$ (also called shape functions) such that

$$u_h(\mathbf{x}, t) = \sum_{i=1}^{N_e} u_i(t) \phi_i^{(k)}(\mathbf{x}) \quad \forall \mathbf{x} \in K, \quad (4.24)$$

where N_e is the local number of degrees of freedom for the element K .

4.2.4 Conforming $\mathbf{Q}_2\mathbf{P}_1$ Element

The choice of a finite element depends on the type of problem, the robustness, the accuracy, the efficiency and the available time. The simplest way of satisfying the convergence requirements is to use elements that are conforming. A conforming finite element is one which is a subspace of the element space for the continuous problem. The conforming finite elements are more accurate compared to non-conforming ones but they require more computing time. The incompressibility constraint of the fluid and solid velocity requires that the finite element spaces pair are chosen in order to satisfy the *inf-sup* or *Ladyzhenskaya-Babuška-Brezzi* condition (see Brezzi & Fortin [1991]; Girault & P.-A. [1986]). We employed

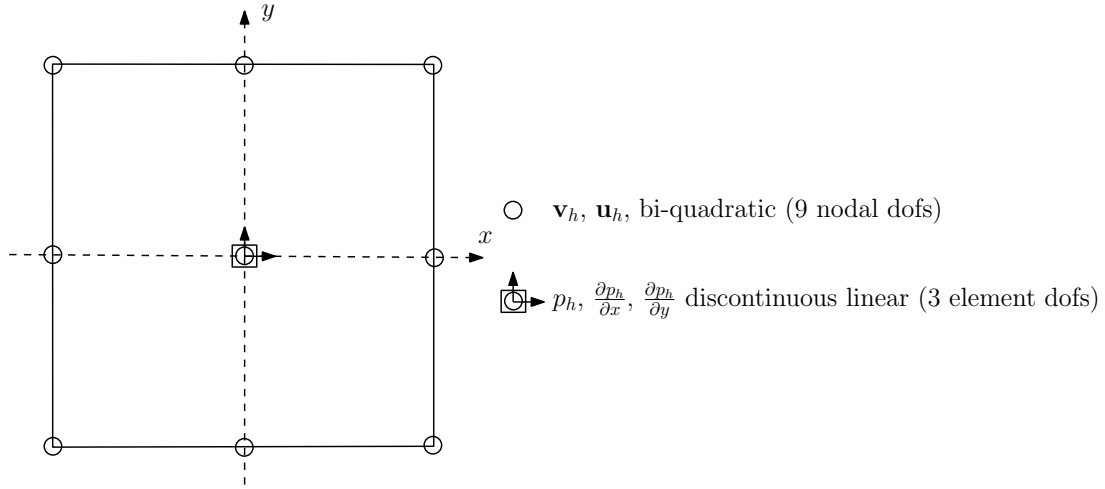


Figure 4.1: Location of the degrees of freedom for the (Crouzeix-Raviart) Q_2P_1 element.

the LBB-stable conforming bi(tri)-quadratic, discontinuous linear Q_2P_1 pair in two(three)-dimension because it is a good compromise between computing time and accuracy. In Fortin [1981] the Q_2P_1 finite element pair is referred to be one of the most accurate and robust finite element pair for highly viscous incompressible flow computations.

In the two-dimensional case, the basis function for this element are bi-quadratic polynomials on the reference square element $\hat{K} = [-1, 1]^2$ for the approximation of the displacement and the velocity solution and linear (discontinuous) polynomials for the approximation of the pressure. See Figure 4.1 for the location of the degrees of freedom on the reference square \hat{K} .

Let consider for each element $K \in \mathcal{T}_h$ the invertible transformation $\psi_K: \hat{K} \rightarrow K$ from the reference square \hat{K} to the quadrilateral K . Therefore the local basis on the reference element for $Q_2(K)$ is defined as

$$Q_2(K) = \{q \circ \psi_K^{-1} : q \in \text{span} \langle 1, x, y, x^2, y^2, x^2y, xy^2, x^2y^2 \rangle\},$$

4. DISCRETIZATION PROCEDURE

or

$$Q_2(K) = \text{span}\left\{(1-x^2)(1-y^2), \frac{1}{2}(1-x^2)(y-y^2), \frac{1}{2}(1-x^2)(y+y^2), \right. \\ \left. \frac{1}{2}(x-x^2)(1-y^2), \frac{1}{4}(x-x^2)(y-y^2), \frac{1}{4}(x-x^2)(y+y^2), \right. \\ \left. \frac{1}{2}(x+x^2)(1-y^2), \frac{1}{4}(x+x^2)(y-y^2), \frac{1}{4}(x+x^2)(y+y^2)\right\},$$

with nine local degrees of freedom located at the vertices, midpoints of the edges and in the center of the quadrilateral. This choice of the number and the location of the degrees of freedom is such that the subspace Q_2 coincides with the subspace V_h^2 defined in (4.19). The space $P_1(K)$ consists of linear functions defined by

$$P_1(T) = \{q \circ \psi_K^{-1} : q \in \text{span} \langle 1, x, y \rangle\}, \quad (4.25)$$

with the function value and both partial derivatives located in the center of the quadrilateral, as its three local degrees of freedom. This choice of the number and the location of the degrees of freedom is such that the subspace P_1 coincides with the subspace Y_h^1 defined in (4.18). Since the displacement and velocity solution of the FSI equations belong to the Sobolev space H^1 and the pressure to the Lebesgue space L^2 , from (4.20) and (4.21) we deduce that this finite element is conforming.

The Crouzeix-Raviart finite element has 39 degrees of freedom for each element in the case of the FSI displacement, velocity, pressure formulation in two dimensions and 166 degrees of freedom for 3D computations. This high number of degrees of freedom leads to prohibitive time-dependent computations, in particular in the three-dimensional case, if the parallel architecture of the modern computers is not exploited.

4.3 Temporal discretization

In this section we address the issue of time-discretization for initial-boundary value problems governed by parabolic or hyperbolic differential equation. The abstract problem 4.1 needs to be discretized with respect to both the time and

space variables.

The space discretization is performed firstly and can be carried out by the Galerkin finite element method previously described. The resulting problem is a system of coupled first order ordinary differential equations in time. This approach is known as *method of lines* or *semi-discrete* approximation in literature.

The following step is to choose an appropriate time stepping scheme that should not only be accurate in time, but also stable for different time steps.

In this section we present some methods of time integration of a system of ordinary differential equations that are massively used in numerical analysis.

4.3.1 Theta-scheme method

A simple and flexible choice for the time-discretization of a system of ordinary differential equations is the θ -scheme method, which has as particular cases the single step Backward Euler and Crank-Nicholson schemes, and also multi-step schemes such as the strongly A-stable Fractional-step- θ -scheme.

Let X be a vector that contains all the degrees of freedom that are generated in the spatial discretization process of the FSI equations. Let us assume that the FSI initial value problem can be written in the following form, with $X(t) \in \mathbb{R}^m$

$$\begin{cases} \frac{dX}{dt} + f(X, t) = 0 & \forall t > 0, \\ X(0) = X_0. \end{cases} \quad (4.26)$$

Given X^n at time $t = t^n$ and $\Delta t = t^{n+1} - t^n$, the method consists in solving for $X = X^{n+1}$

$$X^{n+1} + \theta \Delta t f(X^{n+1}, t^{n+1}) = X^n - (1 - \theta) \Delta t f(X^n, t^n). \quad (4.27)$$

The time step Δt can vary in time and the parameter θ is to be taken in the interval $[0, 1]$.

If $\theta = 0$ the explicit *Forward Euler* scheme is recovered as follows

$$X^{n+1} + \Delta t f(X^n, t^n) = X^n. \quad (4.28)$$

4. DISCRETIZATION PROCEDURE

Explicit time-stepping schemes have been commonly used in the past in non-stationary flow calculations. The advantages of this method are its easy implementation and parallelization and the low-cost per time step. The drawback is that it requires very small time steps for stability reasons, especially if the mesh size is very small compared to the velocity. The required small time steps leads to prohibitive treatment of long time flow simulations.

Due to the high stiffness of the system of ordinary differential equations obtained applying the FEM method and to the development of efficient non-linear and linear solvers, implicit schemes are preferable. Implicit schemes are stable over a wide range of time steps, they can be unconditionally stable under some hypothesis and they have been revealed excellent iterative schemes for obtaining steady-state solutions. The drawbacks of implicit schemes are the difficulty of implementation and parallelization and the high cost per time-step compared to explicit schemes. Due to their stability and high cost per time-step, large time steps are preferable to reduce the computational time. Unfortunately, large time steps lead to inaccurate fully transient solutions and to the deterioration or, in the worst cases, to the failure of the convergence of the linear solver.

The implicit schemes that are more frequently used are the first-order *Backward Euler* scheme (BE) or the second-order *Crank-Nicholson* scheme (CN) that belongs to the *One-step- θ -schemes* family.

The Backward Euler scheme is recovered from (4.27) with $\theta = 1$

$$X^{n+1} + \Delta t f(X^{n+1}, t^{n+1}) = X^n. \quad (4.29)$$

This method has the nice feature to be strongly A-stable, which means that the numerical solution X is bounded, but it is only first-order accurate. These characteristics indicate that the BE scheme is a good choice for steady-state calculations.

A second-order accurate scheme can be achieved from (4.27) with $\theta = 1/2$, obtaining

$$X^{n+1} + \frac{\Delta t}{2} f(X^{n+1}, t^{n+1}) = X^n - \frac{\Delta t}{2} f(X^n, t^n). \quad (4.30)$$

This scheme is called Crank-Nicholson and differently from the Backward Euler scheme is not strongly A-stable, it has a weak damping property and can

occasionally suffers from numerical instability.

4.3.2 Generalized alpha method

The need of development a step-by-step time integration algorithm with algorithmic damping in the solution process of structural dynamics problems has been long recognized. In particular, it is desirable to have the possibility to control the numerical dissipation in the higher frequency modes, since the spatial resolution of these high frequency modes is poor if the spatial domain is partitioned using standard finite elements. The advantage of using numerical algorithms with high-frequency damping is the improvement of the convergence of iterative equation solvers in the solution process of highly nonlinear problems. However, the effect of this damping should not provoke a loss of accuracy nor introduce excessive algorithmic damping in the important low frequency modes. For example, the Newmark family of algorithms (Newmark [1959]) gives the possibility to damp out high frequency modes but they are only first-order accurate and are too dissipative in the low frequency spectrum. Numerous dissipative algorithms have been developed that attain high-frequency dissipation with little low-frequency damping while maintaining second-order accuracy; see, e.g., the θ method of Wilson (Wilson [1968]), the HHT- α method of Hilber, Hughes and Taylor (Hilber *et al.* [1977]), the WBZ- α of Wood, Bossak, and Zienkiewicz (Wood *et al.* [1981]), the ρ method of Bazzi and Anderheggen (Bazzi & Anderheggen [1982]) and the θ_1 method of Hoff and Pahl (Hoff & Pahl [1988a,b]). In the paper of Chung & Hulbert [1993], a new family of one-step, three stage, numerically dissipative time integration algorithms has been developed, which is called the *generalized- α method* and contains the HHT- α and WBZ- α algorithms as particular cases. This integration method can be seen as an improvement of the previous algorithms since it is able to minimize the low frequency dissipation for a given desired amount of high-frequency dissipation. Recently, the generalized- α method has been extended and analyzed to computational fluid-dynamics (i.e., from a second-order system to a first-order system) and successfully applied to large scale turbulence simulation (Jansen *et al.* [2000]).

Let us consider for simplicity the matrix equation of linear structural dynamics

4. DISCRETIZATION PROCEDURE

$$\mathbf{M}\mathbf{a} + \mathbf{C}\mathbf{v} + \mathbf{K}\mathbf{d} = \mathbf{F}, \quad (4.31)$$

where \mathbf{M} , \mathbf{C} and \mathbf{K} are the mass, damping, and stiffness matrices, respectively, \mathbf{F} is the vector of applied loads (a given function of time), $\mathbf{a} = \frac{d\mathbf{v}}{dt}$, $\mathbf{v} = \frac{d\mathbf{d}}{dt}$ and \mathbf{d} are the vector of acceleration, velocity and displacement unknowns, respectively. The initial value problem consists of finding a function of time $\mathbf{d}(t)$ which satisfies (4.31) for all $t \in [0, T]$, $T > 0$, and the initial conditions

$$\mathbf{d}(0) = \mathbf{d}_0, \quad \mathbf{v}(0) = \mathbf{v}_0, \quad (4.32)$$

where \mathbf{d}_0 and \mathbf{v}_0 are given vectors of initial displacements and velocities, respectively. Let $0 = t^0 < t^1 < \dots < t^n = T$ be a partition of the time interval of the simulation $I = [0, T]$, which we suppose uniform for the sake of simplicity. We denote the time step with $\delta t = t^{n+1} - t^n$, for $0 \leq n \leq N - 1$. Let us denote by \mathbf{d}_n , \mathbf{v}_n and \mathbf{a}_n the approximations to $\mathbf{d}(t^n)$, $\mathbf{v}(t^n)$ and $\mathbf{a}(t^n)$, respectively. The generalized- α method applied to the linear structural dynamics has the following form

Given \mathbf{d}_0 and \mathbf{v}_0 , find \mathbf{d}_{n+1} , \mathbf{v}_{n+1} and \mathbf{a}_{n+1} such that, for each $0 < n < N - 1$ we have

$$\mathbf{d}_{n+1} = \mathbf{d}_n + \delta t \mathbf{v}_n + \delta t^2 \left(\left(\frac{1}{2} - \beta \right) \mathbf{a}_n + \beta \mathbf{a}_{n+1} \right), \quad (4.33)$$

$$\mathbf{v}_{n+1} = \mathbf{v}_n + \delta t \left((1 - \gamma) \mathbf{a}_n + \gamma \mathbf{a}_{n+1} \right), \quad (4.34)$$

$$\mathbf{M}\mathbf{a}_{n+1-\alpha_m} + \mathbf{C}\mathbf{v}_{n+1-\alpha_f} + \mathbf{K}\mathbf{d}_{n+1-\alpha_f} = \mathbf{F}(t_{n+1-\alpha_f}), \quad (4.35)$$

$$\mathbf{a}_0 = \mathbf{M}^{-1}(\mathbf{F}(0) - \mathbf{C}\mathbf{v}_0 - \mathbf{K}\mathbf{d}_0), \quad (4.36)$$

where

$$\mathbf{d}_{n+1-\alpha_f} = (1 - \alpha_f)\mathbf{d}_{n+1} + \alpha_f\mathbf{d}_n, \quad (4.37)$$

$$\mathbf{v}_{n+1-\alpha_f} = (1 - \alpha_f)\mathbf{v}_{n+1} + \alpha_f\mathbf{v}_n, \quad (4.38)$$

$$\mathbf{a}_{n+1-\alpha_m} = (1 - \alpha_m)\mathbf{a}_{n+1} + \alpha_m\mathbf{a}_n, \quad (4.39)$$

$$t_{n+1-\alpha_f} = (1 - \alpha_f)t_{n+1} + \alpha_f t_n. \quad (4.40)$$

The displacement and velocity update Eqs. (4.33) and (4.34) are identical to those of the Newmark algorithm. The balance equation is effectively a combination of the HHT- α and WBZ- α balance equations. In fact, using appropriate expressions for γ and β , if we set $\alpha_m = 0$, the algorithm reduces to the HHT- α method; $\alpha_f = 0$ produces the WBZ- α method; $\alpha_m = \alpha_f = 0$ gives rise to the Newmark family. The generalized- α method is second-order accurate and unconditionally stable, provided

$$\gamma = \frac{1}{2} - \alpha_m + \alpha_f, \quad \alpha_m \leq \alpha_f \leq \frac{1}{2}, \quad \beta \geq \frac{1}{4} + \frac{1}{2}(\alpha_f - \alpha_m). \quad (4.41)$$

The free parameters α_m , α_f and β can be chosen in order to minimize the low-frequency dissipation for a given user-specified level of high-frequency dissipation, denoted by the parameter ρ_∞ . The authors Chung and Hulbert prescribe to use the following expressions as an optimal combination of high-frequency and low-frequency dissipation

$$\beta = \frac{1}{4}(1 - \alpha_m + \alpha_f)^2, \quad \alpha_m = \frac{2\rho_\infty - 1}{\rho_\infty + 1}, \quad \alpha_f = \frac{\rho_\infty}{\rho_\infty + 1}. \quad (4.42)$$

In the paper of [Jansen *et al.* \[2000\]](#) the authors performed the analysis of the generalized- α method applied to a linear symmetric system of ordinary differential equations. They found that (4.41) are still valid for a first-order system as sufficient conditions for a second-order accuracy. The extension of the algorithm (4.33)-(4.40) to the full semi-discretized Navier-Stokes equations leads to a non-linear system of algebraic equations to be solved at each time step. If we denote by \mathbf{M} the mass matrix, \mathbf{K} the matrix containing the advective and diffusive term, \mathbf{Y} the vector of nodal values of the solution and $\dot{\mathbf{Y}}$ the vector of nodal time derivatives of the solution, the algorithm reads

$$\mathbf{M}\dot{\mathbf{Y}}_{n+\alpha_m} - \mathbf{K}(\mathbf{Y}_{n+\alpha_f}) = \mathbf{0}, \quad (4.43)$$

$$\mathbf{Y}_{n+1} = \mathbf{Y}_n + \delta t((1 - \gamma)\dot{\mathbf{Y}}_n + \gamma\dot{\mathbf{Y}}_{n+1}), \quad (4.44)$$

$$\mathbf{Y}_{n+\alpha_f} = \alpha_f \mathbf{Y}_n + (1 - \alpha_f)\mathbf{Y}_{n+1}, \quad (4.45)$$

$$\dot{\mathbf{Y}}_{n+\alpha_m} = \alpha_m \dot{\mathbf{Y}}_n + (1 - \alpha_m)\dot{\mathbf{Y}}_{n+1}. \quad (4.46)$$

4. DISCRETIZATION PROCEDURE

4.4 Weak formulation

In the first part of this section the continuous weak incompressible fluid-structure interaction formulation will be derived. We will show that starting from the weak form of the momentum balance equation, *a priori* energy balance can be obtained. In the second part we will derive the fully-discretized formulation using the Galerkin-Finite Element Method for the space discretization and the Backward Euler as time-integration scheme for both fluid and solid equations. In the last part the *unconditionally stability* of the Backward Euler scheme applied to a fully homogeneous Dirichlet fluid-structure interaction problem will be proved.

4.4.1 Continuous weak formulation

We have seen in section 3.4 that the coupling between the fluid and the solid model determines the missing boundary conditions, which consist of imposing the continuity of the velocity and the stress at the interface Γ_t^i in the following form

$$\mathbf{v}^f|_{\Gamma_t^i} = \mathbf{v}^s|_{\Gamma_t^i}, \quad (4.47)$$

$$\boldsymbol{\sigma}^f \cdot \mathbf{n}^f|_{\Gamma_t^i} + \boldsymbol{\sigma}^s \cdot \mathbf{n}^s|_{\Gamma_t^i} = \mathbf{0}. \quad (4.48)$$

To write the weak formulation of the coupled problem, let us consider the following functional spaces

$$\begin{aligned} \mathbf{U} &= \{\boldsymbol{\zeta} \in L^\infty(I, \mathbf{H}^1(\Omega)) : \boldsymbol{\phi}|_{\Gamma_D} = \mathbf{0}\}, \\ \mathbf{V} &= \{\boldsymbol{\phi} \in L^2(I, \mathbf{H}^1(\Omega)) \cap L^\infty(I, \mathbf{L}^2(\Omega)) : \boldsymbol{\phi}|_{\Gamma_D} = \mathbf{0}\}, \\ \mathbf{V}_g &= \{\boldsymbol{\phi} \in L^2(I, \mathbf{H}^1(\Omega)) \cap L^\infty(I, \mathbf{L}^2(\Omega)) : \boldsymbol{\phi}|_{\Gamma_D} = \mathbf{g}\}, \\ P &= \{\psi \in L^2(I, L^2(\Omega))\}, \end{aligned} \quad (4.49)$$

where $I = [0, T]$ denotes the time interval of interest, Γ_D is the portion of the boundary where Dirichlet boundary conditions are imposed and \mathbf{g} is a user-defined functions. In addition, we denote with $(\cdot, \cdot)_f$, $(\cdot, \cdot)_s$ and (\cdot, \cdot) the $L^2(\Omega^f)$, $L^2(\Omega^s)$

and $L^2(\Omega)$ inner product, respectively.

The variational formulation of the fluid-structure equations can be obtained through the usual technique by multiplying the equations (3.100)-(3.102) with appropriate test functions, integrating over the domain Ω , performing integrations by parts and taking into account the boundary and interface conditions. This procedure leads at each time t to the following weak global formulation for the fluid-structure interaction problem

Given $\mathbf{g} \in \mathbf{H}^{1/2}(\Gamma_D)$ and $\mathbf{h} \in \mathbf{L}^2(\Gamma_N)$, find $\mathbf{u} \in \mathbf{U}$, $\mathbf{v} \in \mathbf{V}_g$, $p \in P$ such that, for each t we have

$$\left(\frac{\partial \mathbf{u}}{\partial t}, \boldsymbol{\zeta}\right) = (\mathbf{v}, \boldsymbol{\zeta})_s - (k \nabla \mathbf{u}, \nabla \boldsymbol{\zeta})_f, \quad (4.50)$$

$$\begin{aligned} \left(J \frac{\partial \mathbf{v}}{\partial t}, \boldsymbol{\phi}\right)_f + (\beta J \frac{\partial \mathbf{v}}{\partial t}, \boldsymbol{\phi})_s &= -(J \nabla \mathbf{v} \mathbf{F}^{-1} (\mathbf{v} - \frac{\partial \mathbf{u}}{\partial t}), \boldsymbol{\phi})_f \\ &+ (J p \mathbf{F}^{-T}, \nabla \boldsymbol{\phi}) - (J \mu \nabla \mathbf{v} \mathbf{F}^{-1} \mathbf{F}^{-T}, \nabla \boldsymbol{\phi})_f \end{aligned} \quad (4.51)$$

$$- (\mathbf{F} \boldsymbol{\Sigma}, \nabla \boldsymbol{\phi})_s + \int_{\Gamma_N} \mathbf{h} \cdot \boldsymbol{\phi} \, d\gamma$$

$$0 = (J - 1, \psi)_s + (\nabla \cdot (J \mathbf{v} \mathbf{F}^{-T}), \psi)_f, \quad (4.52)$$

$$\mathbf{u}|_{t=0} = \mathbf{u}_0, \quad \mathbf{v}|_{t=0} = \mathbf{v}_0,$$

for all $(\boldsymbol{\zeta}, \boldsymbol{\phi}, \psi) \in (\mathbf{U}, \mathbf{V}, P)$.

It is worth noting that by the coupling conditions (3.88), (3.89) and the particular choice of the fluid-structure test functions, the two boundary terms that come out from the integration by parts at the fluid and the structure interface Γ_0^i cancel out. This assures that forces at the interface are correctly computed.

The rest of this paragraph is devoted to the *a priori* energy analysis applied to the general fluid-structure interaction problem. As expected, dissipation only comes from the fluid viscosity and no energy losses occur at the fluid-structure interface.

Theorem 4.4.1 (Energy Balance). *Assume that the coupled fluid-structure system is isolated, i.e., $\mathbf{g} = \mathbf{0}$ and $\Gamma_D = \partial\Omega$, and that exist a solution $(\mathbf{u}, \mathbf{v}, \mathbf{p}) \in \mathbf{U} \times \mathbf{V}_g \times P$ such that equations (4.50), (4.51) and (4.52) are satisfied for all*

4. DISCRETIZATION PROCEDURE

$(\zeta, \phi, \psi) \in \mathbf{U} \times \mathbf{V} \times P$, then the following energy balance holds

$$\frac{d}{dt} \left[\int_{\Omega_t^f} \frac{\rho}{2} |\mathbf{v}|^2 d\mathbf{x} + \int_{\Omega_0^s} \frac{\rho_0}{2} |\mathbf{v}|^2 d\mathbf{x} + \int_{\Omega_0^s} \Psi(\mathbf{F}) d\mathbf{x} \right] + \int_{\Omega_t^f} \mu |\nabla \mathbf{v}|^2 d\mathbf{x} = 0. \quad (4.53)$$

Proof. Using the velocity as a test function and transforming some of the integrals to the current domain, the momentum balance equation (4.51) becomes

$$\begin{aligned} \int_{\Omega_0^f} \rho J \frac{\partial \mathbf{v}}{\partial t} \cdot \mathbf{v} d\mathbf{x} + \int_{\Omega_0^s} \rho J \frac{\partial \mathbf{v}}{\partial t} \cdot \mathbf{v} d\mathbf{x} = & - \int_{\Omega_t^f} \rho \nabla \mathbf{v} \left(\mathbf{v} - \frac{\partial \mathbf{u}}{\partial t} \right) \cdot \mathbf{v} d\mathbf{x} + \int_{\Omega_t} p \nabla \cdot \mathbf{v} d\mathbf{x} + \\ & - \int_{\Omega_t^f} \mu |\nabla \mathbf{v}|^2 d\mathbf{x} - \int_{\Omega_0^s} \mathbf{F} \Sigma \cdot \nabla \mathbf{v} d\mathbf{x}. \end{aligned} \quad (4.54)$$

The second term in the right-end side vanish due to the incompressibility constraint. Using the equation of conservation of mass (3.57), the second term of the left hand side can be rewritten as

$$\int_{\Omega_0^s} \rho J \frac{\partial \mathbf{v}}{\partial t} \cdot \mathbf{v} d\mathbf{x} = \frac{d}{dt} \int_{\Omega_0^s} \frac{\rho_0}{2} |\mathbf{v}|^2 d\mathbf{x}. \quad (4.55)$$

For the mass term in the fluid, by using the Euler expansion formula (3.45) recasted to the ALE mapping and the pushing the integrals to the current domain, we have

$$\begin{aligned} \int_{\Omega_0^f} \rho J \frac{\partial \mathbf{v}}{\partial t} \cdot \mathbf{v} d\mathbf{x} = & \int_{\Omega_0^f} \frac{\rho}{2} \frac{\partial (J |\mathbf{v}|^2)}{\partial t} d\mathbf{x} - \int_{\Omega_0^f} \frac{\rho}{2} J (\nabla \cdot \frac{\partial \mathbf{u}}{\partial t}) |\mathbf{v}|^2 d\mathbf{x} = \\ & \frac{d}{dt} \left[\int_{\Omega_t^f} \frac{\rho}{2} |\mathbf{v}|^2 d\mathbf{x} \right] - \int_{\Omega_t^f} \frac{\rho}{2} (\nabla \cdot \frac{\partial \mathbf{u}}{\partial t}) |\mathbf{v}|^2 d\mathbf{x}. \end{aligned} \quad (4.56)$$

For the convective term, since $\nabla \cdot \mathbf{v} = 0$ in the current domain, integrating by parts, using the homogeneous boundary conditions and the equality $\mathbf{v}^f = \frac{\partial \mathbf{u}^f}{\partial t}$ on the interface Γ_t^i , we have

$$\begin{aligned} \int_{\Omega_t^f} \rho \nabla \mathbf{v} \left(\mathbf{v} - \frac{\partial \mathbf{u}}{\partial t} \right) \cdot \mathbf{v} d\mathbf{x} = & \int_{\Omega_t^f} \frac{\rho}{2} \left(\mathbf{v} - \frac{\partial \mathbf{u}}{\partial t} \right) \cdot \nabla |\mathbf{v}|^2 d\mathbf{x} = \\ & \int_{\Omega_t^f} \frac{\rho}{2} (\nabla \cdot \frac{\partial \mathbf{u}}{\partial t}) |\mathbf{v}|^2 d\mathbf{x}. \end{aligned} \quad (4.57)$$

The fourth term in the right end side of (4.54) can be rewritten by using the identity $\nabla \mathbf{v} = \frac{d\mathbf{F}}{dt}$ as

$$\int_{\Omega_0^s} \mathbf{F}\Sigma \cdot \nabla \mathbf{v} \, d\mathbf{x} = \int_{\Omega_0^s} \frac{\partial \Psi}{\partial \mathbf{F}} \cdot \nabla \mathbf{v} \, d\mathbf{x} = \int_{\Omega_0^s} \frac{\partial \Psi}{\partial \mathbf{F}} \cdot \frac{d\mathbf{F}}{dt} \, d\mathbf{x} = \frac{d}{dt} \int_{\Omega_0^s} \Psi(\mathbf{F}) \, d\mathbf{x}. \quad (4.58)$$

Using (4.55), (4.56), (4.57), (4.58) and the incompressibility constraint (4.52) in (4.54), the energy balance (4.53) is obtained, which completes the proof. \square

4.4.2 Space-time discretized weak formulation

The weak coupled formulation is now discretized in space and time. Let $0 = t^0 < t^1 < \dots < t^n = T$ be a partition of the time interval of the simulation $I = [0, T]$, which we suppose uniform for the sake of simplicity. We denote the time step with $\delta t = t^{n+1} - t^n$, for $0 \leq n \leq N - 1$. For the space discretization of the fluid-structure interaction problem (4.50)-(4.52), let us define four finite element subspaces $\mathbf{U}_h \subset \mathbf{U}$, $\mathbf{V}_h \subset \mathbf{V}$, $\mathbf{V}_{h,g} \subset \mathbf{V}_g$, $P_h \subset P$ that in the case of the finite element $Q_2 P_1$ disc pair read as follows

$$\begin{aligned} \mathbf{U}_h &= \{ \mathbf{u}_h \in [C(\Omega_h)]^2, \quad \mathbf{u}_h|_K \in [Q_2(K)]^2 \quad \forall K \in \mathcal{T}_h, \quad \mathbf{u}_h|_{\Gamma_{h,D}} = \mathbf{0} \}, \\ \mathbf{V}_h &= \{ \mathbf{v}_h \in [C(\Omega_h)]^2, \quad \mathbf{v}_h|_K \in [Q_2(K)]^2 \quad \forall K \in \mathcal{T}_h, \quad \mathbf{v}_h|_{\Gamma_{h,D}} = \mathbf{0} \}, \\ \mathbf{V}_{h,g} &= \{ \mathbf{v}_h \in [C(\Omega_h)]^2, \quad \mathbf{v}_h|_K \in [Q_2(K)]^2 \quad \forall K \in \mathcal{T}_h, \quad \mathbf{v}_h|_{\Gamma_{h,D}} = \mathbf{g}_h^n \}, \\ P_h &= \{ p_h \in L^2(\Omega_h), \quad p_h|_K \in P_1(K) \quad \forall K \in \mathcal{T}_h \}, \end{aligned}$$

where K is one of the elements of the triangulation \mathcal{T}_h of the reference domain Ω and \mathbf{g}_h^n is the finite element approximation of $\mathbf{g}(t^n)$. Let us denote by \mathbf{u}_h^n the approximation of $\mathbf{u}(t^n)$, \mathbf{v}_h^n the approximation of $\mathbf{v}(t^n)$ and p_h^n the approximation of $p(t^n)$. Besides, the following shorthand notation will be used

$$\mathbf{F}^n = \mathbf{I} + \nabla \mathbf{u}_h^n, \quad J^n = \det \mathbf{F}^n, \quad (4.59)$$

$$\mathbf{F}^{n+\frac{1}{2}} = \frac{\mathbf{F}^n + \mathbf{F}^{n+1}}{2}, \quad J^{n+\frac{1}{2}} = \frac{J^n + J^{n+1}}{2}. \quad (4.60)$$

Then, using the Backward Euler scheme for the time-discretization, the fully-discretized problem reads

4. DISCRETIZATION PROCEDURE

Given $\mathbf{g}_h^{n+1} \in \mathbf{H}^{1/2}(\Gamma_{h,D})$ and $\mathbf{h}_h^{n+1} \in \mathbf{L}^2(\Gamma_{h,N})$, find $\mathbf{u}_h^{n+1} \in \mathbf{U}_h$, $\mathbf{v}_h^{n+1} \in \mathbf{V}_{h,g}$, $p_h^{n+1} \in P_h$ such that, for each $0 \leq n < N - 1$ we have

$$(\mathbf{u}_h^{n+1}, \boldsymbol{\zeta}) - (\mathbf{u}_h^n, \boldsymbol{\zeta}) - \delta t [(\mathbf{v}_h^{n+1}, \boldsymbol{\zeta})_s + (k \nabla \mathbf{u}_h^{n+1}, \nabla \boldsymbol{\zeta})_f] = 0, \quad (4.61)$$

$$\begin{aligned} & (J^{n+1} \mathbf{v}_h^{n+1}, \boldsymbol{\phi})_f + \beta(\mathbf{v}_h^{n+1}, \boldsymbol{\phi})_s - (J^n \mathbf{v}_h^n, \boldsymbol{\phi})_f - \beta(\mathbf{v}_h^n, \boldsymbol{\phi})_s \\ & \quad - \delta t (J^{n+1} p_h^{n+1}, \nabla \boldsymbol{\phi}(\mathbf{F}^{n+1})^{-1}) + \delta t (\mathbf{F}^{n+1} \boldsymbol{\Sigma}^{n+1}, \nabla \boldsymbol{\phi})_s \\ + \delta t \mu & (J^{n+1} \nabla \mathbf{v}_h^{n+1}(\mathbf{F}^{n+1})^{-1}, \nabla \boldsymbol{\phi}(\mathbf{F}^{n+1})^{-1})_f + \delta t (J^{n+\frac{1}{2}} \nabla \mathbf{v}_h^{n+1}(\mathbf{F}^{n+\frac{1}{2}})^{-1} \mathbf{v}_h^{n+1}, \boldsymbol{\phi})_f \\ & \quad - (J^{n+\frac{1}{2}} \nabla \mathbf{v}_h^{n+1}(\mathbf{F}^{n+\frac{1}{2}})^{-1}(\mathbf{u}_h^{n+1} - \mathbf{u}_h^n), \boldsymbol{\phi})_f \\ & \quad - ((\nabla \cdot (J^{n+\frac{1}{2}} \mathbf{u}_h^{n+1}(\mathbf{F}^{n+\frac{1}{2}})^{-T}) - \nabla \cdot (J^{n+\frac{1}{2}} \mathbf{u}_h^n(\mathbf{F}^{n+\frac{1}{2}})^{-T})) \mathbf{v}_h^{n+1}, \boldsymbol{\phi})_f \\ + \frac{\delta t}{2} & (\nabla \cdot (J^{n+\frac{1}{2}} \mathbf{v}_h^{n+1}(\mathbf{F}^{n+\frac{1}{2}})^{-T}) \mathbf{v}_h^{n+1}, \boldsymbol{\phi})_f - \delta t \int_{\Gamma_{h,N}} \mathbf{h}_h^{n+1} \cdot \boldsymbol{\phi} d\gamma = 0, \quad (4.62) \end{aligned}$$

$$(J^{n+1} - 1, \boldsymbol{\psi})_s + (\nabla \cdot (J^{n+1} \mathbf{v}_h^{n+1}(\mathbf{F}^{n+1})^{-T}), \boldsymbol{\psi})_f = 0, \quad (4.63)$$

$$\mathbf{u}_h^n|_{n=0} = \mathbf{u}_{h,0}, \quad \mathbf{v}_h^n|_{n=0} = \mathbf{v}_{h,0},$$

for all $(\boldsymbol{\zeta}, \boldsymbol{\phi}, \boldsymbol{\psi}) \in (\mathbf{U}_h, \mathbf{V}_h, P_h)$.

We can notice that we added two terms in the discrete formulation with respect to the continuous one, which are

$$\begin{aligned} & ((\nabla \cdot (J^{n+\frac{1}{2}} \mathbf{u}_h^{n+1}(\mathbf{F}^{n+\frac{1}{2}})^{-T}) - \nabla \cdot (J^{n+\frac{1}{2}} \mathbf{u}_h^n(\mathbf{F}^{n+\frac{1}{2}})^{-T})) \mathbf{v}_h^{n+1}, \boldsymbol{\phi})_f, \\ & \frac{\delta t}{2} (\nabla \cdot (J^{n+\frac{1}{2}} \mathbf{v}_h^{n+1}(\mathbf{F}^{n+\frac{1}{2}})^{-T}) \mathbf{v}_h^{n+1}, \end{aligned}$$

and some integrals are evaluated in the intermediate position between t^n and t^{n+1} . The reason for this is for stability purposes as it will be shown in the proof of the next theorem.

In each time step we have to find the vector $\mathbf{X}^{n+1} = (\mathbf{u}_h^{n+1}, \mathbf{v}_h^{n+1}, p_h^{n+1}) \in \mathbf{U}_h \times \mathbf{V}_h \times P_h$ such that

$$\mathcal{F}(\mathbf{X}^{n+1}) = \mathbf{0}, \quad (4.64)$$

where \mathcal{F} represents the system (4.61)-(4.63). The issue of solving numerically

this system will be addressed in the next Chapter. The rest of this paragraph is devoted to the stability analysis of the Backward Euler time-discretization scheme applied to the fluid-structure interaction equations discretized by the Galerkin finite element method. The next result states its unconditional stability.

Theorem 4.4.2 (Energy inequality). *Assume that the coupled fluid-structure system is isolated, i.e., $\mathbf{g}_h^{n+1} = \mathbf{0}$ and $\Gamma_{h,D} = \partial\Omega_h$, the structure is hyperelastic with a quadratic energy density $\Psi(\mathbf{F}^{n+1})$, the fluid-structure system is discretized in space by the finite element method and in time by the Backward Euler method, and that the following identity holds on each time-interval,*

$$\int_{\Omega_{n+1,h}^f} \psi_h \, d\mathbf{x} - \int_{\Omega_{n,h}^f} \psi_h \, d\mathbf{x} = \mathcal{JN}\mathcal{J}_{t^n}^{t^{n+1}} \left[\int_{\Omega_{t,h}^f} \psi_h (\nabla \cdot \frac{\partial \mathbf{u}_h}{\partial t}) \, d\mathbf{x} \right] \quad \forall \psi_h \in V_h, \quad (4.65)$$

where $\mathcal{JN}\mathcal{J}_{t^n}^{t^{n+1}}$ denotes the time integration scheme, then the following energy inequality holds

$$\begin{aligned} & \frac{1}{\delta t} \left[\int_{\Omega_{n+1,h}^f} \frac{\rho}{2} |\mathbf{v}_h^{n+1}|^2 \, d\mathbf{x} - \int_{\Omega_{n,h}^f} \frac{\rho}{2} |\mathbf{v}_h^n|^2 \, d\mathbf{x} \right. \\ & \quad \left. + \int_{\Omega_{0,h}^s} \frac{\rho_0}{2} |\mathbf{v}_h^{n+1}|^2 \, d\mathbf{x} - \int_{\Omega_{0,h}^s} \frac{\rho_0}{2} |\mathbf{v}_h^n|^2 \, d\mathbf{x} \right. \\ & \quad \left. + \int_{\Omega_{0,h}^s} \Psi(\mathbf{F}_h^{n+1}) \, d\mathbf{x} - \int_{\Omega_{0,h}^s} \Psi(\mathbf{F}_h^n) \, d\mathbf{x} \right] + \int_{\Omega_{n+1,h}^f} \mu |\nabla \mathbf{v}_h^{n+1}|^2 \, d\mathbf{x} \leq 0. \end{aligned} \quad (4.66)$$

Therefore, the Backward Euler method applied to the fluid-structure interaction equations in the monolithic discrete formulation is unconditionally stable in the energy norm.

Before giving the proof of this result, some remarks are in order:

- The energy balance (4.66) constitutes the discrete counterpart of (4.53).
- The relation (4.65) is one of the form of the Geometric Conservation Law (GCL), see Nobile [2001], suited for a finite element approximation. This constraint on the fluid domain displacement or, equivalently, on the ALE mapping \mathcal{A} , ensures that the continuous ALE transport formula (3.46) holds at the discrete level at each time interval. As reported in Nobile [2001], a

4. DISCRETIZATION PROCEDURE

sufficient condition for the fulfillment of (4.65) is to use a time integration scheme $\mathcal{N}\mathcal{T}_t^{n+1}$ for the ALE term of degree $d \cdot s - 1$, where d is the space dimension and s is the degree of the polynomial used to represent the time evolution of the nodal displacement within each time step. If we assume a linear time variation of the nodal displacement within each time step, the GCL is satisfied in 2D if we adopt the mid-point rule integration scheme.

Proof. We set $\phi = \mathbf{v}_h^{n+1}$ in (4.62) and $\psi = p_h^{n+1}$ in (4.63). For the mass term in the solid, using the inequality $\frac{a^2}{2} + \frac{b^2}{2} \geq a \cdot b$, we have

$$\frac{\rho_0}{\delta t} \left[\int_{\Omega_{0,h}^s} |\mathbf{v}_h^{n+1}|^2 d\mathbf{x} - \int_{\Omega_{0,h}^s} \mathbf{v}_h^n \mathbf{v}_h^{n+1} d\mathbf{x} \right] \geq \frac{\rho_0}{2\delta t} \left[\int_{\Omega_{0,h}^s} |\mathbf{v}_h^{n+1}|^2 d\mathbf{x} - \int_{\Omega_{0,h}^s} |\mathbf{v}_h^n|^2 d\mathbf{x} \right]. \quad (4.67)$$

On the other hand, thanks to (4.61), we have

$$\begin{aligned} \int_{\Omega_{0,h}^s} \mathbf{F}^{n+1} \Sigma^{n+1} : \nabla \mathbf{v}_h^{n+1} d\mathbf{x} &= \frac{1}{\delta t} \int_{\Omega_{0,h}^s} \mathbf{F}^{n+1} \Sigma^{n+1} : \nabla (\mathbf{u}_h^{n+1} - \mathbf{u}_h^n) d\mathbf{x} \\ &= \frac{1}{\delta t} \int_{\Omega_{0,h}^s} \mathbf{F}^{n+1} \Sigma^{n+1} : (\mathbf{F}^{n+1} - \mathbf{F}^n) d\mathbf{x} = \frac{1}{\delta t} \int_{\Omega_{0,h}^s} \frac{\partial \Psi(\mathbf{F}^{n+1})}{\partial \mathbf{F}} : (\mathbf{F}^{n+1} - \mathbf{F}^n). \end{aligned} \quad (4.68)$$

Therefore, since the density Ψ is assumed to be quadratic, we obtain

$$\frac{1}{\delta t} \int_{\Omega_{0,h}^s} \frac{\partial \Psi(\mathbf{F}^{n+1})}{\partial \mathbf{F}} : (\mathbf{F}^{n+1} - \mathbf{F}^n) \geq \frac{1}{\delta t} \left[\int_{\Omega_{0,h}^s} \Psi(\mathbf{F}^{n+1}) d\mathbf{x} - \int_{\Omega_{0,h}^s} \Psi(\mathbf{F}^n) d\mathbf{x} \right]. \quad (4.69)$$

For the mass term in the fluid, using the same inequality as we did before, we have

$$\begin{aligned} \frac{\rho}{\delta t} \left[\int_{\Omega_{n+1,h}^f} |\mathbf{v}_h^{n+1}|^2 d\mathbf{x} - \int_{\Omega_{n,h}^f} \mathbf{v}_h^n \mathbf{v}_h^{n+1} d\mathbf{x} \right] &\geq \frac{1}{\delta t} \left[\frac{\rho}{2} \int_{\Omega_{n+1,h}^f} |\mathbf{v}_h^{n+1}|^2 d\mathbf{x} \right. \\ &\quad \left. - \frac{\rho}{2} \int_{\Omega_{n,h}^f} |\mathbf{v}_h^n|^2 d\mathbf{x} \right] + \frac{1}{\delta t} \left[\frac{\rho}{2} \int_{\Omega_{n+1,h}^f} |\mathbf{v}_h^{n+1}|^2 d\mathbf{x} - \frac{\rho}{2} \int_{\Omega_{n,h}^f} |\mathbf{v}_h^{n+1}|^2 d\mathbf{x} \right]. \end{aligned} \quad (4.70)$$

By applying (4.65) with $\psi_h = \frac{\rho}{2\delta t} |\mathbf{v}_h^{n+1}|^2$ and mid-point rule as time integration

scheme to the last term, we finally get

$$\begin{aligned} \frac{\rho}{\delta t} \left[\int_{\Omega_{n+1,h}^f} |\mathbf{v}_h^{n+1}|^2 d\mathbf{x} - \int_{\Omega_{n,h}^f} \mathbf{v}_h^n \mathbf{v}_h^{n+1} d\mathbf{x} \right] &\geq \frac{1}{\delta t} \left[\frac{\rho}{2} \int_{\Omega_{n+1,h}^f} |\mathbf{v}_h^{n+1}|^2 d\mathbf{x} \right. \\ &\quad \left. - \frac{\rho}{2} \int_{\Omega_{n,h}^f} |\mathbf{v}_h^n|^2 d\mathbf{x} \right] + \frac{\rho}{2} \int_{\Omega_{n+\frac{1}{2},h}^f} \left(\nabla \cdot \frac{\mathbf{u}_h^{n+1} - \mathbf{u}_h^n}{\delta t} \right) |\mathbf{v}_h^{n+1}|^2 d\mathbf{x}. \end{aligned} \quad (4.71)$$

For the convective term, integrating by parts and using (4.61), we have

$$\begin{aligned} &\int_{\Omega_{n+\frac{1}{2},h}^f} \rho \nabla \mathbf{v}_h^{n+1} \left(\mathbf{v}_h^{n+1} - \frac{\mathbf{u}_h^{n+1} - \mathbf{u}_h^n}{\delta t} \right) \cdot \mathbf{v}_h^{n+1} d\mathbf{x} \\ &- \int_{\Omega_{n+\frac{1}{2},h}^f} \rho \left(\nabla \cdot \frac{\mathbf{u}_h^{n+1} - \mathbf{u}_h^n}{\delta t} \right) |\mathbf{v}_h^{n+1}|^2 d\mathbf{x} + \int_{\Omega_{n+\frac{1}{2},h}^f} \frac{\rho}{2} \nabla \cdot \mathbf{v}_h^{n+1} |\mathbf{v}_h^{n+1}|^2 d\mathbf{x} \\ &= \int_{\Omega_{n+\frac{1}{2},h}^f} \frac{\rho}{2} \left(\mathbf{v}_h^{n+1} - \frac{\mathbf{u}_h^{n+1} - \mathbf{u}_h^n}{\delta t} \right) \cdot \nabla |\mathbf{v}_h^{n+1}|^2 d\mathbf{x} \\ &- \int_{\Omega_{n+\frac{1}{2},h}^f} \rho \left(\nabla \cdot \frac{\mathbf{u}_h^{n+1} - \mathbf{u}_h^n}{\delta t} \right) |\mathbf{v}_h^{n+1}|^2 d\mathbf{x} + \int_{\Omega_{n+\frac{1}{2},h}^f} \frac{\rho}{2} \nabla \cdot \mathbf{v}_h^{n+1} |\mathbf{v}_h^{n+1}|^2 d\mathbf{x} \quad (4.72) \\ &= \int_{\partial\Omega_{n+\frac{1}{2},h}^f} \frac{\rho}{2} \left(\mathbf{v}_h^{n+1} - \frac{\mathbf{u}_h^{n+1} - \mathbf{u}_h^n}{\delta t} \right) \cdot \mathbf{n} |\mathbf{v}_h^{n+1}|^2 d\gamma \\ &- \int_{\Omega_{n+\frac{1}{2},h}^f} \frac{\rho}{2} \left(\nabla \cdot \frac{\mathbf{u}_h^{n+1} - \mathbf{u}_h^n}{\delta t} \right) |\mathbf{v}_h^{n+1}|^2 d\mathbf{x} = - \int_{\Omega_{n+\frac{1}{2},h}^f} \frac{\rho}{2} \left(\nabla \cdot \frac{\mathbf{u}_h^{n+1} - \mathbf{u}_h^n}{\delta t} \right) |\mathbf{v}_h^{n+1}|^2 d\mathbf{x}. \end{aligned}$$

For the dissipation term we have

$$\int_{\Omega_{n+1,h}^f} \mu \nabla \mathbf{v}_h^{n+1} \cdot \nabla \mathbf{v}_h^{n+1} d\mathbf{x} = \int_{\Omega_{n+1,h}^f} \mu |\nabla \mathbf{v}_h^{n+1}|^2 d\mathbf{x}. \quad (4.73)$$

By using the fluid and solid incompressibility constraint (4.63), the pressure term vanish

$$\int_{\Omega_{n+1,h}^f} p_h \nabla \cdot \mathbf{v}_h^{n+1} d\mathbf{x} = 0. \quad (4.74)$$

Finally, the energy balance (4.66) is obtained after summation of (4.67), (4.69), (4.71), (4.72), (4.73) and (4.74), which completes the proof. \square

4. DISCRETIZATION PROCEDURE

Chapter 5

Solvers

In this chapter, we describe the adopted numerical solution strategy of the nonlinear system arising in the numerical discretization of the fluid-structure equations coupled in a monolithic fashion. More specifically, the Newton-method and its variants will be presented together with a general introduction to direct and iterative solvers like Krylov subspace and multigrid solvers.

5.1 Introduction

We have seen in Chapter 4 that after discretization in time by the method of lines and in space by the Galerkin finite element method we arrived at a set of nonlinear algebraic equations for the unknown vector $\mathbf{X}^{n+1} = (\mathbf{u}_h^{n+1}, \mathbf{v}_h^{n+1}, p_h^{n+1})$

$$\mathcal{F}(\mathbf{X}^{n+1}) = \mathbf{0}. \quad (5.1)$$

Equivalently, the discrete set of equations (5.1) can also be rewritten as follows

$$\begin{aligned} (\mathbf{M}^f + \mathbf{M}^s)\mathbf{u}_h^{n+1} - \delta t(\mathbf{L}^f\mathbf{u}_h^{n+1} + \mathbf{M}^s\mathbf{v}_h^{n+1}) - \mathbf{Rhs}_u(\mathbf{u}_h^n) &= \mathbf{0}, \\ (\mathbf{M}^f + \beta\mathbf{M}^s)\mathbf{v}_h^{n+1} + \delta t\mathbf{C}_1^f(\mathbf{v}_h^{n+1}) + \frac{\delta t}{2}\mathbf{C}_2^f(\mathbf{v}_h^{n+1}) - \mathbf{C}_3^f(\mathbf{u}_h^{n+1}, \mathbf{v}_h^{n+1}) - \mathbf{C}_4^f(\mathbf{u}_h^{n+1}, \mathbf{v}_h^{n+1}) \\ + \delta t\mathbf{S}^f(\mathbf{v}_h^{n+1}) + \delta t\mathbf{S}^s(\mathbf{u}_h^{n+1}) - \delta t(\mathbf{B}^f + \mathbf{B}^s)(p_h^{n+1}) - \mathbf{Rhs}_v(\mathbf{v}_h^n) &= \mathbf{0}, \\ \mathbf{I}^s(\mathbf{u}_h^{n+1}) + (\mathbf{B}^f)^T(\mathbf{v}_h^{n+1}) &= \mathbf{0}, \end{aligned}$$

5. SOLVERS

where \mathbf{M}^s and \mathbf{M}^f are the mass matrices, \mathbf{L}^f is the lifting operator of the trace of the solid displacement on the fluid-solid interface that is responsible for the mesh motion in the fluid subdomain, \mathbf{C}_1^f and \mathbf{C}_3^f represent the convective term in the ALE formulation, \mathbf{C}_2^f and \mathbf{C}_4^f are the stabilization terms for the ALE convective term, \mathbf{S}^s and \mathbf{S}^f are the stress operators (elastic for the solid part and diffusive for the fluid), \mathbf{I}^s is the incompressibility constraint for the solid part and $(\mathbf{B}^f)^T$ the incompressibility constraint for the fluid part, \mathbf{B}^f and \mathbf{B}^s are the discrete gradient operators in the fluid and solid subdomain. All of the operators, apart of the dependencies indicated explicitly, depends on the displacement unknown through the deformation gradient and/or the Jacobian of the transformation. Besides, the right hand sides depend on the values of the unknowns in the previous time step. The definition of these quantities is reported below for sake of clarity

$$\begin{aligned}
\mathbf{M}^f \mathbf{u}_h^{n+1} &= (\mathbf{u}_h^{n+1}, \boldsymbol{\zeta})_f, \\
\mathbf{M}^s \mathbf{u}_h^{n+1} &= (\mathbf{u}_h^{n+1}, \boldsymbol{\zeta})_s, \\
\mathbf{L}^f \mathbf{u}_h^{n+1} &= (k(\mathbf{x}) \nabla \mathbf{u}_h^{n+1}, \nabla \boldsymbol{\zeta})_f, \\
\text{Rhs}_u(\mathbf{u}_h^n) &= (\mathbf{u}_h^n, \boldsymbol{\zeta}), \\
\mathbf{M}^f \mathbf{v}_h^{n+1} &= (J^{n+1} \mathbf{v}_h^{n+1}, \boldsymbol{\phi})_f, \\
\mathbf{M}^s \mathbf{v}_h^{n+1} &= (\mathbf{v}_h^{n+1}, \boldsymbol{\phi})_s, \\
\mathbf{C}_1^f(\mathbf{v}_h^{n+1}) &= (J^{n+\frac{1}{2}} \nabla \mathbf{v}_h^{n+1} (\mathbf{F}^{n+\frac{1}{2}})^{-1} \mathbf{v}_h^{n+1}, \boldsymbol{\phi})_f, \\
\mathbf{C}_2^f(\mathbf{v}_h^{n+1}) &= (\nabla \cdot (J^{n+\frac{1}{2}} \mathbf{v}_h^{n+1} (\mathbf{F}^{n+\frac{1}{2}})^{-T}) \mathbf{v}_h^{n+1}, \boldsymbol{\phi})_f, \\
\mathbf{C}_3^f(\mathbf{u}_h^{n+1}, \mathbf{v}_h^{n+1}) &= (J^{n+\frac{1}{2}} \nabla \mathbf{v}_h^{n+1} (\mathbf{F}^{n+\frac{1}{2}})^{-1} (\mathbf{u}_h^{n+1} - \mathbf{u}_h^n), \boldsymbol{\phi})_f, \\
\mathbf{C}_4^f(\mathbf{u}_h^{n+1}, \mathbf{v}_h^{n+1}) &= (J^{n+\frac{1}{2}} (\nabla \mathbf{u}_h^{n+1} - \nabla \mathbf{u}_h^n) : (\mathbf{F}^{n+\frac{1}{2}})^{-1} \mathbf{v}_h^{n+1}, \boldsymbol{\phi})_f, \\
\mathbf{S}^f(\mathbf{v}_h^{n+1}) &= \mu (J^{n+1} \nabla \mathbf{v}_h^{n+1} (\mathbf{F}^{n+1})^{-1}, \nabla \boldsymbol{\phi} (\mathbf{F}^{n+1})^{-1})_f, \\
\mathbf{S}^s(\mathbf{u}_h^{n+1}) &= (\mathbf{F}^{n+1} \boldsymbol{\Sigma}^{n+1}, \nabla \boldsymbol{\phi})_s, \\
(\mathbf{B}^f + \mathbf{B}^s)(p_h^{n+1}) &= (J^{n+1} p_h^{n+1}, \nabla \boldsymbol{\phi} (\mathbf{F}^{n+1})^{-1}), \\
\text{Rhs}_v(\mathbf{v}_h^n) &= (J^n \mathbf{v}_h^n, \boldsymbol{\phi})_f + \beta (\mathbf{v}_h^n, \boldsymbol{\phi})_s + \delta t \int_{\Gamma_{h,N}} \mathbf{h}_h^{n+1} \cdot \boldsymbol{\phi} \, d\gamma, \\
\mathbf{I}^s(\mathbf{u}_h^{n+1}) &= (J^{n+1} - 1, \psi)_s, \\
(\mathbf{B}^f)^T(\mathbf{v}_h^{n+1}) &= (\nabla \cdot (J^{n+1} \mathbf{v}_h^{n+1} (\mathbf{F}^{n+1})^{-T}), \psi)_f.
\end{aligned}$$

Aspects related to how to solve the nonlinear problem (5.1) are presented in the following section.

5.2 Nonlinear solver

Standard forms for solving the nonlinear problem (5.1) are fixed-points based iterations (see [Deparis *et al.* \[2003a\]](#); [Gerbeau & Vidrascu \[2003\]](#); [Mok *et al.* \[2001\]](#); [Nobile \[2001\]](#); [Zhang *et al.* \[2003\]](#)). Unfortunately, these methods usually show a slow rate of convergence and may fail to converge (see [Deparis *et al.* \[2003a\]](#); [Gerbeau & Vidrascu \[2003\]](#); [Matthies & Steindorf \[2002, 2003\]](#); [Mok *et al.* \[2001\]](#)). In order to speed up the convergence, it is useful to use Newton-Raphson based methods (see [Bathe & Zhang \[2004\]](#); [Gerbeau & Vidrascu \[2003\]](#); [Heil \[2004\]](#); [Hron & Turek \[2006\]](#); [Matthies & Steindorf \[2002, 2003\]](#); [Tezduyar \[2001\]](#); [Zhang *et al.* \[2003\]](#)) as the basic iteration. In the subsequent sections we describe the main features of the Newton method and its variants developed in order to reduce the cost and improve the convergence properties of the Newton method.

5.2.1 Newton's method

Consider a vector function $\mathbf{F}: \mathbb{R}^n \rightarrow \mathbb{R}^n \in C^1(D)$, i.e., \mathbf{F} is continuously differentiable function on D , where D is a convex open set of \mathbb{R}^n . We denote also by $J_{\mathbf{F}}(\mathbf{X})$ the Jacobian matrix (or tangent matrix) associated with \mathbf{F} and evaluated at the point $\mathbf{X} = (x_1, \dots, x_n)^T$ of \mathbb{R}^n , defined as

$$(J_{\mathbf{F}}(\mathbf{X}))_{ij} = \left(\frac{\partial F_i}{\partial x_j} \right) (\mathbf{X}), \quad i, j = 1, \dots, n. \quad (5.2)$$

The newton algorithm looks for a root of the vector function \mathbf{F} and can be formulated as follows

$$\begin{aligned} &\text{given } \mathbf{X}^0 \in \mathbb{R}^n, \text{ for } k = 0, 1, \dots, \text{ until convergence} \\ &\text{solve} \quad J_{\mathbf{F}}(\mathbf{X}^k) \delta \mathbf{X}^k = -\mathbf{F}(\mathbf{X}^k) \\ &\text{set} \quad \mathbf{X}^{k+1} = \mathbf{X}^k + \delta \mathbf{X}^k. \end{aligned} \quad (5.3)$$

5. SOLVERS

Thus, at each step k the solution of a linear system with matrix $J_{\mathbf{F}}(\mathbf{X})$ is required. The next paragraph will briefly describe the linear solvers available nowadays and the solver we developed to invert the Jacobian matrix in an efficient way. The following theorem asserts (for a proof see [Quarteroni *et al.* \[2010\]](#)) the local convergence properties of the Newton method.

Theorem 5.2.1. *Suppose that \mathbf{X}^* be a root of \mathbf{F} that belongs to D , that $J_{\mathbf{F}}^{-1}(\mathbf{X}^*)$ exists and that \mathbf{F} is locally Lipschitz continuous. Then, if \mathbf{X}^0 is sufficiently close to \mathbf{X}^* , the sequence (5.3) is uniquely defined and converges to \mathbf{X}^* with*

$$\|\mathbf{X}^{k+1} - \mathbf{X}^*\| \leq c \|\mathbf{X}^k - \mathbf{X}^*\|^2,$$

where c is a constant that depends on the Lipschitz constant and on the norm of $J_{\mathbf{F}}^{-1}(\mathbf{X}^*)$.

Theorem (5.2.1) shows that quadratic convergence is achieved only if the initial guess is sufficiently close to the solution and if the Jacobian matrix is nonsingular. Moreover, the explicit computation of the Jacobian matrix is often very expensive. For these reasons, several modifications to Newton's method have been proposed to reduce its cost and to improve its convergence properties, which will be briefly considered in the next section.

5.2.2 Modified Newton's methods

Several modifications to Newton's method have been proposed in order to reduce its cost when the computed solution is sufficiently close to \mathbf{X}^* .

An efficient alternative to (5.3) consists of keeping constant the Jacobian matrix for a certain number of steps. Generally, a deterioration of convergence rate is observed accompanied by a gain in computational efficiency. However, in our computation we preferred to compute the Jacobian at every step.

Another possibility is to use an iterative solver to invert the linear system (5.3), fixing a priori the maximum number of admissible iterations. The resulting schemes are called Newton-Jacobi, Newton-Krylov or Newton-Multigrid methods, according to the iterative process used for the inversion. We used a multigrid solver as iterative scheme for the solution process of (5.3).

A third possibility consists of using the *inexact* Newton method which deals with approximations of $\mathbf{J}_{\mathcal{F}}$, in contrast with *exact* Newton method, which involves repeated solutions of problem (5.3) with an exact Jacobian $\mathbf{J}_{\mathcal{F}}$ having the following block structure

$$\begin{bmatrix} \mathbf{A}_{\mathbf{u}\mathbf{u}} & \mathbf{A}_{\mathbf{u}\mathbf{v}} & 0 \\ \mathbf{A}_{\mathbf{v}\mathbf{u}} & \mathbf{A}_{\mathbf{v}\mathbf{v}} & \delta t \mathbf{B} \\ (\mathbf{B}^s)^T & (\mathbf{B}^f)^T & 0 \end{bmatrix}. \quad (5.4)$$

Using the definitions given in the first section of this chapter, the tangent matrix of the discrete FSI operator \mathcal{F} reads as follows

$$\frac{\partial \mathcal{F}}{\partial \mathbf{X}} = \begin{bmatrix} \mathbf{M}^f + \mathbf{M}^s - \delta t \mathbf{L}^f & \delta t \mathbf{M}^s & 0 \\ \frac{\partial \mathbf{M}^f}{\partial \mathbf{u}_h} + \delta t \frac{\partial(\mathbf{C}^f + \mathbf{S}^s + \mathbf{S}^f + \mathbf{B})}{\partial \mathbf{u}_h} & \mathbf{M}^s + \beta \mathbf{M}^f + \delta t \frac{\partial(\mathbf{C}^f + \mathbf{S}^f)}{\partial \mathbf{v}_h} & \delta t \mathbf{B} \\ \mathbf{I}_s + \frac{\partial(\mathbf{B}^f)^T}{\partial \mathbf{u}_h} & (\mathbf{B}^f)^T & 0 \end{bmatrix}. \quad (5.5)$$

The main difficulty in the computation of the Jacobian $\mathbf{J}_{\mathcal{F}}$ is the evaluation of the cross-derivatives in (5.5), $\frac{\partial \mathbf{M}^f}{\partial \mathbf{u}_h}$, $\frac{\partial \mathbf{C}^f}{\partial \mathbf{u}_h}$, $\frac{\partial \mathbf{S}^f}{\partial \mathbf{u}_h}$, $\frac{\partial \mathbf{B}}{\partial \mathbf{u}_h}$, $\frac{\partial(\mathbf{B}^f)^T}{\partial \mathbf{u}_h}$, corresponding to the directional derivative of the fluid operator terms with respect to fluid-domain perturbations. The evaluation of these terms requires shape derivative calculus within the fluid (see Fernández & Moubachir [2003, 2004]; Sokolowski & J.-P. [1992]). Moreover, the explicit computation of the Jacobian matrix is often very expensive.

These drawbacks can be overcome by a suitable approximation of $\mathbf{J}_{\mathcal{F}}$, for instance, using finite difference approximations of the only cross derivative terms (see Heil [2004]; Tezduyar [2001]) or of all terms (see Hron & Turek [2006]) from the residual vector $\mathcal{F}(\mathbf{X})$. However, the lack of a priori rules for selecting optimal finite difference infinitesimal steps leads to nonconsistent Jacobians (Fernández & Moubachir [2005]) and to a quite sensitivity of the resulting solution behavior w.r.t. to the finite difference infinitesimal steps. For this reason, another strategy, which is the one we adopted, may be to approximate $\mathbf{J}_{\mathcal{F}}$ by neglecting the cross derivative terms in (5.5) and evaluating the remaining terms on variational level before applying the finite element discretization (see Bathe & Zhang [2004]; Heil [2004]; Tezduyar [2001]; Zhang *et al.* [2003]). In both cases a reduction of the

5. SOLVERS

overall convergence rate is observed.

Last possibility is to use a software like Sundance that performs the Fréchet differentiation of the finite variational form under exam, i.e.(5.1), in a automatic fashion (see *Kevin et al.* [2010]).

We conclude by saying that since the sparsity pattern of the Jacobian matrix is known in advance (see Figure 5.1), which is given by the finite element method, the computation of the assembly process can be done in a efficient way so that the linear solver remains the dominant part of the solution process in terms of CPU time.

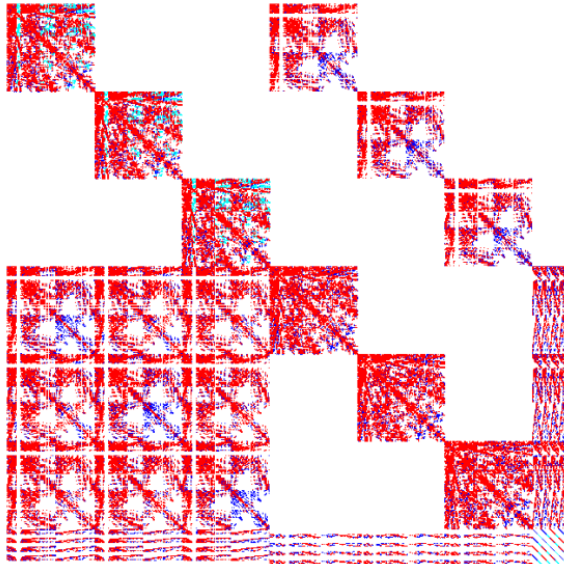


Figure 5.1: Sparsity pattern of the Jacobian matrix of the FSI operator.

5.2.3 Quasi-Newton's methods

Quasi-Newton's methods are all those schemes in which globally convergent methods are coupled with Newton-like methods that are only locally convergent, but with an order greater than one. Given a continuously differentiable function $\mathcal{F}(\mathbf{X}): \mathbb{R}^n \rightarrow \mathbb{R}^n$, which in our case coincides with the residual vector function (5.1), and an initial value $\mathbf{X}^0 \in \mathbb{R}^n$, at each step k one has to perform the following operations:

-
1. evaluate $\mathcal{F}(\mathbf{X}^k)$;
 2. choose the Jacobian $\mathbf{J}_{\mathcal{F}}(\mathbf{X}^k) = \frac{\partial \mathcal{F}}{\partial \mathbf{X}}(\mathbf{X}^k)$ as being the exact Jacobian or an approximation of it (i.e. finite difference approximation);
 3. solve the linear system $\mathbf{J}_{\mathcal{F}}(\mathbf{X}^k)\delta\mathbf{X}^k = -\mathcal{F}(\mathbf{X}^k)$;
 4. update the solution $\mathbf{X}^{k+1} = \mathbf{X}^k + \omega^k\delta\mathbf{X}^k$, where ω^k are suitable *damping parameters*.

Last step is the characterizing operation of this family of methods. Parameters ω^k can be chosen in according to a global convergence criterion, i.e, using line search techniques, which are based on the backtracking idea (see [Dennis & Schnabel \[1996\]](#); [Press *et al.* \[2002\]](#)). Line search techniques improve the chance of convergence by adaptively changing the length of the correction vector $\delta\mathbf{X}$ (see [Hron & Turek \[2006\]](#); [Turek \[1999\]](#) for more details) in order to minimize a certain error measure. One of the possible choices for the quantity to minimize is

$$\mathcal{R}(\omega) = \mathcal{F}(\mathbf{X}^n + \omega^n\delta\mathbf{X}^n) \cdot \delta\mathbf{X}^n, \quad (5.6)$$

with $\omega^k \in (0, 1]$. The algorithm starts with a full step ($\omega^k = 1$) checking if $\mathcal{R}(\omega)$ is minimized or not. If the initial guess is close to the solution then the above condition is mostly satisfied, as it happens in time-dependent simulations with a sufficient small time step. If it is not, then at least we can store this information and use it for searching a new damping factor by backtracking along the Newton direction until the function $\mathcal{R}(\omega)$ is minimized. Since we have already three parameters, $\mathcal{R}(\omega = 1)$ from the full step, $\mathcal{R}(0)$ when we evaluate the residual vector and $\mathcal{R}'(0)$ when the Jacobian matrix is built, a quadratic interpolation can be constructed. Then, the new damping factor reads

$$\omega_1 = \frac{-\mathcal{R}'(0)}{2(\mathcal{R}(1) - \mathcal{R}(0) - \mathcal{R}'(1))}. \quad (5.7)$$

By replacing $\mathcal{R}(1)$ with the last computed information $\mathcal{R}(\omega_1)$, the next damping parameter can be iteratively computed in the same way until $\mathcal{R}(\omega_k)$ meets the selected criterion. By this algorithm we can enforce a monotone convergence of

5. SOLVERS

the approximation \mathbf{X}^n (see Kelley [1999]). If $\omega^k = 1$ then the Quasi Newton method coincides with the Newton method and only one iteration is required.

Remark 5.2.1. *Theorem 5.2.1 affirms that the Newton's method is only locally convergent. The damping greatly improves the robustness of the Newton algorithm if the current approximation is not close enough to the final solution. Line search is a method which make the Newton method globally convergent.*

5.3 Linear Solvers

Consider the real algebraic system corresponding to (5.3)

$$\mathbf{Ax} = \mathbf{b}, \quad (5.8)$$

where $\mathbf{A} = J_{\mathcal{F}}(\mathbf{X}^k)$ and $\mathbf{b} = -\mathcal{F}(\mathbf{X}^k)$, and assume that \mathbf{A} is a non-singular matrix of dimension n . The solution of linear algebraic systems like (5.8) is the most time-consuming part of the numerical solution process of a PDE problem, therefore it is not surprising if a lot of effort has been made in order to develop efficient linear solvers.

Linear algebraic system solvers are generally divided into two broad categories, the *direct solvers* and the *iterative solvers*. Direct methods give the exact solution to (5.8) in a finite number of steps (in the absence of round-off errors). The most classical direct method is the *Gaussian Elimination method* (GEM), which consists of decomposing the matrix \mathbf{A} into the product \mathbf{LU} , where \mathbf{L} and \mathbf{U} are, respectively, a lower triangular and an upper triangular matrix. Direct linear solvers are preferably used when the matrix \mathbf{A} is dense or when the matrix \mathbf{A} is sparse and the size of the problem n is small (i.e. number of unknowns less than 20.000). However, for larger sparse system they become less efficient with respect to iterative methods and their memory and CPU time requirements could become prohibitive. Implementations of sparse direct linear solver can be found in the UMFPACK (Davis & Duff [1999]), MUMPS (Amestoy *et al.* [2000]) and SUPERLU (Li [2005]) packages. UMFPACK is a set of routines for solving unsymmetric sparse linear system using the Unsymmetric MultiFrontal method, MUMPS is a MULTifrontal Massively Parallel distributed symmetric and unsym-

metric Solver and SUPERLU is a library for for the direct solution of large, sparse, nonsymmetric systems of linear equations on high performance machines.

Contrarily iterative methods provide the solution to (5.8) as the limit of a sequence \mathbf{x}^k and usually the matrix \mathbf{A} is only involved in matrix-vector multiplications. Typical situations in which iterative methods are involved are large sparse problems that can arise from the Finite-Element Galerkin discretization of a PDE. Iterative solvers can be further divided into two broad classes, namely Krylov Subspace solvers and Multigrid solvers. In the following subsections a general description of these methods is reported.

5.3.1 Krylov Subspace Solver

The Krylov subspace methods are considered currently among the most important iterative techniques for solving large linear systems. These techniques are based on projection algorithms, both orthogonal and incline, onto *Krylov subspaces* K_m of order m associated with matrix \mathbf{A} and vector \mathbf{v} , which are defined as

$$K_m(\mathbf{A}; \mathbf{v}) = \text{span} \{ \mathbf{v}, \mathbf{A}\mathbf{v}, \dots, \mathbf{A}^{m-1}\mathbf{v} \}. \quad (5.9)$$

In other words, it is a subspace of the set spanned by all the vectors $\mathbf{u} \in \mathbb{R}^n$ that can be written as $\mathbf{u} = p_{m-1}(\mathbf{A})\mathbf{v}$, where p_{m-1} is a polynomial in \mathbf{A} of degree $\leq m - 1$. A general projection algorithm for solving the linear system (5.8) is a method which seeks an approximate solution \mathbf{x}_m belongs to the affine subspace

$$W_m = \{ \mathbf{v} = \mathbf{x}_0 + \mathbf{y}, \quad \mathbf{y} \in K_m(\mathbf{A}; \mathbf{r}_0) \}, \quad (5.10)$$

where $\mathbf{r}_0 = \mathbf{b} - \mathbf{A}\mathbf{x}_0$ is the initial residual and \mathbf{x}_0 an arbitrary initial guess to the solution, under the condition

$$\mathbf{b} - \mathbf{A}\mathbf{x}_m \perp L_m, \quad (5.11)$$

where L_m is another Krylov subspace of dimension m . The different versions of Krylov subspace methods are related to the definition of the subspace L_m and from the way in which the system is preconditioned (Saad [2000]). From the

5. SOLVERS

approximation theory point of view, the approximation obtained by a Krylov subspace method can be written in the following form

$$\mathbf{A}^{-1}\mathbf{v} \approx \mathbf{x}_m = \mathbf{x}_0 + p_{m-1}(\mathbf{A})\mathbf{r}_0. \quad (5.12)$$

Although all the techniques provide the same type of *polynomial* approximations, the choice of L_m , i.e., the constraint used for the computation of the coefficients of the polynomial p_{m-1} , has an important effect on the behavior of the iterative technique. Two broad choices for L_m give rise to the best known techniques.

The first class is obtained simply imposing $L_m = K_m$ or $L_m = \mathbf{A}K_m$, giving rise to an orthogonal or oblique projection method, respectively. The Arnoldi method (more commonly known as FOM, *full orthogonalization method*) and the GMRES (*generalized minimum residual*) method fall in this category. In the Arnoldi method the approximation \mathbf{x}_m is computed enforcing that the residual $\mathbf{r}_m = \mathbf{b} - \mathbf{A}\mathbf{x}_m$ is orthogonal to any vector in $K_m(\mathbf{A}; \mathbf{r}_0)$, i.e., we look for a vector $\mathbf{x}_m \in W_m$ such that

$$\mathbf{v}^T(\mathbf{b} - \mathbf{A}\mathbf{x}_m) = 0, \quad \forall \mathbf{v} \in K_m(\mathbf{A}; \mathbf{r}_0). \quad (5.13)$$

In the GMRES method, instead, we seek for an approximation $\mathbf{x}_m \in W_m$ that minimizes the Euclidean norm of the residual $\|\mathbf{r}_m\|_2$, i.e.,

$$\|\mathbf{b} - \mathbf{A}\mathbf{x}_m\|_2 = \min_{\mathbf{v} \in W_m} \|\mathbf{b} - \mathbf{A}\mathbf{v}\|_2. \quad (5.14)$$

Both FOM and GMRES require to compute an orthonormal basis for the Krylov subspace $K_m(\mathbf{A}; \mathbf{r}_0)$ for building the approximation \mathbf{x}_m . The orthogonalization algorithm, named *Arnoldi algorithm* and based on the *Gram-Schmidt* procedure, entails a high computational effort and a large amount of memory if the dimension of the space m is high. This happens if the iterative method does not converge in a few iterations. For this reason, two variants of the algorithm are available, one named GMRES(m) and based on the restart after m steps, with \mathbf{x}_m as initial guess, the other named Quasi-GMRES based on stopping the Arnoldi orthogonalization algorithm ([Quarteroni \[2009\]](#)).

The second class of methods is based on defining L_m to be a Krylov subspace

method associated with \mathbf{A}^T , namely, $L_m = K_m(\mathbf{A}^T, \mathbf{r}_0)$. The conjugate bigradient method BiCG, as well as its stabilised version, the BiCGSTAB method belong to this class.

5.3.1.1 Preconditioning techniques

It is well observed that iterative solvers require less memory compared to direct solvers but for ill-conditioned problems they may suffer from lack of robustness and stability issues without preconditioning techniques. The idea of preconditioning is simply to transforming the original linear system into one which is equivalent, but which is likely to be easier to solve with an iterative solver. Consider the following equivalent system

$$\mathbf{P}^{-1}\mathbf{A}\mathbf{x} = \mathbf{P}^{-1}\mathbf{b}, \quad (5.15)$$

obtained multiplying the left and right end side of system (5.8) by a non singular matrix \mathbf{P}^{-1} , named preconditioner. The basic requirements in order for \mathbf{P} to be a good preconditioner of \mathbf{A} are that \mathbf{P} is “easy” to invert and that the condition number of $\mathbf{P}^{-1}\mathbf{A}$ is smaller than the condition number of \mathbf{A} . \mathbf{P} is said to be an *optimal* preconditioner if the condition number of the product $\mathbf{P}^{-1}\mathbf{A}$ is bounded uniformly with respect to the order of \mathbf{A} (Quarteroni & Valli [1994]). A preconditioner can also be defined as a supplementary linear system associated to \mathbf{P} which is easy to be solved and combined with an outer iteration technique, typically one of the Krylov subspace iterations. In general, the reliability of iterative techniques depends much more on the quality of preconditioner than the particular outer iteration technique.

The simplest preconditioner is provided by the diagonal matrix of \mathbf{A}

$$\mathbf{P} := \mathbf{D} = \text{diag}(a_{11}, \dots, a_{nn}), \quad (5.16)$$

i.e., the Jacobi preconditioner. The resulting matrix $\mathbf{P}^{-1}\mathbf{A}$ is obtained by scaling each row by the reciprocal of the diagonal entry of the matrix \mathbf{A} and can be solved by a Krylov subspace method. In order for this preconditioned iteration method to be an effective procedure is that \mathbf{A} is diagonally dominant.

5. SOLVERS

For a non symmetric sparse matrix \mathbf{A} , especially when \mathbf{A} is banded, one of the most successful preconditioning techniques is to perform an *incomplete LU* (*ILU*) factorization of the original matrix. A general incomplete LU factorization process computes a sparse lower triangular matrix \mathbf{L} and a sparse upper triangular matrix \mathbf{U} so that the residual matrix $\mathbf{R} = \mathbf{LU} - \mathbf{A}$ satisfies certain constraints. The incomplete factorization $ILU(0)$ with no fill-in is defined uniquely by taking the matrices \mathbf{L} and \mathbf{U} with the same nonzero structure as the lower and upper parts of \mathbf{A} , respectively, and by taking the zero pattern of \mathbf{R} to be precisely the zero pattern of \mathbf{A} (see Saad [2000]).

This incomplete factorization is rather easy and inexpensive to compute, but it often leads to a crude approximation which may result in a slow convergence of the outer Krylov subspace algorithm. To improve the rate of convergence, several alternative incomplete factorizations have been developed by allowing more fill-in in \mathbf{L} and \mathbf{U} , leading to the $ILU(p)$ method and its improvements, the modified ILU ($MILU$) and the $ILUT$ algorithms (see van der Vorst [2003], Saad [2000], van der Vorst [1989], Evans [1983]).

In general, the more accurate ILU factorizations are, fewer iterations are required by the iterative method to converge, but the preprocessing cost to perform the factorization is higher. However, these trade-offs generally favor the more accurate factorization due to improved robustness of the iterative procedure. This is especially true when several problems with the same matrix needs to be solved because the cost of this operation can be amortized.

5.3.2 Multigrid Solver

The multigrid method provide an efficient iterative algorithm for solving elliptic boundary value problems, however it can be applied on a wider class of problems. Today it is considered one of the fastest iterative linear solvers for large CFD problems. In contrast to other iterative methods, the total amount of computational work involved is proportional to the number of unknowns in the discretized equations.

In this thesis we have applied successfully the Multilevel Domain Decomposition technique to monolithic FSI problems. This technique was initially pro-

posed by [Aulisa *et al.* \[2006\]](#) and applied to CFD problems, FSI and FSTI partitioned problems, see [Aulisa *et al.* \[2008, 2009\]](#). Multilevel-Domain Decomposition methodology combines together the major features of Domain Decomposition (DD), Selective Mesh Refinement (SMR) and Algebraic Multigrid algorithms (AMG) and it allows the user to select the regions of mesh refinement in order to reduce the degrees of freedom to be solved without losing the multigrid algorithm features. This feature is very attractive in several physical fields, such as FSI, CFD or two-phase flow, where it is of interest to have an algorithm that is able to handle finer mesh near interfaces or in boundary layers where the solution has strong variations.

In this section we describe in a quite abstract and simplistic way the Multilevel-Domain Decomposition methodology in order to introduce the non-familiar reader to the major ideas that are behind Multigrid, Domain Decomposition and Vanka-type smoothers, and to show how we combine these methods to solve Fluid-Structure Interaction problems.

5.3.2.1 Multilevel Domain Decomposition

Domain decomposition methods allow for effective implementation of numerical techniques for partial differential equations on parallel architectures. The parallelization of the algorithm has been accomplished using the Petsc library. The multilevel domain decomposition algorithm is based on the assumption that the given computational domain, say Ω , is partitioned into several non-overlapping subdomains Ω_i , $i = 1, \dots, M$, and for each of them we introduce a finite element discretization. Next, the original problem can be reformulated upon each subdomain Ω_i yielding a family of subproblems of reduced size which are coupled each others through the values of the unknown solution at subdomain interfaces. Although we do not require mesh conformity at the interface between adjacent subdomains, we enforce continuity for each state variable on the common boundaries. This is achieved in a natural and straightforward way by using the ideas that are behind multigrid algorithms.

In [Figure 5.2](#) an example of non-conforming mesh partitioning is generated for a square domain Ω , where on the right-bottom part of the domain there is a

5. SOLVERS

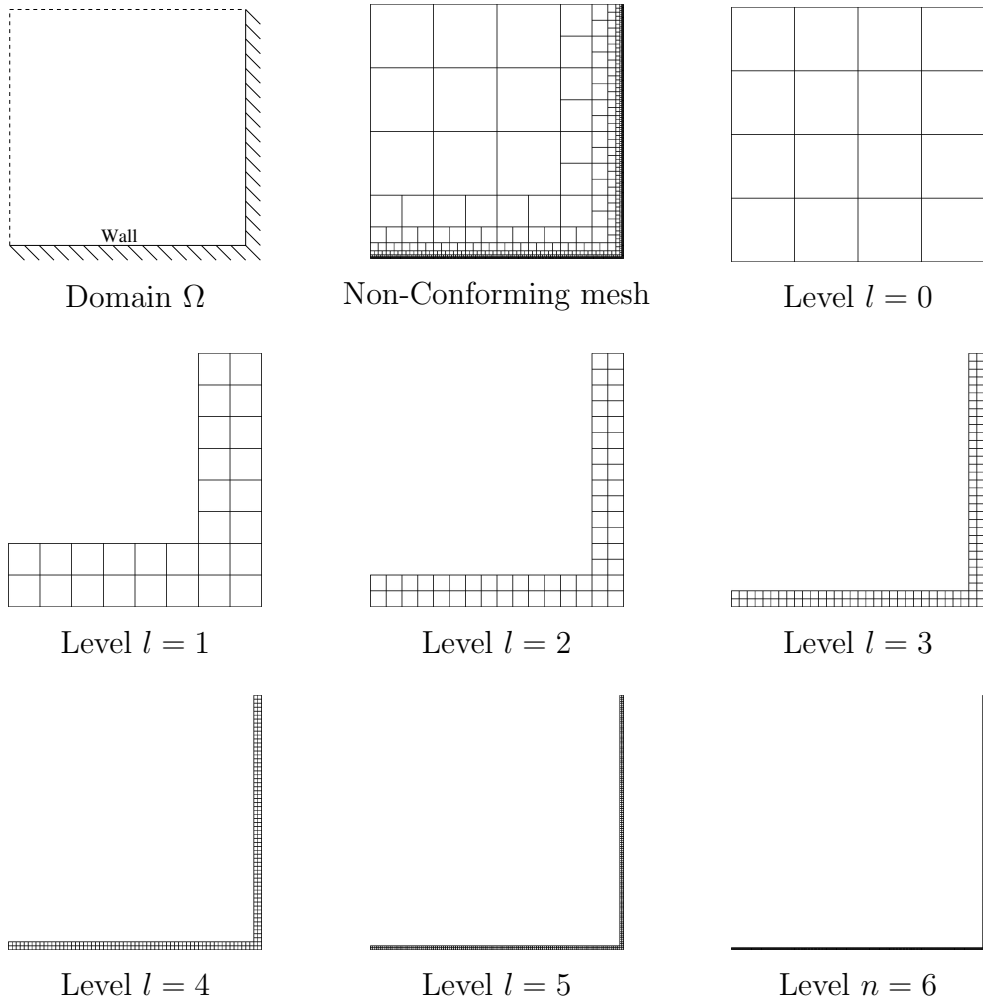


Figure 5.2: Example of a non conforming mesh built using multilevel triangulations.

wall. In the region closed to the wall a progressive mesh refinement is constructed as it follows. By starting at the coarse level $l = 0$, we discretize the entire domain Ω into quadrilaterals (in more generality quadrilaterals and triangles (in 2D), or hexahedra, wedges and tetrahedra (in 3D)). A conforming coarse mesh \mathcal{T}_h^0 is then generated throughout the entire domain Ω . Based on a simple element midpoint refinement, successive level meshes \mathcal{T}_h^l are built recursively up to the top level $l = n$, until the geometry and/or the physics of the considered problem is well represented. Each level mesh \mathcal{T}_h^l is not defined on the whole domain Ω ,

but only on a subregion Ω^l where refinement is needed. Every triangulation \mathcal{T}_h^l is conforming within its own domain Ω^l . In the example of Figure 5.2 the refined subdomains Ω^l are thinner regions closer to the wall. If we consider the non-conforming mesh given by the union of all the triangulations \mathcal{T}_h^l , the nodes of the coarser mesh are always included in the nodes of the finer mesh on adjacent boundaries. This is the key point for this kind of discretization and it is always true for different level meshes generated by using midpoint refinements.

Let $V^{l,\Omega^l} \subset H_0^1(\Omega^l)$ be the finite-dimensional space built on the triangulation \mathcal{T}_h^l , and let V^l be its continuous extension by zero on the whole domain Ω . Notice that each element $u^l \in V^l$ is continuous, since by definition each element of V^{l,Ω^l} has zero trace on its boundary. The non-conforming space V_l is defined to be

$$V_l = \bigcup_{k=0}^l V^k. \quad (5.17)$$

Clearly, this space is defined on the non-conforming triangulation

$$\mathbb{T}_{h,l} = \bigcup_{k=0}^l \mathcal{T}_h^k. \quad (5.18)$$

Notice that

$$V_0 \subset V_1 \subset \dots \subset V_n, \quad (5.19)$$

but in general $V^{l-1} \not\subset V^l$. Any element u_l of V_l can be represented as

$$u_l = \sum_{k=0}^l u^k, \quad (5.20)$$

for some $u^l \in V^l$, thus it is continuous. Of particular interest is the space

$$V_h := V_n, \quad (5.21)$$

where we seek the solution u_h .

Summarizing, for each level we introduced two families of spaces:

1. V^l , built over a conforming triangulation on Ω^l , with extension by zero in

5. SOLVERS

$$\Omega \setminus \Omega_l;$$

2. V_l , built over a non-conforming triangulation up to the level l .

We define the index n_{MG} to be the highest level index l for which $V_l = V^l$. Note that $n_{MG} \geq 0$ since on the coarsest level ($l = 0$) we built a conforming triangulation all over the domain Ω . Moreover if $n = n_{MG}$ then at each level we have a conforming triangulation, and the standard multigrid spaces are recovered.

We can now define the inter-space transfer operators as it follows. The coarse-to-fine operator

$$I_{l-1}^l : V_{l-1} \rightarrow V_l \quad (5.22)$$

is taken to be the natural injection. In other words

$$I_{l-1}^l u_{l-1} = u_{l-1}, \quad \forall u_{l-1} \in V_{l-1}. \quad (5.23)$$

The fine-to-coarse inter-space transfer operator

$$I_l^{l-1} : V_l \rightarrow V_{l-1} \quad (5.24)$$

is defined to be the transpose of I_{l-1}^l , with respect to the inner product (\cdot, \cdot) . In other words

$$(I_l^{l-1} w_l, u_{l-1}) = (w_l, I_{l-1}^l u_{l-1}) \quad \forall u_{l-1} \in V_{l-1}, w_l \in V_l. \quad (5.25)$$

Note that although the inter-space operators are defined similarly to the intergrid operators used in the multigrid method ([Brenner & ScottBrown \[2008\]](#)), they differ because of the non-conforming space representations.

The Multilevel Domain Decomposition algorithm works similarly to an algebraic multigrid algorithm ([Brenner & ScottBrown \[2008\]](#)) with the exception that the spaces for the state variables, the residuals, the error correction and the corresponding test functions should be taken following different rules. Furthermore the inter-level operators (fine-to-coarse (prolongation) and coarse-to-fine (restriction)) are non-standard since they are defined between two consecutive non-conforming spaces. In [Figure 5.3](#) we reported the weights for the prolongation operator in the \mathbb{Q}_2 finite element space.

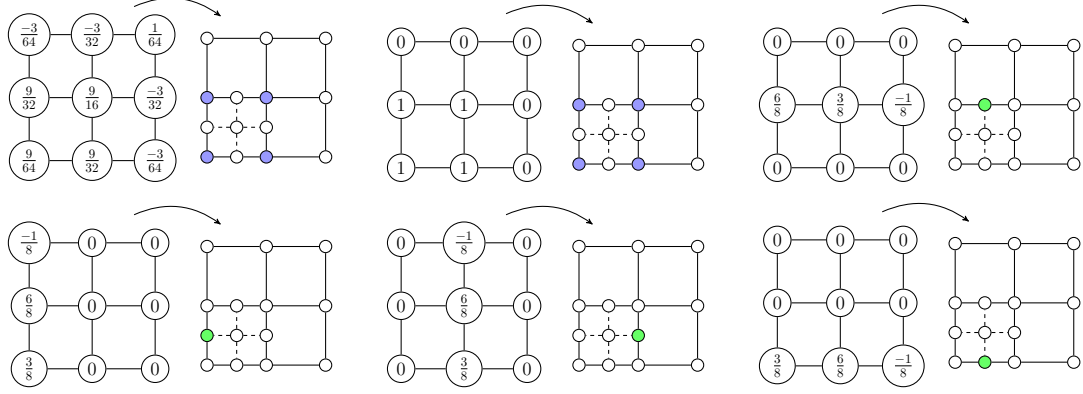


Figure 5.3: Weights for the prolongation operator in \mathbb{Q}_2 with biquadratic interpolation.

Below we present a schematic description for solving the problem

$$a(u_h, v_h) = (f, v_h) \quad \forall v_h \in V_h, \quad (5.26)$$

where $a(\cdot, \cdot)$ is a differential operator, f is an external force/source term and they both depend on the physics of particular problem that is been considered. First we describe the l^{th} level iteration, and then the full algorithm (see Figure 5.4).

The l^{th} Level Iteration. $ML(l, z_0, g)$ is the approximate solution of

$$a(z, v_l) = (g, v_l) \quad \forall v_l \in V_l, \quad (5.27)$$

obtained at the l^{th} level with initial guess $z_0 \in V_l$.

For $l = 0$, $ML(l, z_0, g)$ is the solution of the problem

$$a(ML(l, z_0, g), v_0) = (g, v_0) \quad \forall v_0 \in V_0, \quad (5.28)$$

obtained with a direct method. Note that $V_0 = V^0$ is a conforming space all over the domain Ω .

For $l > 0$, $ML(l, z_0, g)$ is obtained recursively in 3 steps.

1. *Pre-smoothing Step.* For $1 \leq j \leq m_1$, let

$$z_j = z_{j-1} + (S^l)^{-1} r^j, \quad (5.29)$$

5. SOLVERS

where $r^j \in V^l$ satisfies

$$(r^j, v^l) = (g, v^l) - a(z_{j-1}, v^l) \quad \forall v^l \in V^l, \quad (5.30)$$

and $S^l : V^l \rightarrow V^l$ is some invertible *smoothing operator* that will be defined later and it depends on the specific equation system. Since V^l is built as a continuous extension by zero of V^{l, Ω^l} to the whole domain Ω , then without loosing generality the equivalent operator $S^{l, \Omega^l} : V^{l, \Omega^l} \rightarrow V^{l, \Omega^l}$ can also be considered.

2. *Error Correction Step.* Let $q_0 = 0$ and $\bar{g} := I_l^{l-1} r_l$, where $r_l \in V_l$ satisfies

$$(r_l, v_l) = (g, v_l) - a(z_{m_1}, v_l) \quad \forall v_l \in V_l. \quad (5.31)$$

Let

$$q_1 = ML(l-1, q_0, \bar{g}). \quad (5.32)$$

Then

$$z_{m_1+1} = z_{m_1} + I_{l-1}^l q_1. \quad (5.33)$$

3. *Post-smoothing Step.* For $m_1 + 2 \leq j \leq m_1 + m_2 + 1$, let

$$z_j = z_{j-1} + (S^l)^{-1} r_j. \quad (5.34)$$

Then the output of the l^{th} level iteration is

$$ML(l, z_0, g) := z_{m_1+m_2+1}. \quad (5.35)$$

Here m_1 and m_2 are positive integers.

The Full Multilevel Algorithm. The solution $u_h \in V_h$ of the problem

$$a(u_h, v_h) = (f, v_h) \quad \forall v_h \in V_h \quad (5.36)$$

is obtained with the following nested iterations.

For $l = 0$, $u_0 \in V_0$ is the solution of

$$a(u_0, v_0) = (f, v_0) \quad \forall v_0 \in V_0, \quad (5.37)$$

obtained with a direct method.

For $1 \leq l \leq n$, the approximate solutions $u_l \in V_l$ are obtained recursively from

$$u_{l,0} = I_{l-1}^l u_{l-1}, \quad (5.38)$$

$$u_{l,j} = ML(l, u_{l,j-1}, f) \quad 1 \leq j \leq r, \quad (5.39)$$

$$u_l = u_{l,r}. \quad (5.40)$$

Finally

$$u_h = u_n. \quad (5.41)$$

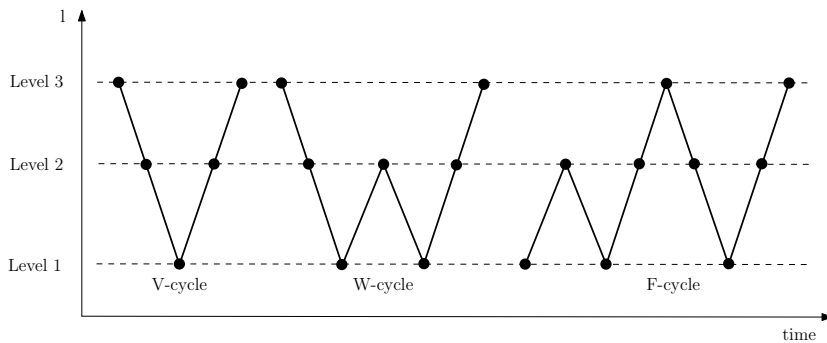


Figure 5.4: Multigrid V, W and F cycles.

5.3.2.2 Vanka-type smoothers

The Vanka-type class of smoothers has been originally introduced by Vanka (Vanka [1985]) for solving the Navier-Stokes equations discretized by finite differences. This type of multigrid smoothers can be considered as a block Gauss-Seidel method, where each block consists of a small number of degrees of freedom (for details see Vanka [1985, 1986]).

The Vanka technique has especially been developed to deal with saddle point systems having a matrix with a zero block appearing on the diagonal, where standard point-wise Jacobi or Gauss-Seidel smoothers fail. Due to the incom-

5. SOLVERS

compressibility constraint, Stokes, linearized Navier-Stokes and incompressible FSI belong to this class of problems and this is one of the main reasons why the method has influenced the field of computational fluid dynamics (CFD). Other reasons are that it can be implemented in a finite element library using elementary techniques available in solver packages like PETSC and it is efficient and robust for a wide class of problem configurations.

While the theoretical aspects of the Vanka smoother has not been deeply investigated (see [Manservigi \[2006\]](#); [Molenaar \[1991\]](#); [Scheberl & Zulehner \[2003\]](#)), many articles can be found in literature presenting numerical studies of different Vanka-type smoothers for solving the discretized Navier-Stokes equations in CFD. John and Tobiska apply it to the non-conforming Crouzeix/Raviart element \mathbb{P}_1 - \mathbb{P}_0 , Turek to the corresponding non-conforming rotated bilinear Rannacher/Turek element \mathbb{Q}_1 - \mathbb{P}_0 and Becker to the stabilized \mathbb{Q}_1 - \mathbb{Q}_1 element (see [Wobker & Turek \[2009\]](#) and the references therein). In all cases, the smoother has been extensively tested on the benchmark configuration “Flow around a cylinder” ([Turek \[1999\]](#); [Turek & Schäfer \[1996\]](#)), both for the steady and unsteady case. Less examples can be found in the contest of Fluid-Structure Interaction or Computational Solid Mechanics. For further references, the interested reader can consult the overview paper of [Wesseling & Oosterlee \[2001\]](#) and comparative solver studies including Vanka smoothers ([Turek \[1999\]](#)).

The characteristic feature of these types of smoothers is that all field variables (i.e. displacement, velocity and pressure in the FSI case) are directly coupled on a local level resulting in a large number of small coupled linear systems that have to be solved successively in each smoothing step. Each system corresponds to all the degrees of freedom of all field variables associated with a block of elements in a compact subdomain. The blocks are overlapping and their union spans the whole domain. The Vanka-smoother can be regarded as an overlapping *domain decomposition* method, where each sub-system can be solved using the most appropriate solver

For conforming finite elements the Fluid-Structure Interaction block may consist of all the elements containing some pressure dofs. Thus, in the case of Q_2P_1 discretization of fluid structure interaction problems, which has been employed in this thesis, a smoothing step with a Vanka smoother consists of a loop over all the

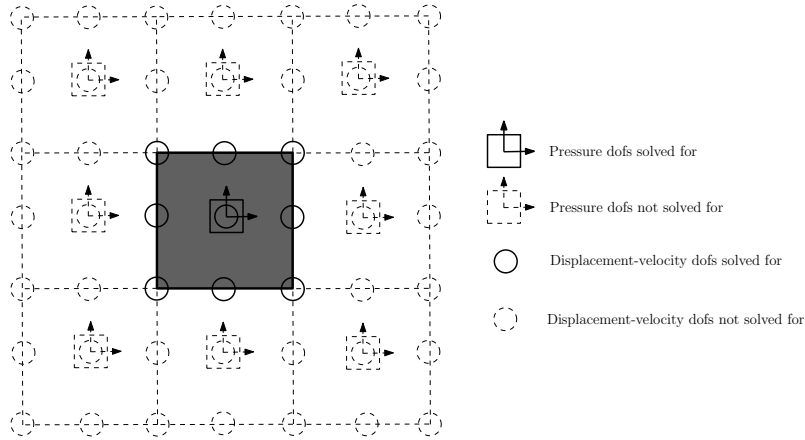


Figure 5.5: Vanka-block for the FSI $Q_2Q_2P_1$ Crouzeix-Raviart finite element.

blocks, solving only the equations involving the degrees of freedom (dofs) related to the elements that contain element pressure dofs. The displacement, velocity and pressure dofs are solved many times in one smoothing step. Examples of computations with this kind of smoother and finite element discretization can be found in [Hron & Turek \[2006\]](#) and [Razzaq \[2011\]](#).

Figure 5.5 shows an example of a minimal Vanka-block for a 2D structured $Q_2Q_2P_1$ Crouzeix-Raviart finite element triangulation (discontinuous linear pressure and bi-quadratic displacement and velocity). We use the same strategy for non-structured 2D and 3D triangulations.

1. The internal elements are marked: one in this example, the darker element located in the middle.
2. A search for all the pressure dofs associated with the internal elements is done: the 3 dofs (the square and the two arrows) associated to the middle element.
3. A search for all the velocity dofs associated to the internal elements is done: the 9 solid circle.
4. The small local matrix associated with all the found dofs ($3 + 9 \times 4 = 39$) is extracted from the global matrix and its inverse is obtained using hardware optimized direct solvers.

5. SOLVERS

Note that the equation system associated with the dofs to be solved, involves a number of pressure, displacement and velocity dofs that are not solved for (the 40×2 dashed circles for the velocity and displacement and the 8×3 dashed squares for the pressure). Their contribution to the equation system is taken into account in the assembly process of the current local residual as an explicit term calculated with the last updated values.

Remark 5.3.1. *Since the Crouzeix-Raviart finite element has a discontinuous pressure with an element-wise compact support, a less number of pressure dofs has to be updated with respect to finite element with continuous pressure (i.e. \mathbb{Q}_2 - \mathbb{Q}_1 Taylor-Hood finite element). In particular, pressure dofs that are not solved for are 8×3 in two-dimension. Besides, this advantage is enhanced in parallel computations together with Multilevel domain decomposition techniques where a non-conformal mesh is adopted.*

The number of internal elements used in each Vanka-block is a parameter that we fix a-priori. The larger this number is, the bigger the domain for each Vanka-block is, the smaller the number of Vanka-blocks needed to span the whole domain is, the better the algorithm convergence properties are. However, the number of dofs increases linearly with the Vanka-block size, thus the computational time increases with a cubic factor, if a direct solver is used. We have found that a good compromise between these opposite factors is obtained with a number of 64 internal elements in two-dimensional computations.

We used on finer levels a fixed number of Vanka smoothing iterations in the presmoothing and postsmoothing step which operate locally in each block $\Omega_i^l \subset \Omega^l$. Such iterations define the $S^{l,\Omega^l} : V^{l,\Omega^l} \rightarrow V^{l,\Omega^l}$ operator previously declared and can be written as

$$\begin{bmatrix} \mathbf{u}^{l+1} \\ \mathbf{v}^{l+1} \\ p^{l+1} \end{bmatrix} = \begin{bmatrix} \mathbf{u}^l \\ \mathbf{v}^l \\ p^l \end{bmatrix} - \omega^n \sum_{\Omega_i^l} \begin{bmatrix} \mathbf{A}_{\mathbf{uu}}|_{\Omega_i^l} & \mathbf{A}_{\mathbf{uv}}|_{\Omega_i^l} & \mathbf{0} \\ \mathbf{A}_{\mathbf{vu}}|_{\Omega_i^l} & \mathbf{A}_{\mathbf{vv}}|_{\Omega_i^l} & dt * (\mathbf{B}_{f|\Omega_i^l} + \mathbf{B}_{s|\Omega_i^l}) \\ \mathbf{B}_{s|\Omega_i^l}^T & \mathbf{B}_{f|\Omega_i^l}^T & \mathbf{0} \end{bmatrix}^{-1} \begin{bmatrix} \mathbf{res}_u^l \\ \mathbf{res}_v^l \\ \mathbf{res}_p^l \end{bmatrix}, \quad (5.42)$$

where the residual vector is computed in the following way

$$\begin{bmatrix} \text{res}_u^l \\ \text{res}_v^l \\ \text{res}_p^l \end{bmatrix} = \left(\begin{bmatrix} \mathbf{A}_{uu} & \mathbf{A}_{uv} & \mathbf{0} \\ \mathbf{A}_{vu} & \mathbf{A}_{vv} & dt * (\mathbf{B}_f + \mathbf{B}_s) \\ \mathbf{B}_s^T & \mathbf{B}_f^T & \mathbf{0} \end{bmatrix} \begin{bmatrix} \mathbf{u}^l \\ \mathbf{v}^l \\ p^l \end{bmatrix} - \begin{bmatrix} \mathbf{b}^u \\ \mathbf{b}^v \\ \mathbf{b}^p \end{bmatrix} \right)_{\Omega_i^l} \quad (5.43)$$

and ω^n is a relaxation parameter. Vanka-block equation systems can be solved using a direct solver or an iterative solver. As iterative solver we have used the GMRES with ILU preconditioner. The results are similar in terms of computational time if the dimension of the linear systems to be solved are relatively small. In addition, we noticed that multigrid algorithms which use direct solvers in the Vanka smoothing process seem to be more robust with respect to the one which use iterative solvers if the error tolerance is set too small. However, since the cost of solving a linear system using a direct solver is approximately $\frac{2}{3}n^3$ floating point operations, where n is the size of the matrix to invert, the performance of using direct solvers in the Vanka smoothing process decreases rapidly.

In alternative we can see the small local matrix as a block matrix which offers the possibility of far more efficient solvers than just treating the entire matrix as a black box. In our case the blocks arise naturally from the underlying physics. We can decouple the entire local matrix in four blocks as follows

$$\begin{bmatrix} \mathbf{A}_{00} & \mathbf{A}_{01} \\ \mathbf{A}_{10} & \mathbf{A}_{11} \end{bmatrix}, \quad (5.44)$$

where each single block is defined as

$$\begin{aligned} \mathbf{A}_{00} &= \begin{bmatrix} \mathbf{A}_{uu|\Omega_i^l} & \mathbf{A}_{uv|\Omega_i^l} \\ \mathbf{A}_{vu|\Omega_i^l} & \mathbf{A}_{vv|\Omega_i^l} \end{bmatrix} & \mathbf{A}_{01} &= \begin{bmatrix} \mathbf{0} \\ dt * (\mathbf{B}_{f|\Omega_i^l} + \mathbf{B}_{s|\Omega_i^l}) \end{bmatrix} \\ \mathbf{A}_{10} &= \begin{bmatrix} \mathbf{B}_{s|\Omega_i^l}^T & \mathbf{B}_{f|\Omega_i^l}^T \end{bmatrix} & \mathbf{A}_{11} &= \begin{bmatrix} \mathbf{0} \end{bmatrix}, \end{aligned}$$

which corresponds to a splitting the displacement and velocity from the pressure. For two by two blocks there is a family of solvers based on Schur complements.

5. SOLVERS

The inverse of the Schur complement factorization is

$$\begin{aligned}
& \left(\begin{bmatrix} \mathbf{I} & \mathbf{0} \\ \mathbf{A}_{10}\mathbf{A}_{00}^{-1} & \mathbf{I} \end{bmatrix} \begin{bmatrix} \mathbf{A}_{00} & \mathbf{0} \\ \mathbf{0} & \mathbf{S} \end{bmatrix} \begin{bmatrix} \mathbf{I} & \mathbf{A}_{00}^{-1}\mathbf{A}_{01} \\ \mathbf{0} & \mathbf{I} \end{bmatrix} \right)^{-1} = \\
& \begin{bmatrix} \mathbf{I} & \mathbf{A}_{00}^{-1}\mathbf{A}_{01} \\ \mathbf{0} & \mathbf{I} \end{bmatrix}^{-1} \begin{bmatrix} \mathbf{A}_{00}^{-1} & \mathbf{0} \\ \mathbf{0} & \mathbf{S}^{-1} \end{bmatrix} \begin{bmatrix} \mathbf{I} & \mathbf{0} \\ \mathbf{A}_{10}\mathbf{A}_{00}^{-1} & \mathbf{I} \end{bmatrix}^{-1} = \\
& \begin{bmatrix} \mathbf{I} & -\mathbf{A}_{00}^{-1}\mathbf{A}_{01} \\ \mathbf{0} & \mathbf{I} \end{bmatrix} \begin{bmatrix} \mathbf{A}_{00}^{-1} & \mathbf{0} \\ \mathbf{0} & \mathbf{S}^{-1} \end{bmatrix} \begin{bmatrix} \mathbf{I} & \mathbf{0} \\ -\mathbf{A}_{10}\mathbf{A}_{00}^{-1} & \mathbf{I} \end{bmatrix} = \\
& \begin{bmatrix} \mathbf{A}_{00}^{-1} & \mathbf{0} \\ \mathbf{0} & \mathbf{I} \end{bmatrix} \begin{bmatrix} \mathbf{I} & -\mathbf{A}_{01} \\ \mathbf{0} & \mathbf{I} \end{bmatrix} \begin{bmatrix} \mathbf{I} & \mathbf{0} \\ \mathbf{0} & \mathbf{S}^{-1} \end{bmatrix} \begin{bmatrix} \mathbf{I} & \mathbf{0} \\ -\mathbf{A}_{10}\mathbf{A}_{00}^{-1} & \mathbf{I} \end{bmatrix},
\end{aligned}$$

where $\mathbf{S} = \mathbf{A}_{11} - \mathbf{A}_{10}\mathbf{A}_{00}^{-1}\mathbf{A}_{01}$ is the Schur complement. The Schur complement of a matrix (dense or sparse) is essentially always dense and very expensive to be computed. Therefore, an approximation of \mathbf{S} , namely, $\hat{\mathbf{S}} = \mathbf{A}_{11} - \mathbf{A}_{10}[\text{ILU}(0)(\mathbf{A})]^{-1}\mathbf{A}_{01}$, is implemented in the Petsc library (see [Balay *et al.* \[2013\]](#) for further details). The Schur complement algorithm for solving the Vanka-block equation systems (5.42) reads as follows

$$\text{given } \mathbf{z}^l = \begin{bmatrix} \mathbf{u}^l \\ \mathbf{v}^l \end{bmatrix}, p^l, \mathbf{res}_z^l = \begin{bmatrix} \mathbf{res}_u^l \\ \mathbf{res}_v^l \end{bmatrix} \text{ and } res_p^l,$$

$$\text{solve } \mathbf{A}_{00}\delta\mathbf{z}^l = \mathbf{res}_z^l \quad (5.45)$$

$$\text{solve } \hat{\mathbf{S}}\delta p^l = res_p^l - \mathbf{A}_{10}\mathbf{A}_{00}^{-1}\mathbf{res}_z^l \quad (5.46)$$

$$\text{solve } \mathbf{A}_{00}\delta\mathbf{z}^l = \mathbf{res}_z^l - \mathbf{A}_{01}\delta p^l \quad (5.47)$$

$$\text{update } \begin{bmatrix} \mathbf{z}^{l+1} \\ p^{l+1} \end{bmatrix} = \begin{bmatrix} \mathbf{z}^l \\ p^l \end{bmatrix} - \omega^l \begin{bmatrix} \delta\mathbf{z}^l \\ \delta p^l \end{bmatrix}. \quad (5.48)$$

The Schur complement matrix is known only implicitly. Therefore, iterative schemes that require only matrix-vector products seems to be appropriate solvers of (5.46). In this way it is not necessary to assemble the Schur complement $\hat{\mathbf{S}}$ in order to solve the system with it. The numerical cost of a smoothing step depends on the number of iterations for the solution of (5.45) and (5.46) and on the dimension of the involved matrices. If a small number of elements is consid-

ered for each Vanka-block, the Local Multilevel Pressure Schur Complement is recovered (local MPSC). On the contrary, if the number of internal elements used in each Vanka-block is equal to the number of all elements in serial computations or to number of elements of the domain partition in parallel computations, the global Multilevel Pressure Schur Complement is recovered (global MPSC) (Turek [1999]). In this case we apply only a few iterations in order to prevent a very large increase of these costs and we employ the GMRES solver for which the norm of the residual is reduced in each iteration (Volker & Tobiska [2000]).

5. SOLVERS

Chapter 6

Numerical results

In this chapter we validate the proposed algorithm for a set of well known numerical benchmarks. This section is divided into three different sections, namely, the benchmarking and numerical performance of the Navier-Stokes code, the benchmarking and validation of the FSI code and the haemodynamics vessel wave propagation application.

6.1 Navier-Stokes Turek Benchmark

In the benchmark problem for the steady state Navier-Stokes equations defined in the DFG priority research program “Flow simulation with high-performance computer” and proposed by [Turek & Schäfer \[1996\]](#), coupled multigrid methods have been proven as efficient solvers for the incompressible Navier-Stokes equations. In this section a numerical study of the multilevel domain decomposition algorithm performed on this benchmark is presented. The problem describes the flow in a channel around a cylinder, which is slightly closer to the lower than to the upper wall.

6.1.1 Definitions

Geometry and computational mesh The geometry of the benchmark consists of a simple channel of length $L = 2.2 m$ and height $H = 0.41 m$. At point C a cylinder with radius $r = 0.05 m$ is placed (see [Figure 6.1](#)). The parameters

6. NUMERICAL RESULTS

which define the geometry are reported in Table 6.1. The geometry previously defined has to be discretized and partitioned in several domains of simple geometry. The output of the mesh processing is reported in Figure 6.2. The computational mesh for the simulations is obtained by successive regular or selective refinements of the coarse mesh of Figure 6.2. In Table 6.2 we have reported the number of elements and the number of degrees of freedom for each level of refinement. The following notation has been used:

- if we use only one number (e.g. 3) for indicating the level of refinement it means that the coarse mesh has been refined regularly over all the domain (light gray, gray and dark gray regions) for a number of times as indicated by the number;
- if we use two number separated by the *plus* symbol (e.g. 3 + 2), the first number indicates the number of successive regular refinement of the coarse mesh while the second number indicates the successive selective regular refinement of the gray and dark gray regions only (see Fig. 6.2) starting from the regularly refined mesh;
- if we use three number separated by the *plus* symbol (e.g. 3 + 2 + 1), the first number indicates the number of successive regular refinement of the coarse mesh, the second number indicates the successive selective regular refinement of the gray and dark gray region (see Fig. 6.2) starting from the regularly refined mesh while the third number indicates the successive selective regular refinement of the dark gray region only.

Fluid and Structure properties The fluid flow in the channel is described by the stationary incompressible Navier-Stokes equations for the velocity field $\mathbf{v} = (v_1, v_2)$ and the pressure p in the spatial (fixed) moving coordinate system

$$\begin{aligned} \rho(\mathbf{v} \cdot \nabla)\mathbf{v} + \nabla p - \mu\Delta\mathbf{v} &= \mathbf{0} && \text{in } \Omega^f, \\ \nabla \cdot \mathbf{v} &= 0 && \text{in } \Omega^f. \end{aligned}$$

We assume that no gravitation or other volume forces affect the fluid motion. The fluid is Newtonian characterized by a viscosity-parameter of $\mu = 0.001 \text{ Pa} \cdot \text{s}$

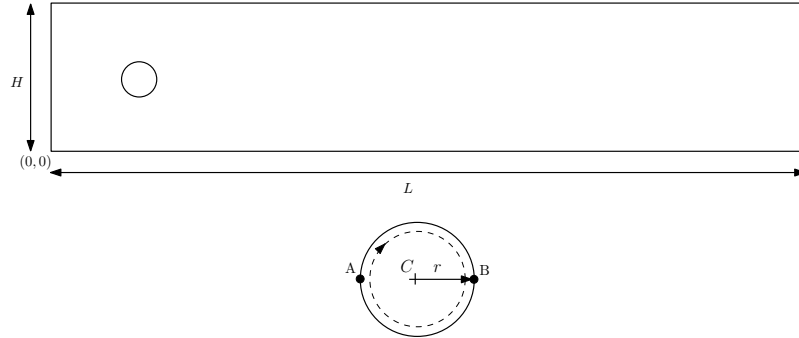


Figure 6.1: Computational domain.

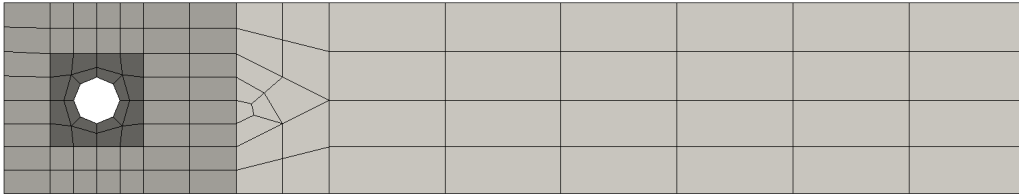


Figure 6.2: Coarse Mesh.

Table 6.1: Overview of the geometry parameters.

Geometry parameter	symbol	value
channel length	L	2.2 m
channel width	H	0.41 m
cylinder center position	C	(0.2 m, 0.2 m)
cylinder radius	r	0.05 m
reference point A	A	(0.15 m, 0.2 m)
reference point B	B	(0.25 m, 0.2 m)

and a density $\rho = 1 \text{ Kg/m}^3$.

Boundary and Initial conditions On the upper wall, lower wall and on the cylinder surface, a homogeneous Dirichlet boundary condition is imposed. The left wall is set to a parabolic inflow profile with maximum inflow velocity

6. NUMERICAL RESULTS

Table 6.2: Number of elements and degrees of freedom for refined levels.

Level	nel	ndof
0	98	1,178
1	392	4,512
2	1,568	17,648
3	6,272	57,248
4	25,088	277,568
3+2	63,872	705,216
4+1	71,168	643,328
5	100,352	1,006,720
2+4	246,368	2,715,008
4+2	255,488	2,815,616
3+2+1	81,920	1,252,416
6	401,408	4,421,888

$$U_{max} = 0.3$$

$$v_2(0, y) = \frac{4U_{max}y(H - y)}{H^2}. \quad (6.1)$$

The boundary condition on the right wall is the homogeneous Neumann boundary condition (i.e. do-nothing boundary condition). The benchmark setup results in a Reynolds number of

$$Re = \frac{2\rho U_{mean}r}{\mu} = 20,$$

with the characteristic velocity

$$U_{mean} = \frac{2}{3}U_{max} = 0.2$$

of the parabolic profile.

Quantities for Comparison In this stationary benchmark, the correctness and accuracy of the results are measured by the comparison of the following quantities of interest:

-
- The drag coefficient

$$C_D = \frac{2F_D}{2\rho U_{mean}^2 r},$$

- The lift coefficient

$$C_L = \frac{2F_L}{2\rho U_{mean}^2 r},$$

- The pressure drop

$$\Delta p = p(A) - p(B),$$

where A and B are the leftmost and rightmost point of the cylinder, respectively.

F_D and F_L are the forces exerted by the fluid on the whole submerged body, i.e. lift and drag forces acting on the cylinder

$$(F_D, F_L) = \int_S \boldsymbol{\sigma}^f \mathbf{n} dS,$$

where S (see Figure 6.1) is the surface of the cylinder and \mathbf{t} and \mathbf{n} denote the unit tangential and outer unit normal vector to the integration path, respectively. The definition of the Newtonian stress tensor $\boldsymbol{\sigma}$ is

$$\boldsymbol{\sigma} := -p\mathbf{I} + \mu\nabla\mathbf{v} = -p\mathbf{I} + \mu\frac{D\mathbf{v}_t}{D\mathbf{n}}\mathbf{n} = -p\mathbf{I} + \mu\langle D\mathbf{v} \cdot \mathbf{n}, \mathbf{t} \rangle \mathbf{t}$$

which leads to the following formula for calculating the forces

$$F_D = \int_S (\mu\frac{\partial\mathbf{v}_t}{\partial\mathbf{n}}n_y - pn_x)dS,$$

$$F_L = \int_S (-\mu\frac{\partial\mathbf{v}_t}{\partial\mathbf{n}}n_x - pn_y)dS.$$

The reference values for this benchmark are reported below

- $C_D = 5.57953523384,$
- $C_L = 0.010618948146,$
- $\Delta p = 0.11752016697.$

6. NUMERICAL RESULTS

Table 6.3: Results for the Turek-Navier Stokes benchmark.

Level	nel	ndof	F_drag	F_lift	Δp
1	392	4,512	4.8146589	0.0089345196	0.105267
2	1,568	17,648	5.1894628	0.0097317264	0.112725
3	6,272	57,248	5.3814652	0.0101664	0.115412
4	25,088	277,568	5.4790063	0.010380453	0.116521
3+2	63,872	705,216	5.52818446	0.010485166	0.117031
4+1	71,168	643,328	5.52818449	0.010485157	0.117031
5	100,352	1,006,720	5.528184550	0.010485159	0.117031
2+4	246,368	2,715,008	5.5528702	0.010538353	0.117278
4+2	255,488	2,815,616	5.5528708	0.01053829	0.117277
3+2+1	81,920	1,252,416	5.5528708	0.01053829	0.117277
6	401,408	4,421,888	5.5528708	0.01053829	0.117277
ref.			5.5529	0.01054	0.1173

6.1.2 Numerical Results

The results of the benchmark computations are summarized in Tables 6.3 and 6.4 and Figures 6.3, 6.4 and 6.5. Figure 6.3, 6.5 and 6.4 show the u-velocity field, the pressure field in the dark gray region and the plot of the pressure and drag and lift stresses over the circle perimeter, respectively. In Table 6.3 we reported the number of refinement, the number of elements, the number of unknowns, the drag and lift force and the delta pressure values for different levels of refinement. All the results we showed have been compared with the ones reported in Turek & Schäfer [1996] and are in total agreement. We can notice that using the Multilevel Domain Decomposition algorithm it is possible to obtain similar results by prescribing the same number of levels but with fewer degrees of freedom. For example you can compare the results obtained using 3+2+1 levels (ndof = 1,252,416) and 6 levels (ndof = 4,421,888): the drag and lift force integral values, which are computed using a user-defined filter implemented in Paraview, are the same.

The advantages of using our technique are highlighted by the execution times of the steady solver, reported in Table 6.4. The solution obtained with 4+2 levels

and 6 processors requires 22.27 s instead of 159.43 s of a serial solution with 6 levels. The solver implemented in the FEMTTU library is described in the previous chapter. The load-balancing is achieved using the Metis library. Each level of refinement is partitioned among the processors using the Metis library in order to address the load balance. Since the domain at level $n+1$ can be a subset of the domain at level n , the partitioning of level $n+1$ is performed independently of the previous partitions. This implies that the domain of processor p at level $n+1$ is not in general a subset of the same processor at the previous level. This can be seen clearly from Figure 6.6.

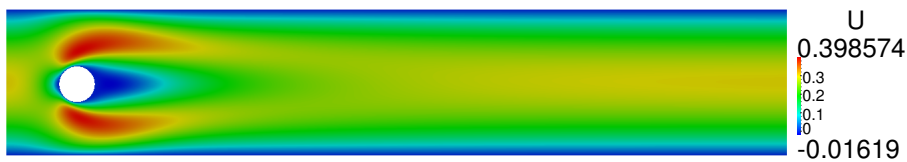


Figure 6.3: u velocity field.

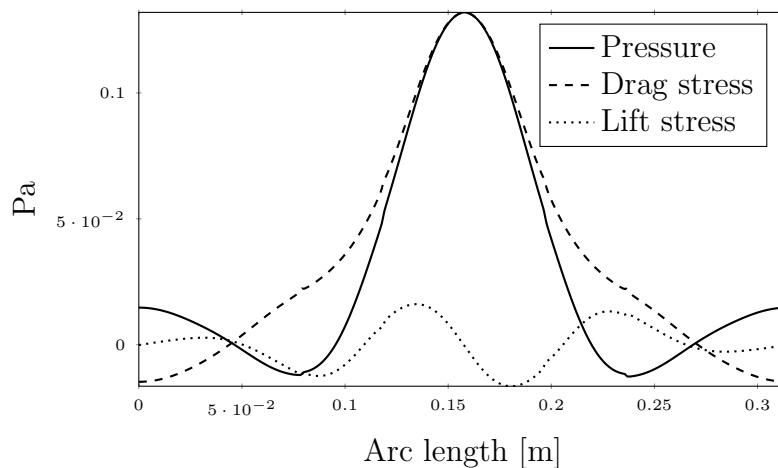


Figure 6.4: Plot of the pressure and drag and lift stresses over the circle perimeter.

6. NUMERICAL RESULTS

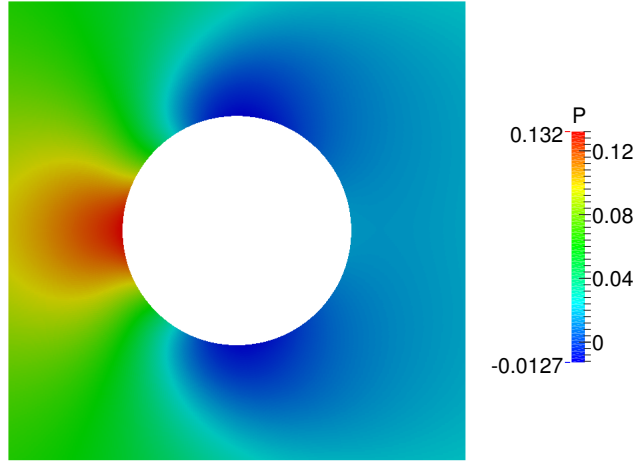


Figure 6.5: Pressure field in the dark gray region.

6.2 FSI numerical benchmarks

In this section two benchmark settings, one proposed by Turek in [Turek & Hron \[2006\]](#) and the other one by COMSOL Multiphysics, will be described in order to compare our results and validate our methodology.

6.2.1 FSI Hron-Turek Benchmark

In [Turek & Hron \[2006\]](#) the authors proposed a benchmark for testing and comparing different numerical methods and code implementations for fluid-structure interaction problems. This benchmark is based on the older successful *flow around cylinder* setting developed in [Turek & Schäfer \[1996\]](#) for incompressible laminar flow. The overall setup of this interaction problem consists of an elastic solid object which is submerged in a laminar channel flow. As the previous benchmark the fluid is incompressible and the structure is allowed to be compressible or incompressible. Then, self-oscillations in the fluid and solid part are obtained so that characteristic physical quantities and plots for the time-dependent results can be provided and compared. (see [Razzaq *et al.* \[2010\]](#); [Turek *et al.* \[2010a,b\]](#) for more details).

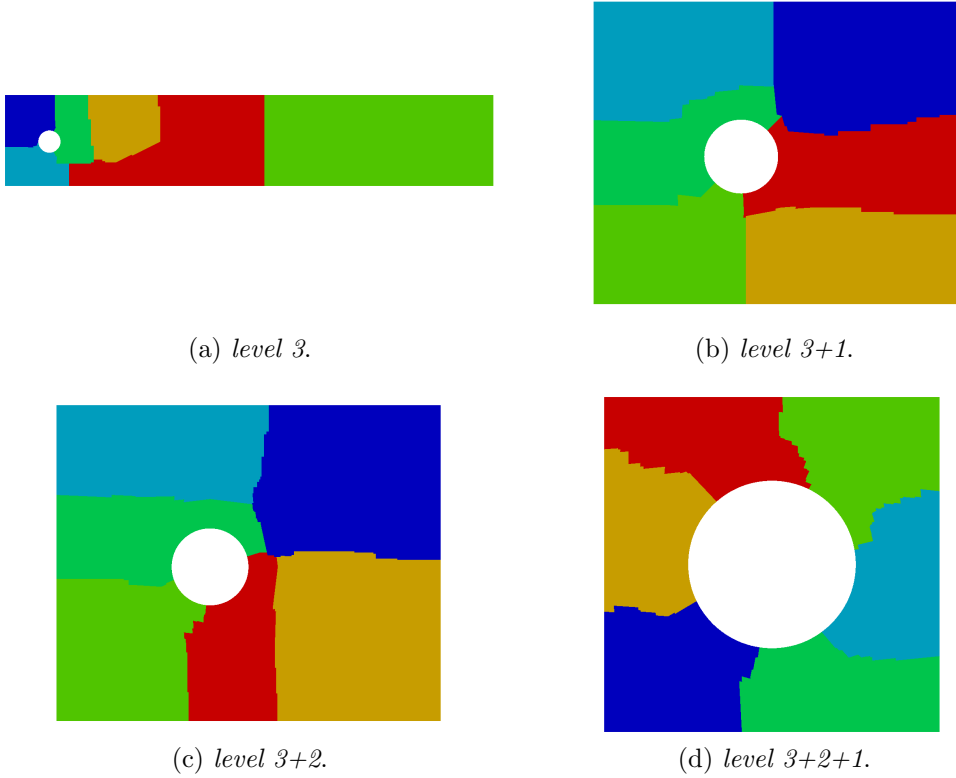


Figure 6.6: Domain partition among 6 processors for different levels of refinement: Figure (a) shows the domain partition of the whole region at level 3, Figure (b-c) the domain partition of the gray and dark gray regions at level 3+2, Figure (d) only the dark gray region at level 3+2+1.

Table 6.4: Execution times of the parallel steady Navier-Stokes solver.

Nproc	level	ndof	steady solver time (s)
1	6	4,421,888	159.43
1	4+2	2,815,616	83.49
2	4+2	2,815,616	59.50
3	4+2	2,815,616	40.07
4	4+2	2,815,616	32.87
5	4+2	2,815,616	29.04
6	4+2	2,815,616	22.27

6. NUMERICAL RESULTS

6.2.1.1 Definitions

Geometry and computational mesh The computational domain is based on the 2D version of the well-known *flow around cylinder* benchmark and it is showed in Figure 6.7. The parameters which define the geometry are reported in Table 6.5 and are given as follows:

- the domain dimensions are: length $L = 2.5m$, height $H = 0.41m$;
- the circle center is positioned at $C = (0.2m, 0.2m)$ (measured from the left bottom corner of the channel) and the radius is $r = 0.05m$;
- the elastic structure bar has length $l = 0.35m$ and height $h = 0.02m$; the right bottom corner is positioned at $(0.6m, 0.19m)$, and the left end is fully attached to the fixed and rigid cylinder;
- the control points is $A(t)$, attached to the structure with $A(0) = (0.6m, 0.2m)$.

The thickness and the length of the beam are chosen in order to reduce the bending stiffness without introducing additional numerical complications connected with high aspect ratios in the geometry. As reported in Turek & Schäfer [1996], the setting is intentionally non-symmetric to prevent the dependence of the onset of any possible oscillation on the precision of the computation.

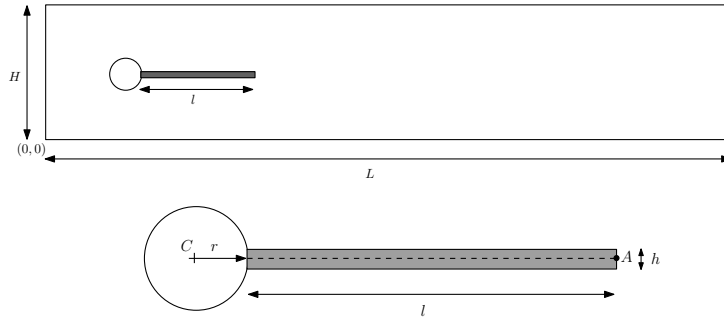


Figure 6.7: Computational domain and detail of the beam.

The geometry previously defined has to be discretized and partitioned in several domains of simple geometry. The output of the mesh processing is reported in Figure 6.8. The computational mesh for the simulations is obtained by successive regular or selective refinements of the coarse mesh of Figure 6.8. In Table 6.6

Table 6.5: Overview of the geometry parameters.

Geometry parameter	symbol	value
channel length	L	2.5 m
channel width	H	0.41 m
cylinder center position	C	(0.2 m, 0.2 m)
cylinder radius	r	0.05 m
elastic structure length	l	0.35 m
elastic structure thickness	h	0.02 m
reference point	A	(0.6 m, 0.2 m)

we have reported the number of elements and the number of degrees of freedom for each level of refinement. The same notation of the previous benchmark has been used for indicating the level of refinement.

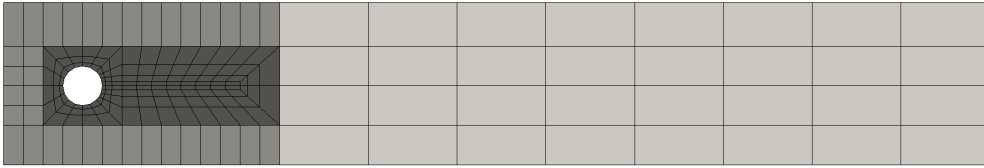


Figure 6.8: Coarse mesh.

Fluid and Structure properties The configuration of this benchmark is characterized by the interaction of a laminar flow and an elastic solid object. The fluid is considered to be Newtonian, incompressible and its state is described by the velocity \mathbf{v}^f and pressure p^f . The balance equations are the Navier-Stokes equations in the ALE formulation

$$\begin{aligned} \rho^f \frac{\partial \mathbf{v}^f}{\partial t} \Big|_{\tilde{A}} + \rho^f (\mathbf{v}^f - \mathbf{w}^f) \cdot \nabla \mathbf{v}^f - \nabla \cdot \boldsymbol{\sigma}^f &= \mathbf{0} & \text{in } (0, T) \times \Omega_t^f, \\ \nabla \cdot \mathbf{v}^f &= 0 & \text{in } (0, T) \times \Omega_t^f. \end{aligned}$$

6. NUMERICAL RESULTS

Table 6.6: Number of elements and degrees of freedom for refined levels.

Level	nel	ndof
1	792	15,640
1+1	2,784	53,952
2	3,168	61,376
2+1	11,136	213,696
3	12,672	243,136
2+2	43,008	821,120
4	50,688	967,808

The material constitutive equation is

$$\boldsymbol{\sigma}^f = -p^f \mathbf{I} + \rho^f \nu^f (\nabla \mathbf{v}^f + \nabla \mathbf{v}^{fT}).$$

The density and the kinematic viscosity are assumed constant and denoted by ρ^f and ν^f , respectively. The Reynolds number is denoted by $\text{Re} = \frac{2rU_m}{\nu^f}$, with the mean velocity $U_m = \frac{2}{3}v^f(0, \frac{H}{2}, t)$, r the radius of the cylinder and H the height of the channel (see Figure 6.7).

The structure is assumed to be elastic, Neo-Hookean and either compressible or incompressible. The solid state is described by the displacement \mathbf{u}^s and velocity \mathbf{v}^s if the material is compressible. When the material is incompressible the Lagrange multiplier p^s (i.e. the solid pressure) associated to the incompressibility constraint is introduced. However, the compressible solid equations can also make use of the solid pressure if the problem is properly reformulated. The balance equations are

$$J\rho^s \frac{\partial^2 \mathbf{u}^s}{\partial t^2} - \nabla \cdot \mathbf{P}^s = \mathbf{0} \quad \text{in } \Omega_0^s. \quad (6.2)$$

The first Piola Kirchhoff stress tensor \mathbf{P}^s is specified by the constitutive law of the Neo-Hookean material described in Chapter 2. The solid parameters are the solid density ρ^s , the Young Modulus E^s , the Poisson coefficient ν^s and the shear modulus μ^s . All these parameters are assumed to be constant.

Boundary and Initial conditions The FSI initial-boundary value problem at hand needs to prescribe some boundary and initial conditions.

- A parabolic velocity profile is prescribed in the left channel inflow section

$$\mathbf{v}^f(0, y) = 1.5U_m \frac{y(H-y)}{\left(\frac{H}{2}\right)^2} = 1.5U_m \frac{4.0}{0.1681} y(0.41 - y). \quad (6.3)$$

- The outflow condition can be chosen by the user. For example stress free or do nothing conditions. The outflow condition effectively prescribes some reference value for the pressure variable p . While this value could be arbitrarily set in the incompressible case, in the case of compressible structure this will have influence on the stress and consequently the deformation of the solid. In this benchmark, the reference pressure at the outflow section is set to have zero mean value.
- The *no-slip* condition is prescribed for the fluid on the other boundary edges. i.e. top and bottom wall, circle and fluid-structure interface.

Regarding to the initial conditions, we prescribed:

- zero velocity in the fluid and no deformation in the structure;
- for the non steady-tests we used as starting procedure a smooth increase of the velocity inlet profile in time as follow

$$v^f(0, y, t) = \begin{cases} v^f(0, y) \frac{1 - \cos(\frac{\pi}{2}t)}{2} & \text{if } t < 2.0, \\ v^f(0, y) & \text{otherwise,} \end{cases} \quad (6.4)$$

where the $v^f(0, y)$ is the velocity profile given in (6.3).

Material parameters The material parameters of the simulation are the fluid density, the solid density, the dynamic viscosity, the shear modulus and the Poisson coefficient. A minimal set of independent parameters can be obtained by using the Buckingham π theorem and it is made up of 4 elements, the density ratio $\beta = \frac{\rho^s}{\rho^f}$, the Reynolds number Re , the dimensionless shear modulus $Ae = \frac{\mu^s}{\rho^f U_m^2}$

6. NUMERICAL RESULTS

and the Poisson coefficient ν^s . An overview of certain material properties for some relevant fluids and elastic materials is shown in Tables 6.7 and 6.8. The choice of the fluid and solid properties for this benchmark is guided by several requirements. First, we would like the flow to be in the laminar regime, which implies a relatively small Reynolds number. A typical fluid candidate for the simulation is glycerine. Second, the stiffness of the beam should be low enough to allow significant deformations. Certain rubber-like materials fit into such a setting, namely polybutadiene (for an incompressible configuration) and polypropylene. In Tables 6.7 and 6.8 the combination of glycerine and polybutadiene is highlighted in grey.

Table 6.7: Overview of some solid material parameters.

Solid material	$\rho^s [10^3 \frac{Kg}{m^3}]$	ν^s	$E^s [10^6 \frac{Kg}{ms^2}]$	$\mu^s [10^6 \frac{Kg}{ms^2}]$
polybutadiene	0.910	0.50	1.6	0.53
polyurethane	1.200	0.50	25	8.33
polypropylene	0.890	0.42	900	317
PVC	1.400	0.42	1500	528
cork	0.180	0.25	32	81400
steel	7.800	0.29	210000	76000

Quantities for Comparison Comparisons will be performed both for steady state and time-dependent simulations. In the last case comparisons will be done for fully developed flow referring to one full period of the oscillation of the position of the point $A(t)$.

The quantities of interest are:

- The displacements u_1 and u_2 in x -direction and y -direction of the point $A(t)$ at the end of the beam structure (See Figure 6.7).
- Forces exerted by the fluid on the whole submerged body, i.e. lift and drag forces acting on the cylinder and the beam structure together

$$(F_D, F_L) = \int_S \boldsymbol{\sigma}^f \mathbf{n} dS = \int_{S_1} \boldsymbol{\sigma}^f \mathbf{n} dS + \int_{S_2} \boldsymbol{\sigma}^f \mathbf{n} dS,$$

Table 6.8: Overview of some fluid material parameters.

Fluid material	$\rho^f [10^3 \frac{Kg}{m^3}]$	$\nu^f [10^{-6} \frac{m^2}{s}]$	$\mu^f [10^{-3} \frac{Kg}{ms}]$
air	0.00123	0.015	0.018
acetone	0.790	0.405	0.32
ethyl alcohol	0.790	1.4	1.1
oil, vegetable	0.920	76.1	70
water	1.000	1.14	1.14
blood	1.035	3-4	3-4
glycerine	1.260	1127	1420
honey	1.420	7042	10000
mercury	13.594	0.0114	1.55

where $S = S_1 \cup S_2$ (see Figure 6.9) denoted the part of the circle being in contact with the fluid (i.e. S_1) plus the part of the boundary of the beam structure which is contact with the fluid (i.e. S_2) and \mathbf{n} is the outer unit normal vector to the integration path that points outward from the region inside the beam and the cylinder.

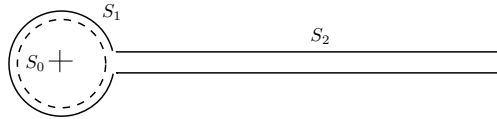


Figure 6.9: Integration path $S = S_1 \cup S_2$ for the force calculation.

Remark 6.2.1. *The force can be computed in several ways, i.e.:*

$$\begin{aligned}
 (F_D, F_L) &= \int_S \boldsymbol{\sigma}^f \mathbf{n} dS = \int_{S_1} \boldsymbol{\sigma}^f \mathbf{n} dS + \int_{S_2} \boldsymbol{\sigma}^f \mathbf{n} dS \\
 &= \int_{S_1} \boldsymbol{\sigma}^f \mathbf{n} dS + \int_{S_2} \boldsymbol{\sigma}^s \mathbf{n} dS \\
 &= \int_{S_1} \boldsymbol{\sigma}^f \mathbf{n} dS + \int_{S_2} \frac{1}{2} (\boldsymbol{\sigma}^f + \boldsymbol{\sigma}^s) \mathbf{n} dS \\
 &= \int_{S_0} \boldsymbol{\sigma} \mathbf{n} dS.
 \end{aligned}$$

6. NUMERICAL RESULTS

In the time dependent case the quantities for comparison are represented by the mean value, amplitude and frequency. The mean value and amplitude are computed from one full period of the oscillations by taking the maximum and minimum values and evaluating the average of the min/max values and the difference of the max/min from the mean, respectively

$$\begin{aligned}\text{mean} &= \frac{1}{2}(\max + \min), \\ \text{amplitude} &= \frac{1}{2}(\max - \min).\end{aligned}$$

The frequency of the oscillations can be computed either from the period time T as

$$\text{frequency} = \frac{1}{T},$$

or by using the Fourier analysis on the periodic data and taking the lowest significant frequency present in the spectrum. Additionally, a plot of the quantities over the period for different time integration scheme are showed.

6.2.1.2 Numerical Results

The results of the benchmark computations are summarized in Tables 6.10, 6.11 and 6.12: $u_1(\mathbf{A})$ and $u_2(\mathbf{A})$ denote the displacements in x - and y -direction of the point \mathbf{A} and F_D and F_L the drag and lift forces, respectively. For the unsteady case also the frequencies f_1 and f_2 obtained for the displacements $u_1(\mathbf{A})$ and $u_2(\mathbf{A})$, respectively, are given. The column “ndof” refers to the sum of unknowns for all velocity components, pressure, and displacement components.

All simulations have been performed with a fully implicit monolithic ALE-FEM method with a fully coupled multigrid solver as described in the previous chapter. For the validation of the employed fluid and solid solvers, we performed computations for different levels of spatial discretization (see Table 6.6). For the unsteady case the solutions are computed in one case with the first order Backward-Euler algorithm scheme for both fluid and solid equations and in the other case with the Backward-Euler algorithm scheme for the fluid equations and the second-order Generalized-alpha scheme for the solid equations. In both cases we adopted a constant time step size $\delta t = 0.001$.

Table 6.9: Parameter settings for the Hron-Turek FSI benchmarks.

Parameter	symbol	measure unit	FSI1	FSI3
Fluid density	ρ^f	$[10^3 \frac{Kg}{m^3}]$	1	1
Fluid viscosity	ν^f	$[10^{-3} \frac{m^2}{s}]$	1	1
Solid density	ρ^s	$[10^3 \frac{Kg}{m^3}]$	1	1
Poisson coefficient	ν^s	-	0.4	0.4
Shear modulus	μ^s	$[10^6 \frac{Kg}{m.s^2}]$	0.5	2
Density ratio	β	-	1	1
Dimensionless shear modulus	Ae	-	3.5×10^4	1.4×10^3
Average inlet velocity	U_m	$[\frac{m}{s}]$	0.2	2
Reynolds number	Re	-	20	200

The FSI tests are performed for two different inflow speeds. FSI1 is resulting in a steady state solution, while FSI3 results in a periodic solution. The parameter values for the FSI1 and FSI3 tests are given in the Table 6.9.

In Table 6.10, the quantities for comparison for the steady test case FSI1 are summarized. In Figure 6.10, resulting plots of $x - y$ displacement of the trailing edge point **A** of the elastic bar are drawn while the quantities for the non-steady test FSI3 are presented in Tables 6.12 and 6.11. The results show a (almost) grid independent solution behavior and the efficiency of the Multilevel Domain Decomposition algorithm. The selective refinement of the mesh allows to obtain similar results in the region of interest by prescribing the same number of levels but with fewer degrees of freedom. The advantages of this technique are clearly more relevant in the unsteady case.

Comparative benchmark results for different solution methods for fluid structure interaction problems are reported in Turek *et al.* [2010b] which have been developed as collaborative project under the DFG Research Unit 493. As a first result for the FSI1 benchmark, which leads to stationary displacement of the attached elastic beam, the authors found that all applied methods and codes can approximate the same results, at least with decreasing mesh width Turek *et al.* [2010b]. Evidently for FSI3, the evaluation of the results is a little bit more dif-

6. NUMERICAL RESULTS

difficult: first of all, all schemes show the tendency to converge towards the (more or less) same solution values, at least for increasing mesh level. Although the applied FSI techniques are very different w.r.t. discretization, solver and coupling mechanisms, the authors found that the FSI3 benchmark setting proves to be a very valuable tool for numerical FSI benchmarking, leading to grid independent results for the prescribed geometrical and parameter settings [Turek *et al.* \[2010b\]](#). The comparison of our results with the ones reported in [Turek *et al.* \[2010b\]](#) shows the feasibility and the accuracy of the proposed methodology.

Table 6.10: Results for FSI1.

Level	nel	ndof	$u_1(\mathbf{A})[\times 10^{-3}]$	$u_2(\mathbf{A})[\times 10^{-3}]$	drag	lift
1	792	15,640	0.02277155	0.81681181	14.29122	0.77623
1+1	2,784	53,952	0.02274367	0.81965970	14.29003	0.77545
2	3,168	61,376	0.02274210	0.81849791	14.28967	0.77512
2+1	11,136	213,696	0.02271311	0.81851485	14.28495	0.77474
3	12,672	243,136	0.02271325	0.81848982	14.28475	0.77456
2+2	43,008	821,120	0.02269696	0.81858452	14.28439	0.77428
4	50,688	967,808	0.02269713	0.81855286	14.28432	0.77424
ref.			0.0227	0.818	14.284	0.774

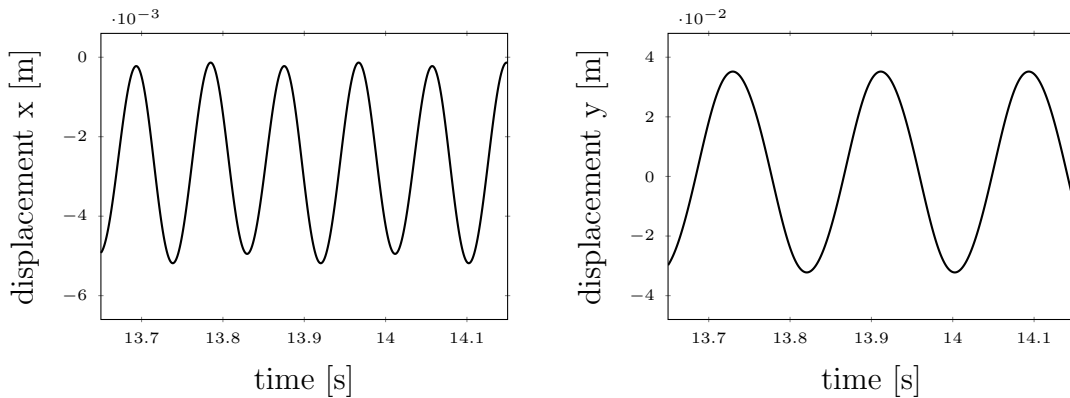


Figure 6.10: x and y displacement of the point A.

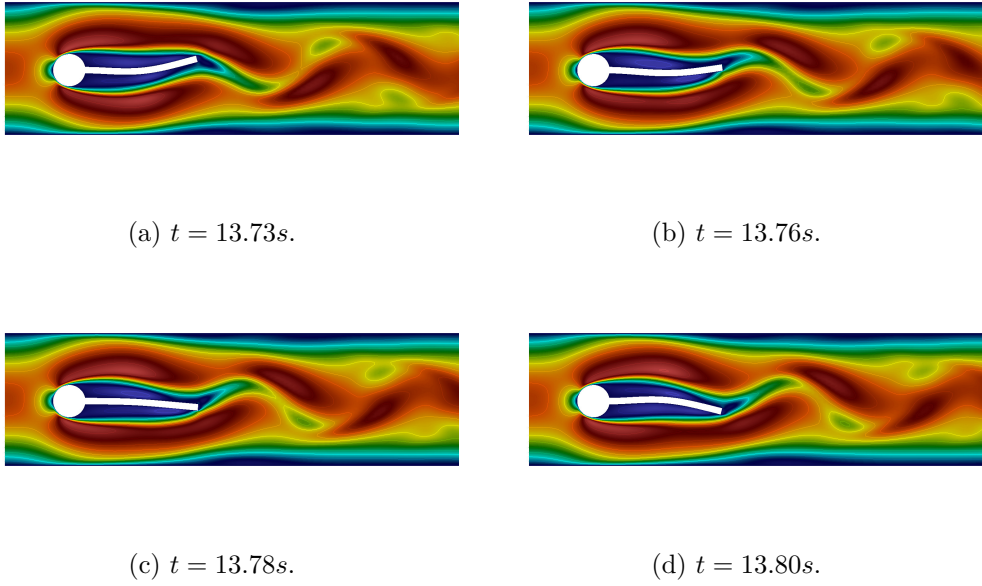


Figure 6.11: Fluid flow during one-half oscillation for the FSI3 benchmark.

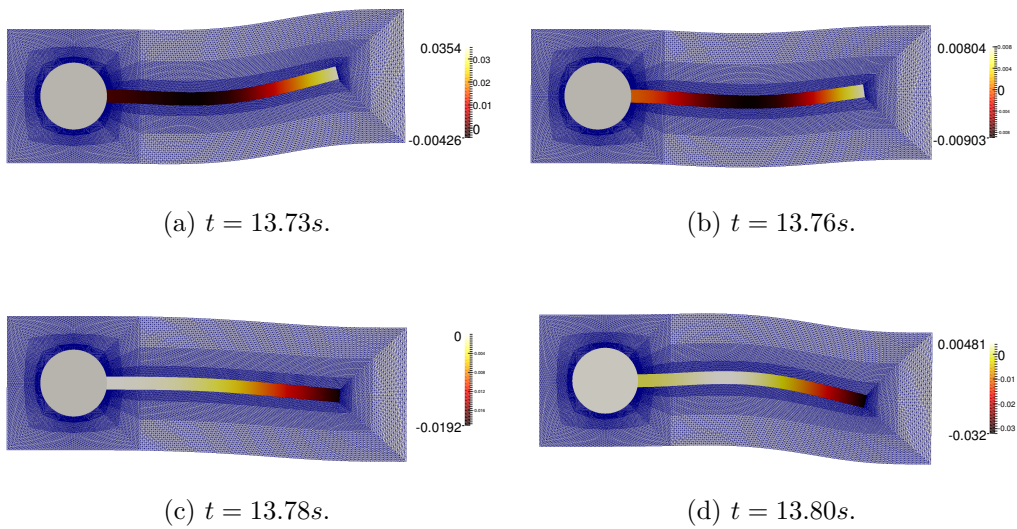


Figure 6.12: y -displacement field during one-half oscillation for the FSI3 benchmark.

6. NUMERICAL RESULTS

Table 6.11: Results for FSI3 using the Backward-Euler algorithm for both fluid and solid equations.

Level	nel	ndof	$u_1(\mathbf{A})[\times 10^{-3}]$	$u_2(\mathbf{A})[\times 10^{-3}]$	f_1	f_2
1	792	15,640	-3.62 ± 3.39	1.48 ± 39.72	5.32	5.32
2	3,168	61,376	-2.69 ± 2.55	1.53 ± 33.86	5.49	5.49
2+1	11,136	213,696	-2.65 ± 2.53	1.49 ± 33.72	5.49	5.49
3	12,672	243,136	-2.66 ± 2.52	1.49 ± 33.70	5.49	5.49
ref.			-2.66 ± 2.52	1.49 ± 33.70	5.49	5.49

Table 6.12: Results for FSI3 using the Backward-Euler algorithm for the fluid equations and the Generalized-alpha algorithm for the solid equations.

Level	nel	ndof	$u_1(\mathbf{A})[\times 10^{-3}]$	$u_2(\mathbf{A})[\times 10^{-3}]$	f_1	f_2
1	792	15,640	-3.67 ± 3.49	1.36 ± 40.00	5.46	5.43
2	3,168	61,376	-2.74 ± 2.61	1.59 ± 34.06	5.49	5.49
2+1	11,136	213,696	-2.70 ± 2.60	1.54 ± 33.94	5.49	4.49
3	12,672	243,136	-2.70 ± 2.58	1.54 ± 33.92	5.49	5.49
ref.			-2.70 ± 2.58	1.54 ± 33.92	5.49	5.49

6.2.2 FSI COMSOL Multiphysics Benchmark

This example is based on a 2D classical benchmark proposed by COMSOL Multiphysics to demonstrate its techniques for modeling fluid-structure interactions. The aim of this benchmark is to compare our results obtained with the methodology described in the previous chapters with the ones obtained with a commercial FSI code implementing a partitioned algorithm.

The overall setup of this FSI problem consists of a narrow vertical structure attached to the bottom wall of a horizontal channel which bends under the force due to viscous drag and fluid pressure. As the previous benchmark the fluid is incompressible and the structure is compressible. The boundary conditions are time-dependent but are defined in order to get a transient solution which

converges after a certain period of time to a steady state.

6.2.2.1 Definitions

Geometry and computational mesh The model geometry consists of a horizontal flow channel in the middle of which an obstacle, a narrow vertical structure, is placed. The fluid flows from left to right, except where the obstacle forces it to flow into a narrow path in the upper part of the channel, and it imposes a force onto the structure's wall resulting from the viscous drag and fluid pressure. The structure, being made of a deformable material, bends under the applied force modifying the path followed by the fluid flow. The parameters which define the geometry are reported in Table 6.13 and described as follows:

- the channel dimensions are: length $L = 300\mu m$, height $H = 100\mu m$;
- the elastic vertical structure has length $l = 35\mu m$ and height $h = 5.5\mu m$; the left side is positioned at $d = 100\mu m$ away from the channel's left boundary and the bottom end is fully attached to the bottom wall of the channel; the top end of the beam is semicircular which radius is $r = 5\mu m$;
- the control point is $A(t)$, attached to the top of the vertical narrow structure with $A(0) = (105\mu m, 55\mu m)$.

As for the previous benchmark, the thickness and the length of the vertical structure are chosen in order to get a significant excursion of the beam without introducing additional numerical complications connected with high aspect ratios in the geometry.

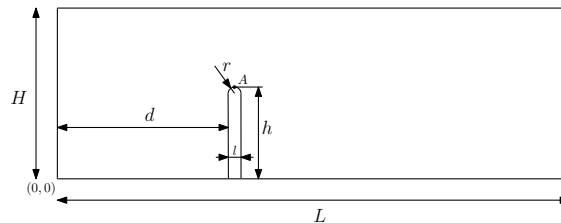


Figure 6.13: Computational domain.

The geometry previously defined has to be discretized and partitioned in several domains of simple geometry. The output of the mesh processing is reported

6. NUMERICAL RESULTS

Table 6.13: Overview of the geometry parameters.

Geometry parameter	symbol	value
channel length	L	$3.e^{-04}m$
channel height	H	$1.e^{-04}m$
rounded-end beam radius	r	$5.e^{-06}m$
beam distance from the inlet section	d	$1.e^{-04}m$
beam length	l	$1.e^{-05}m$
beam height	h	$5.5e^{-05}m$
reference point	A	$(1.05e^{-04}m, 5.5e^{-05}m)$

in Figure 6.14. The computational mesh for the simulations is obtained by successive regular or selective refinements of the coarse mesh of Figure 6.14. Since we are interested in the accurate computation of the drag and lift forces acting on the beam and of the displacements of the top end of the beam, the region highlighted in gray (see Figure 6.14) will be used for selective refinement. The same notation of the previous benchmark has been used for indicating the level of refinement. In Table 6.14 we have reported the number of elements and the number of degrees of freedom for each level of refinement.

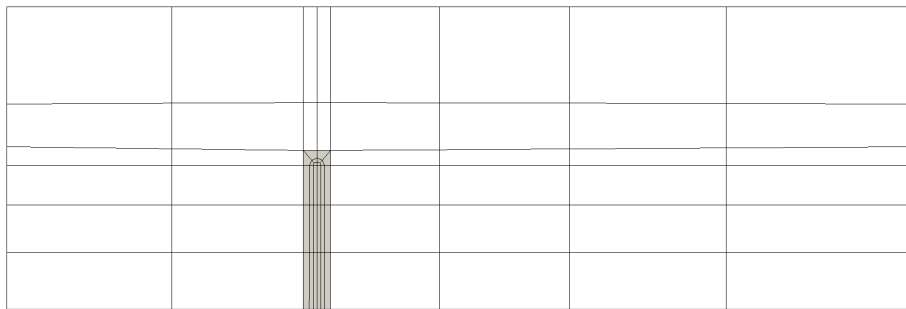


Figure 6.14: Coarse mesh.

Table 6.14: Number of elements and degrees of freedom for refined levels.

Level	nel	ndof
2	1,088	21,188
2+1	2,432	46,980
3	4,352	83,716
2+2	7,808	149,636
3+1	9,728	186,372
4	17,408	332,804

Fluid and Structure properties The fluid flow in the channel is described by the incompressible Navier-Stokes equations for the velocity field \mathbf{v} and the pressure p in the ALE (deformed) moving coordinate system. We assume that no gravitation or other volume forces affect the fluid motion. As fluid for the test, an incompressible water-like substance with a density $\rho^f = 1000Kg/m^3$ and dynamic viscosity $\mu^f = 0.001Pa \cdot s$ has been used.

The structural deformations are solved for using a neo-Hookean hyperelastic material model and a nonlinear geometry formulation to allow large deformations. The structure consists of a narrow vertical flexible material with a density of $\rho^s = 7850Kg/m^3$, Young's modulus $E = 200kPa$ and Poisson coefficient $\nu^s = 0.30$.

Boundary and Initial conditions At the channel entrance on the left, the flow has fully developed laminar characteristics with a parabolic velocity profile but its amplitude changes with time. At first flow increases rapidly, reaching its peak value at 0.215 s; thereafter it gradually decreases to a steady-state value of 5 cm/s. The centerline velocity in the x -direction, $v^f(0, \frac{H}{2}, t)$ (see Figure 6.18), with the steady-state amplitude U comes from the equation

$$v^f(0, \frac{H}{2}, t) = \frac{U \cdot t^2}{\sqrt{(0.04 - t^2)^2 + (0.1t)^2}},$$

where t must be expressed in seconds.

At the outflow (right-hand boundary), the do-nothing condition is prescribed. On the solid (non-deforming) walls, no-slip conditions are imposed, $\mathbf{v} = \mathbf{0}$, while

6. NUMERICAL RESULTS

on the deforming interface the continuity of the velocity is prescribed.

The obstacle is fixed to the bottom of the fluid channel. All other beam boundaries experience a load from the fluid, given by

$$\boldsymbol{\sigma}_{|\gamma_i}^s = (-p^f \mathbf{I} + \mu^f (\nabla \mathbf{v} + (\nabla \mathbf{v})^T)) \cdot \mathbf{n},$$

where \mathbf{n} is the normal vector to the boundary. This load represents the sum of pressure and viscous drag forces.

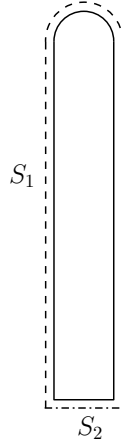


Figure 6.15: Integration path for the force calculation.

Quantities for Comparison Comparisons will be done when the solution reaches the steady-state configuration. The quantities of interest are:

- The displacements u_1 and u_2 in x -direction and y -direction of the point $A(t)$ at the top end of the beam structure (See Figure 6.13).
- Forces exerted by the fluid on the whole submerged body, i.e. lift and drag forces acting on the beam structure

$$(F_D, F_L) = \int_{S_1} \boldsymbol{\sigma}^f \mathbf{n} dS = - \int_{S_2} \boldsymbol{\sigma}^s \mathbf{n} dS,$$

where S_1 (dashed path, see Figure 6.15) denoted the part of the beam being in contact with the fluid, S_2 (dash dotted path, see Figure 6.15) denoted

the part of the beam attached to the bottom wall of the channel and \mathbf{n} is the outer unit normal vector to the integration path that points outward from the region inside the beam.

6.2.2.2 Numerical results

In this FSI benchmark we are interested in the computation of the displacement of a beam subjected to a bending force in order to highlight the potentiality of the Multilevel Domain Decomposition algorithm that has been presented in the previous chapter. The results of the benchmark computations are collected in Tables 6.15. We reported the number of refinement, the number of elements, the number of dofs, the x and y displacements and the drag and lift forces. We can notice that using the Multilevel Domain Decomposition algorithm it is possible to obtain similar results in the region of interest by prescribing the same number of levels but with fewer degrees of freedom. For example you can compare the results obtained using 3+1 levels (ndof = 186,372) and 4 levels (ndof = 332,804). The reference values are compared with the results obtained by solving the model using COMSOL Multiphysics. Subdividing the geometry described above in 69,864 triangular elements and discretizing the unknowns with Lagrangian finite element, resulting in 185,770 dofs, we found $u_1(\mathbf{A}) = 1.0915e^{-05}$ and $u_2(\mathbf{A}) = -1.38413e^{-06}$, which are in agreement with our results. The small differences are due to the different compressible Neo-Hookean model implemented in COMSOL Multiphysics.

Figure 6.16 shows the geometry deformation and the fluid flow at $t = 4s$ when the system is close to its steady state. Due to the channels small dimensions, the Reynolds number of the flow is small ($Re \ll 100$), and the flow stays laminar in most of the area. The swirls are restricted to a small area behind the structure. The amount of deformation as well as the size and location of the swirls depend on the magnitude of the inflow velocity.

Figure 6.17 shows the mesh deformation at different times. The first image shows the initial mesh, which you generate prior to solving the model. The mesh is refined selectively around the beam where a more accurate solution is desired. As you can see the mesh elements are smaller near the top of the beam where

6. NUMERICAL RESULTS

Table 6.15: Results for COMSOL benchmark.

Level	nel	ndof	$u_1(\mathbf{A})$	$u_2(\mathbf{A})$	drag	lift
2	1,088	21,188	$1.080789e^{-05}$	$-1.357274e^{-06}$	0.0094275	-0.395467
2+1	2,432	46,980	$1.082260e^{-05}$	$-1.361050e^{-06}$	0.0083059	-0.384256
3	4,352	83,716	$1.081792e^{-05}$	$-1.359843e^{-06}$	0.0083106	-0.384255
2+2	7,808	149,636	$1.082794e^{-05}$	$-1.361782e^{-06}$	0.0083124	-0.384256
3+1	9,728	186,372	$1.082661e^{-05}$	$-1.361700e^{-06}$	0.0050632	-0.384362
4	17,408	332,804	$1.082601e^{-05}$	$-1.361546e^{-06}$	0.0050521	-0.384331
ref.			$1.0826e^{-05}$	$-1.361e^{-06}$	0.005	-0.384

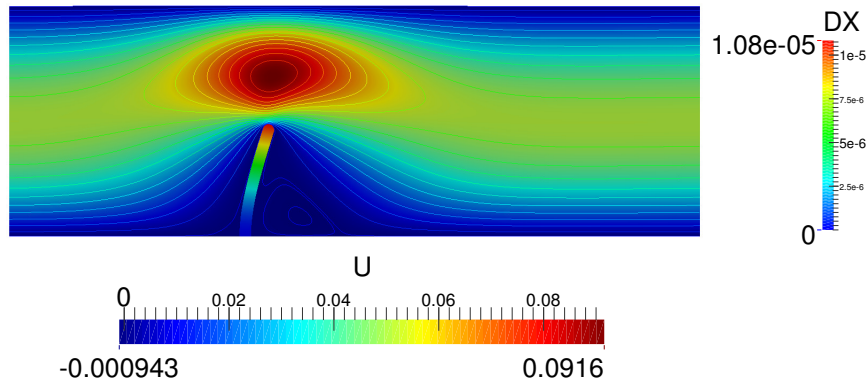


Figure 6.16: u velocity and mesh deformation at $t = 4s$; the contour lines indicates the u velocity field.

the mesh undergoes large distortion. The ALE map is constructed as explained in Chapter 3: the smaller the elements are, the stiffer they behave resulting in a mesh of higher quality. The second image shows the mesh in its deformed state when the beam reaches the maximum x-elongation. Because the structure deforms more in the horizontal direction, the mesh also changes more in this direction: on the left, the mesh elements are stretched; on the right, they are compressed in the x direction.

The boundaries of the narrow structure are the only moving boundaries of the flow channel. Therefore the mesh velocity also has its largest values near

the structure. Depending on the current state of the deformation – whether it is increasing, decreasing or stationary – the mesh velocity can have a very different distribution. Figure 6.18 further illustrates this point: it compares the maximum inflow velocity to the horizontal mesh velocity and the horizontal mesh displacement just above the top of the structure. Most of the time the deformation follows the inflow velocity quite closely. Whenever the inflow velocity starts to decrease, the deformation also decreases, which you can observe as the negative values on the horizontal mesh velocity. Toward the end of the simulation, when inflow and structure deformation approach their steady-state values, the mesh velocity also decreases to zero.

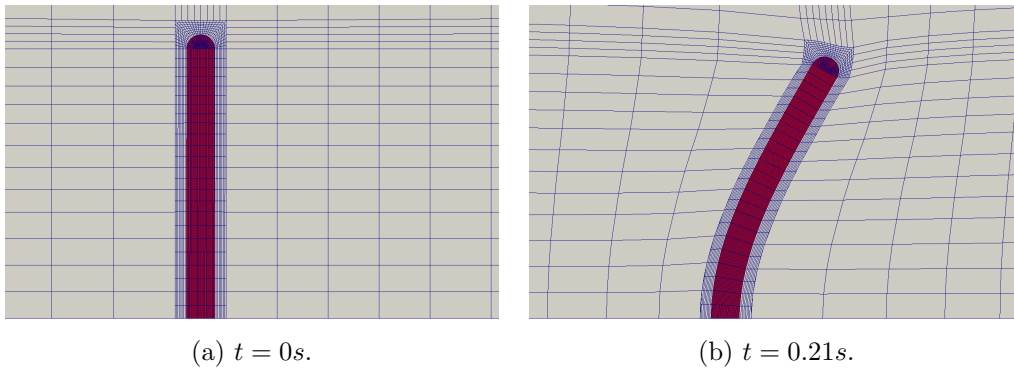


Figure 6.17: Geometry and mesh near the top of the structure at $t = 0s$ and $t = 0.21s$.

6.3 Biomedical application: wave propagation in a compliant vessel

We consider in this section the academic fluid-structure numerical test arising in the modeling of blood flow in large arteries, which consists in simulating the pressure wave propagation through a thin straight compliant vessel. This test case, originally proposed in Formaggia *et al.* [2001], has been extensively used in the literature as a benchmark (see e.g., Fernández & Moubachir [2005]; Fernández *et al.* [2007]; Gerbeau & Vidrascu [2003]), in order to illustrate the efficiency of different fluid-structure coupling algorithms proposed in literature. This problem is very

6. NUMERICAL RESULTS

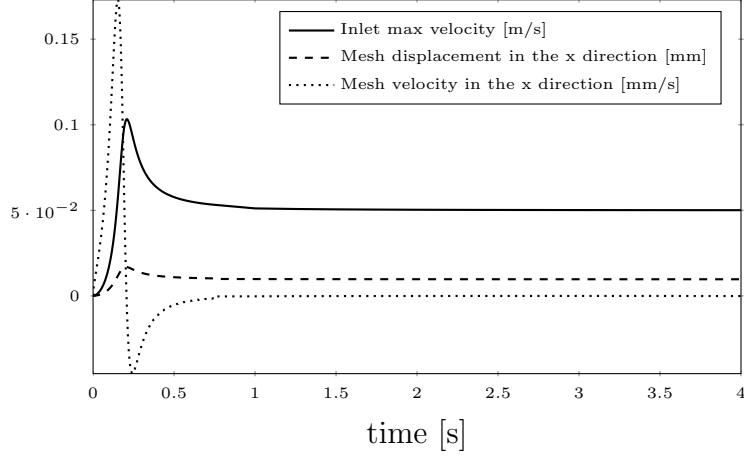


Figure 6.18: Inflow maximum velocity, horizontal mesh deformation and mesh velocity. The solid curve shows the maximum u velocity at the inflow boundary (m/s); the dashed one shows the mesh displacement in the x direction (mm) at the geometry point $(1.00275e^{-04}m, 6.83267e^{-05}m)$; the dotted one shows the mesh velocity in the x direction (mm/s) at the same point.

interesting from the mathematical and numerical modeling viewpoints: indeed, even if the flow is governed by parabolic equations such as the time-dependent incompressible Navier-Stokes, the overall behavior of the coupled fluid-structure system is in many aspects more similar to that of a hyperbolic problem. As a consequence, if the inflow and outflow boundary conditions are not chosen properly, an incorrect representation of the traveling waves with spurious reflections is observed (Formaggia *et al.* [2001]), see Figure 6.24. This problem has been tackled in Formaggia *et al.* [2001] by coupling the 3D fluid-structure problem with a reduced one-dimensional model, which acts as an “absorbing” device for the waves exiting the computation domain. Finally, the problem is axisymmetric but has been treated as a three-dimensional one in order to show the applicability of our approach also to three-dimensional time-dependent problems.

6.3.1 Definitions

Geometry and computational mesh The model geometry consists of a straight cylinder of radius $r = 5.e^{-03}m$ and length $l = 5.e^{-02}m$ discretized by 3D 27-node hexagonal elements, see Figure 6.20. The surrounding structure has

a thickness of 0.005 m which is represented by one layer of 3D 27-node hexagonal solid elements. The parameters which define the geometry are reported in Table 6.16 for sake of clarity. The fluid (light gray) and solid (dark gray) coarse computational mesh is shown in figure 6.20. The finer computational mesh are obtained by successive regular or selective refinements of the coarse mesh of Figure 6.20. We decided to refine selectively the surrounding structure since we are interested in the maximum interface displacement magnitude. The same notation of the previous benchmarks has been used for indicating the level of refinement. In Table 6.17 we have reported the number of elements and the number of degrees of freedom for each level of refinement.

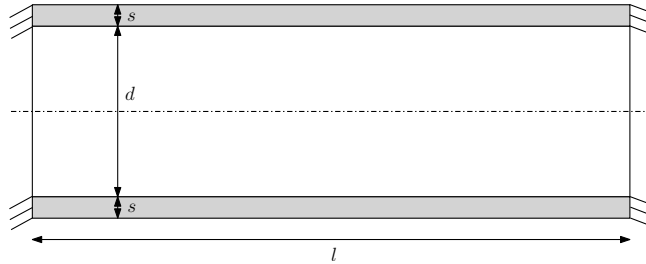


Figure 6.19: Computational domain.

Table 6.16: Overview of the geometry parameters.

Geometry parameter	symbol	value
channel length	l	$5.e^{-02}$
channel diameter	d	$1.e^{-02}$
channel radius	r	$5.e^{-03}$
structure thickness	s	$1.e^{-03}$

Fluid and Structure properties The fluid flow in the channel is described by the incompressible Navier-Stokes equations for the velocity field \mathbf{v} and the pressure p in the ALE (deformed) moving coordinate system. We assume that no gravitation or other volume forces affect the fluid motion. As fluid for the

6. NUMERICAL RESULTS

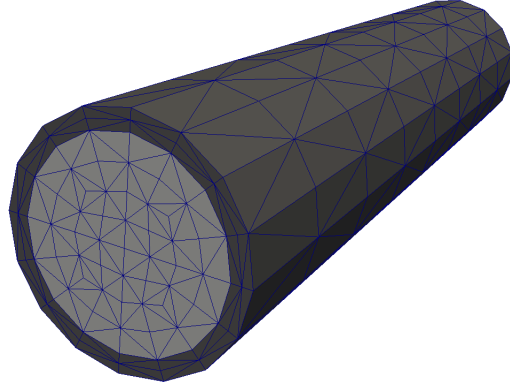


Figure 6.20: Coarse mesh.

Table 6.17: Number of elements and degrees of freedom for refined levels.

Level	nel	ndof
0	80	5,126
1	640	36,934
1+1	2,048	140,294
2	5,120	280,454

test, an incompressible blood-like substance with a density $\rho^f = 1000Kg/m^3$ and dynamic viscosity $\mu^f = 0.003Pa \cdot s$ has been used.

The structural deformations are solved for using the Saint-Venant-Kirchhoff hyperelastic material model. The structure consists of a thin straight compliant vessel with a density of $\rho^s = 7850Kg/m^3$, Young's modulus $E = 3 \cdot 10^5Pa$ and Poisson coefficient $\nu^s = 0.3$.

Boundary and Initial conditions Both systems, the fluid and the structure, are initially at rest. An over pressure of $1333.2Pa$ ($10mmHg$) is imposed on the inlet boundary during $3 \times 10^{-3} s$ while at the outflow (right-end boundary), the do-nothing condition is prescribed. The structure is clamped at the inlet and outlet boundaries. On the solid external surface, the stress free boundary condition is imposed, while on the deforming interface the continuity of the velocity and of

the stress is prescribed, given by

$$\mathbf{v}_{|\gamma_i}^s = \mathbf{v}_{|\gamma_i}^f \quad \boldsymbol{\sigma}_{|\gamma_i}^s = \boldsymbol{\sigma}_{|\gamma_i}^f = (-p^f \mathbf{I} + \mu^f (\nabla \mathbf{v} + (\nabla \mathbf{v})^T)) \cdot \mathbf{n},$$

where \mathbf{n} is the normal vector to the interface.

The boundary data imposed on the inlet and outlet boundaries do not have any physiological meaning (Fernández & Moubachir [2005]). Let us notice that the typical period of a heart beat is about 1 second. The scope of this benchmark is not to provide realistic physiological simulations of the interaction between the blood and the arterial wall but to test our solution algorithm on a simplified representation of this phenomena and to compare our results.

Quantities for Comparison The solution is time-dependent and decays over time to the null solution. We restrict our observation to the time interval between 0 s and 0.05 s. As quantitative outputs for comparison we provide

- the maximum interface displacement magnitude;
- the inlet and outlet flow-rates.

6.3.2 Numerical results

A pressure wave propagation is observed during the simulation (see Figure 6.24). Figure 6.24 shows the fluid pressure at time $t = 0.0025, 0.005, 0.0075, 0.01, 0.0125, 0.015, 0.0175, 0.02s$ with the time step $\Delta t = 1e^{-04}s$. In Figure 6.25 the corresponding solid deformed configurations (half section) are displayed. We also provides for this test case a few quantitative outputs: the maximum interface displacement, the inlet and outlet flow-rates and the solid displacement magnitude in the middle section of the cylinder for different meshes. From the observation of Figure 6.22 we can clearly observe the phase shift between the inflow and outflow maximum velocities due to the compliance of the vessel wall. Figure 6.21 and 6.23 shows clearly that pressure waves are traveling along the vessel. In particular, due to the incorrect representation of the traveling waves, spurious reflections occur resulting in a different solution behavior after about $t = 0.01s$ from what it is observed in the works presented in Fernández & Moubachir [2005], Formaggia *et al.*

6. NUMERICAL RESULTS

[2001] and Formaggia *et al.* [2009]. Figure 6.23 shows also the solution behavior for different meshes. It can be noticed that a (almost) grid independent solution behavior is obtained if at least one refinement is performed and if the time is less than $t < 0.01s$. In particular the solution obtained with 1+1 levels is very similar to the solution obtained with 2 levels, therefore in this example no advantages can be achieved using the multilevel domain decomposition algorithm with the selective refinement prescribed in the surrounding structure, as explained above. Further investigations on this issue will be addressed in the future.

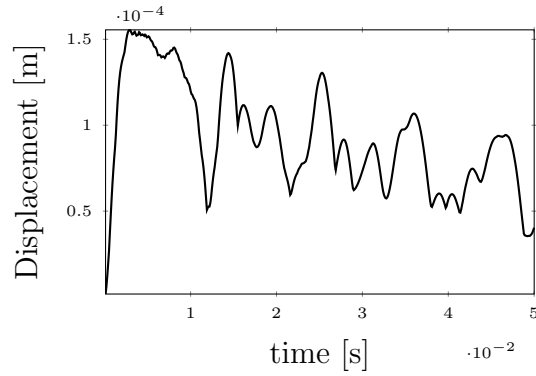


Figure 6.21: Maximum solid displacement magnitude.

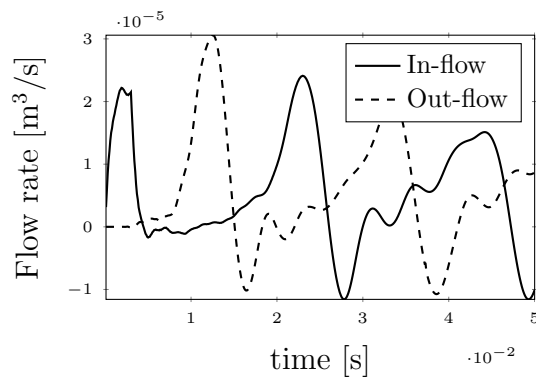


Figure 6.22: In- and out-flow rates.

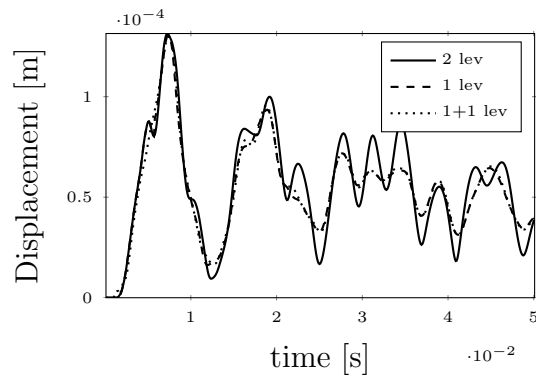


Figure 6.23: Plot over time of the solid displacement magnitude in the middle section of the cylinder for different meshes.

6. NUMERICAL RESULTS

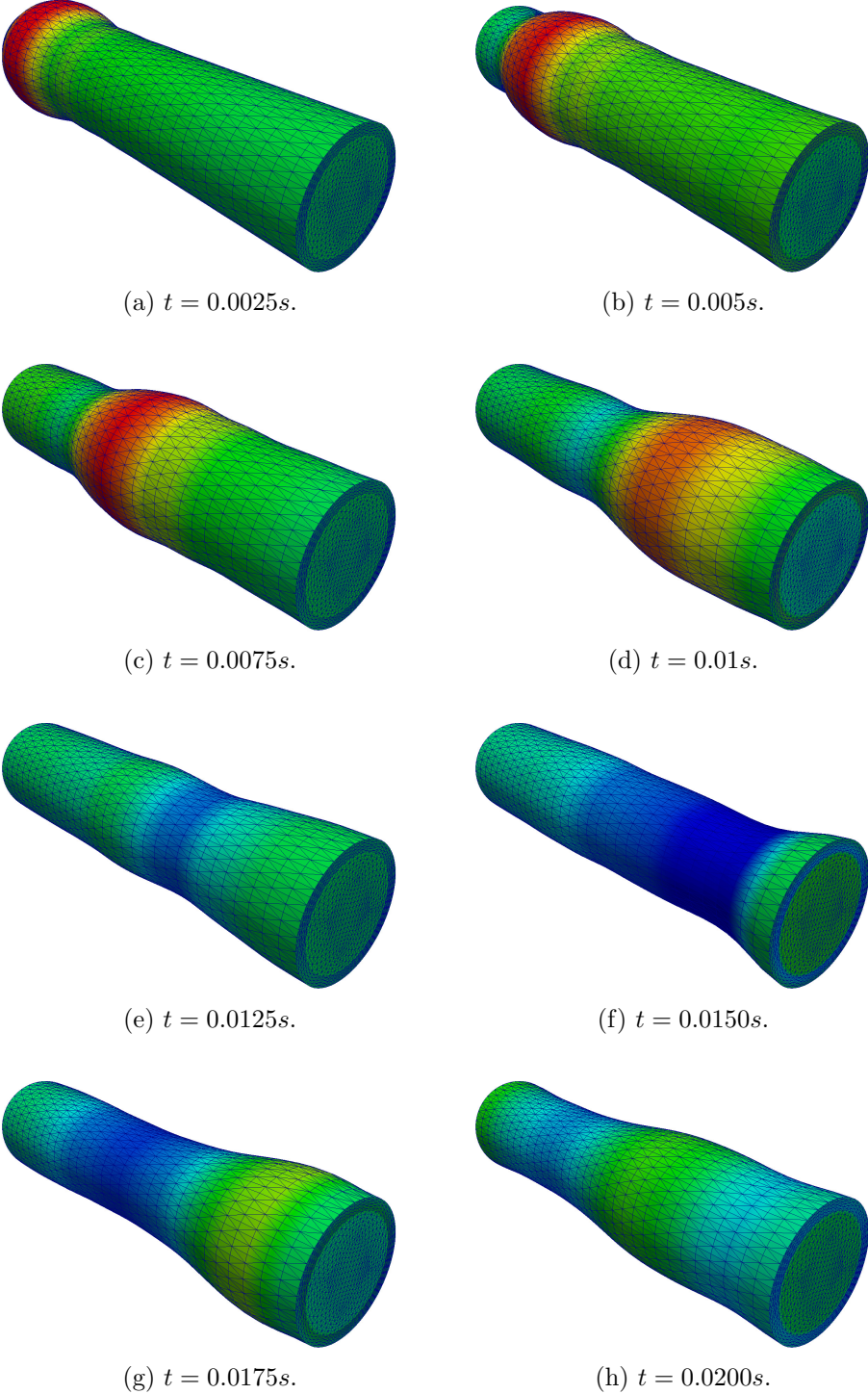


Figure 6.24: Pressure wave propagation.

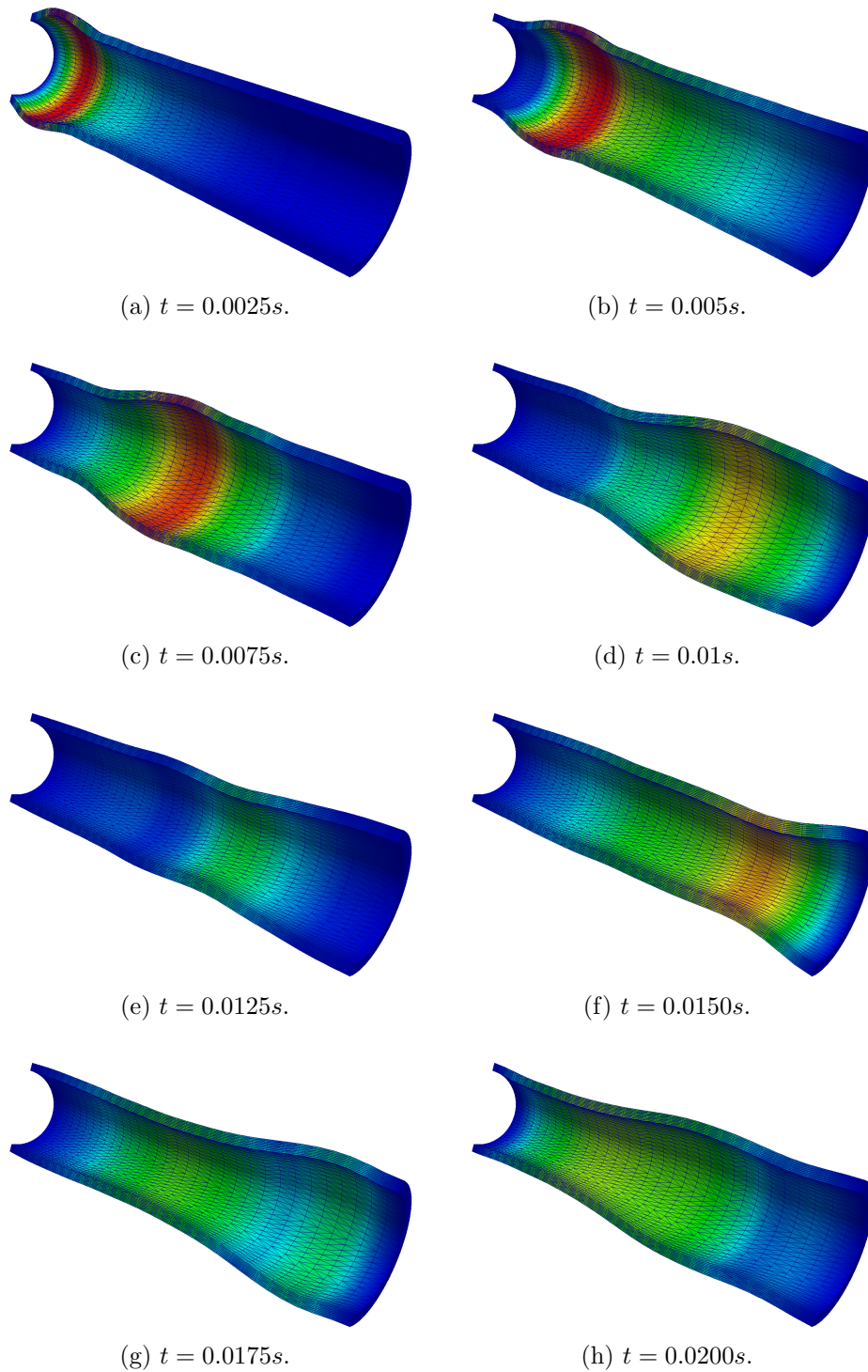


Figure 6.25: Solid domain deformed configuration.

6. NUMERICAL RESULTS

Chapter 7

Conclusions

The work presented in this thesis describes the research activity carried out to develop efficient and accurate algorithms for the solution of fluid-structure interaction problems. The performance and accuracy of the proposed methodology has been analyzed by conducting extensive and accurate simulations and compared with existing standard benchmark settings. This concluding chapter presents a summary of the work undertaken and the results achieved by applying our numerical solution methodology to FSI problems. We will also point out areas where further research should be performed in order to ensure a continual progress.

In this thesis we have presented some finite element techniques for solving the problem of fluid-structure interaction of an elastic solid material (either incompressible or compressible) in a laminar incompressible viscous flow. The mathematical problem consists of the Navier-Stokes equations in the Arbitrary Lagrangian-Eulerian (ALE) formulation coupled with a non-linear structure model, considering the problem as one continuum. Since we are interested in solving FSI problems where the added-mass effect is significant, the coupling between the structure and the fluid is enforced inside a monolithic framework which computes simultaneously for the fluid and the structure unknowns within a unique solver. The mathematical description and the numerical schemes are designed in such a way that more complicated constitutive relations (and more realistic ones for biomechanics applications) for the fluid as well as for the structural part can be easily incorporated. We used the well-known Q_2P_1 Crouzeix-Raviart finite element pair for discretization in space and as a time-stepping algorithm

7. CONCLUSIONS

we used the strongly A-stable Backward-Euler scheme for both solid and fluid parts, or alternatively the Backward Euler-scheme for the fluid domain and the generalized-alpha scheme for the solid domain. Furthermore, a stability result using the Backward-Euler time-stepping scheme for both fluid and solid part and the finite element method for the space discretization has been proved. The resulting nonlinear discretized algebraic system of equations has been solved by a Quasi-Newton method, where the Jacobian matrix is approximated by neglecting the directional derivative of the fluid operator terms with respect to fluid-domain perturbations, and the resulting linear system has been solved by multilevel domain decomposition techniques. Our strategy is to solve several local subproblems over subdomain patches using the Schur-complement or the GMRES smoother within a multigrid iterative solver.

For validation and evaluation of the accuracy of the proposed methodology, we presented corresponding results for a set of two FSI benchmarking configurations (“Channel flow around cylinder with attached elastic beam”, see [Turek & Hron \[2006\]](#)) which describe the self-induced elastic deformation of a beam attached to a cylinder in a laminar channel flow, allowing either stationary or periodically-oscillating deformations, and for a benchmark proposed by COMSOL multiphysics where a narrow vertical structure attached to the bottom wall of a channel bends under the force due to both viscous drag and fluid pressure. Our results show that the proposed numerical algorithm allows to achieve the same solution accuracy in the user selected region (e.g. interface) with a smaller number of degrees of freedom with respect to standard multigrid algorithms. We have also shown the effectiveness of the implementation of the multilevel domain decomposition algorithm on parallel architectures.

Then, as an example of fluid-structure interaction (FSI) in biomedical problems, we considered the academic numerical test which consists in simulating the pressure wave propagation through a straight compliant vessel. The test shows the applicability and the accuracy of our approach also to three-dimensional time-dependent problems.

The presented calculations are for relatively simple examples in order to test accurately the proposed numerical algorithm, but the numerical formulation is general enough to allow a straightforward extension to more realistic material

models. For example the material anisotropy can be taken into account using the following energy function

$$\Psi = c_1(I_c - 3) + c_2(II_c - 3) + c_3(|\mathbf{Fa}| - 1)^2,$$

with \mathbf{a} being the preferred material direction and the term $|\mathbf{Fa}|$ representing the extension in the direction \mathbf{a} . Viscoelastic behavior may be relevant in muscular arteries and plasticity effects should be considered when major strains are involved. In the same manner the constitutive relation for the fluid can be directly extended to non-Newtonian model (e.g. the Carreau Model) in order to describe the shear thinning property of blood. Finally, the coupling with models for biochemical transport processes involved in vascular physiology and biology and with the energy conservation equation when the variation of blood temperature is relevant would allow to perform more realistic simulations for industrial applications.

7. CONCLUSIONS

Appendix

During my PhD period we developed a numerical algorithm to initialize the volume fraction field of the *volume-of-fluid* method starting from a given implicit equation of the interface, $f(x, y) = 0$ in 2D and $f(x, y, z) = 0$ in 3D (Bnà *et al.* [2014]). This algorithm has been implemented in the VOFI library that will be distributed as an open-source software.

The *volume-of-fluid* method is the most popular numerical technique to follow the evolution of interfaces in two-phase or free-surface flows within the framework of DNS (Bnà *et al.* [2013b]). The volume-of-fluid method is based on the phase indicator or characteristic function $\chi(\mathbf{x}, t)$, a multidimensional Heaviside step function with value 1 in the reference phase, and 0 in the secondary phase or vacuum. The color function or volume fraction C is the discrete version of χ

$$C(t) = \frac{1}{V} \int_V \chi(\mathbf{x}, t) \, d\mathbf{x},$$

where V is the volume (area in 2D) of the cell under investigation. The volume fraction C represents the volume of the cell which is occupied by the reference phase; it is bounded by the interface and the cell boundary and it is normalized to 1, i.e. $0 \leq C \leq 1$.

A simple, but rather rough initialization of the volume fraction in each cell of the computational domain can be easily attained by considering an arbitrary number of internal nodes, either on a regular submesh or randomly generated. The local C value is then given by the ratio of the number of nodes inside the reference phase to the total number of nodes. More advanced techniques for multidimensional integration include Monte Carlo methods with different sam-

pling strategies to improve the efficiency of the method (Evans & Swartz [2000]; Hahn [2005]). Alternatively, it is possible to initialize the scalar C field with a recursive local mesh refinement in the cut cells (Cummins *et al.* [2005]). At the finest level the interface can be approximated by a linear interface, which can be easily integrated (Scardovelli & Zaleski [2000]). Very precise initial data, which are necessary for example to compute the convergence rate with grid spacing of curvature calculations (Popinet [2009]) or of instability growth rates (Bagué *et al.* [2010]), may require initialization of the volume fractions directly from an integration of the analytical expression of the interface.

However, direct initialization is usually rather cumbersome, in particular for a closed line or surface, such as a circle and a sphere. In these cases the interface must be subdivided into several portions, each of them with a different analytical expression, and in each cut cell the local limits of integration must be computed. Furthermore, this procedure is usually not automatic, in the sense that some editing of the numerical code is required as the initial interface is moved around in the computational domain or the grid resolution is changed.

In the paper of Bnà *et al.* [2014], we consider square cells in two-dimensions (2D) and cubic cells in three-dimensions (3D), always with a side of length h_0 , and we present a numerical algorithm to initialize the volume fraction field starting from a given implicit equation of the interface, $f(x, y) = 0$ in 2D and $f(x, y, z) = 0$ in 3D.

References

- ADAMS, R.A. (1975). *Sobolev spaces*. Academic press, New York, 1st edn. [19](#), [21](#)
- AMESTOY, P., DUFF, I. & L'EXCELLENT, J.Y. (2000). Multifrontal parallel distributed symmetric and unsymmetric solvers. *Comput. Methods in Appl. Mech. Eng.*, **184**, 501–520. [6](#), [100](#)
- ASTARITA, G. & MARRUCCI, G. (1974). *Principles of Non-Newtonian Fluid Mechanics*. McGraw Hill, London. [58](#), [59](#)
- AULISA, E., MANSERVISI, S. & SESHAIYER, P. (2006). A computational multi-level approach for solving 2D NavierStokes equations over non-matching grids. *Comput. Meth. Appl. Mech. Eng.*, **195**, 4604–4616. [5](#), [105](#)
- AULISA, E., MANSERVISI, S. & SESHAIYER, P. (2008). A multilevel domain decomposition approach to solving coupled applications in computational fluid dynamics. *Int. J. Numer. Meth. Fluids*, **56**, 1139–1145. [5](#), [105](#)
- AULISA, E., MANSERVISI, S. & SESHAIYER, P. (2009). A computational domain decomposition approach for solving coupled flow-structure-thermal interaction problems. In J. Graef, R. Koomullil, H. Lim, R. Shivaji, B. Soni & J. Zhu, eds., *Seventh Mississippi State Conference on Differential Equations and Computational Simulations*, 17, 13–31, *Electron. J. Diff. Eqns.* [5](#), [105](#)
- BAGUÉ, A., FUSTER, D., POPINET, S., SCARDOVELLI, R. & ZALESKI, S. (2010). Instability growth rate of two-phase mixing layers from a linear

REFERENCES

- eigenvalue problem and an initial-value problem. *Phys. Fluids*, **22**, 092104–1–092104–9. [160](#)
- BALAY, S., GROPP, W.D., MCINNES, L.C. & SMITH, B.F. (1997). Efficient management of parallelism in object oriented numerical software libraries. In E. Arge, A.M. Bruaset & H.P. Langtangen, eds., *Modern Software Tools in Scientific Computing*, 163–202, Birkhäuser Press. [5](#)
- BALAY, S., BROWN, J., , BUSCHELMAN, K., EIJKHOUT, V., GROPP, W.D., KAUSHIK, D., KNEPLEY, M.G., MCINNES, L.C., SMITH, B.F. & ZHANG, H. (2013). PETSc users manual. Tech. Rep. ANL-95/11 - Revision 3.4, Argonne National Laboratory. [5](#), [6](#), [116](#)
- BATHE, K. & LEDEZMA, G. (2007). Benchmark problems for incompressible fluid flows with structural interactions. *Computers & Structures*, **85**, 628–644. [7](#)
- BATHE, K. & ZHANG, H. (2004). Finite element developments for general fluid flows with structural interactions. *Int. J. Numer. Meth. Engng.*, **60**, 213–232. [95](#), [97](#)
- BAZZI, G. & ANDERHEGGEN, E. (1982). The ρ -family of algorithms for time-step integration with improved numerical dissipation. *Earthquake Engineering and Structural Dynamics*, **10**, 537–550. [81](#)
- BEIRÃO DA VEIGA, H. (2004). On the existence of strong solutions to a coupled fluid-structure evolution problem. *J. Math. Fluid Mech.*, **6**, 21–52. [26](#)
- BELYTSCHKO, T.B. (1977). Methods and programs for analysis of fluid-structure systems. *Nuclear Engineering design*, **42**, 41–52. [33](#)
- BELYTSCHKO, T.B. & KENNEDY, J.M. (1976). A fluid-structure finite element method for the analysis of reactor safety problems. *Nuclear Engineering design*, **38**, 71–81. [33](#)
- BELYTSCHKO, T.B. & MULLEN, R. (1981). Two-dimensional fluid-structure impact computations with regularization. *Comput. Meth. Appl. Mech. Eng.*, **27**, 139–154. [33](#)

REFERENCES

- BELYTSCHKO, T.B. & SCHUMANN, U. (1980). Fluid structure interactions in light water reactor systems. *Nuclear Engineering design*, **60**, 173–195. [33](#)
- BELYTSCHKO, T.B., FLANAGAN, D.P. & KENNEDY, J.M. (1982). Finite element methods with user-controlled meshes for fluid-structure interaction. *Comput. Meth. Appl. Mech. Eng.*, **33**, 669–688. [33](#)
- BENSON, D.J. (1984). An efficient, accurate, simple ale method for nonlinear finite element programs. *Comput. Meth. Appl. Mech. Eng.*, **89**, 305–350. [33](#)
- BNÀ, S., BORNIA, G. & MANSERVISI, S. (2012a). A Monolithic FEM Multigrid Penalty-Projection Solver for Incompressible Fluid-Structure Interaction. In A. Andrade-Campos, N. Lopes, R. Valent & H. Varum, eds., *First ECCOMAS Young Investigators Conference*, Aveiro, Portugal. [5](#)
- BNÀ, S., MANSERVISI, S. & BORNIA, G. (2012b). A Penalty-Projection Algorithm for Incompressible Fluid-Structure Interaction. In H. Mang, J. Eberhardsteiner, H. Bohm & F. Rammerstorner, eds., *European Congress on Computational Methods in Applied Sciences and Engineering (ECCOMAS 2012)*, Vienna, Austria. [5](#)
- BNÀ, S., AULISA, E. & MANSERVISI, S. (2013a). A Multilevel Domain Decomposition Solver for Monolithic Fluid-Structure Interaction Problems. In *11th International Conference of Numerical Analysis and Applied Mathematics 2013: ICNAAM 2013*, vol. 1558, 871–874, AIP. [5](#)
- BNÀ, S., CERVONE, A., CHENADEC, V., MANSERVISI, S. & SCARDOVELLI, R. (2013b). Review of split and unsplit geometric advection algorithms. In *11th International Conference of Numerical Analysis and Applied Mathematics 2013: ICNAAM 2013*, vol. 1558, 875–878, AIP. [159](#)
- BNÀ, S., MANSERVISI, S., SCARDOVELLI, R., YECKO, P. & ZALESKI, S. (2014). Numerical integration of implicit functions for the initialization of the vof function, submitted. [159](#), [160](#)
- BONET, J. & WOOD, R.D. (1997). *Nonlinear continuum mechanics for finite element analysis*. Cambridge university press, Cambridge. [27](#)

REFERENCES

- BRENNER, S.C. & SCOTTBROWN, L.R. (2008). *The Mathematical Theory of Finite Element Methods*. Springer. 108
- BREZIS, H. (1983). *Analyse Fonctionnelle*. Masson, Paris. 13
- BREZZI, F. & FORTIN, M. (1991). *Mixed and Hybrid Finite Element Methods*. Springer-Verlag, New York. 76
- CAUSIN, P., GERBEAU, J. & NOBILE, F. (2005). Added-mass effect in the design of partitioned algorithms for fluid-structure problems. *Comput. Meth. Appl. Mech. Eng.*, **194**, 4506–4527. 4, 8
- CHAMBOLLE, A., DESJARDINS, B., ESTEBAN, M.J. & GRANDMONT, C. (2005). Existence of weak solutions for the unsteady interaction of a viscous fluid with an elastic plate. *J. Math. Fluid Mech.*, **7**, 368–404. 26, 27
- CHANG, Y., HOU, T., MERRIMAN, B. & OSHER, S. (1996). A level set formulation of eulerian interface capturing methods for incompressible fluid flows. *J. of Comp. Phys.*, **124**, 449–464. 2
- CHUNG, J. & HULBERT, G.M. (1993). A time integration algorithm for structural dynamics with improved numerical dissipation: The generalized- α method. *Journal of Applied Mechanics*, **60**, 371–375. 81
- CIARLET, P. (1998). *Mathematical elasticity. Volume I, Three-Dimensional Elasticity*, vol. 20 of *Studies in Mathematics and its Applications*. Elsevier Science, Amsterdam. 27
- COUTAND, D. & SHKOLLER, S. (2005). Motion of an elastic solid inside an incompressible viscous fluid. *Arch. Ration. Mech. Anal.*, **176**, 25–102. 26
- CUMMINS, S., FRANCOIS, M. & KOTHE, D. (2005). Estimating curvature from volume fractions. *Computers and Structures*, **83**, 425–434. 160
- DAVIS, T.A. & DUFF, I.S. (1999). A combined unifrontal/multifrontal method for unsymmetric sparse matrices. *SACM Trans. Math. Software*, **25**, 1–19. 6, 100

REFERENCES

- DENNIS, J.E.J. & SCHNABEL, R.B. (1996). *Numerical Methods for Unconstrained Optimization and Nonlinear Equations*. SIAM, Philadelphia. 99
- DEPARIS, S., FERNÁNDEZ, M. & FORMAGGIA, L. (2003a). Acceleration of a fixed point algorithm for fluid-structure interaction using transpiration conditions. *M2AN. Math. Model. Numer. Anal.*, **37**, 601–616. 95
- DEPARIS, S., FERNÁNDEZ, M., FORMAGGIA, L. & NOBILE, F. (2003b). Acceleration of a fixed point algorithm for fluid structure interaction using transpiration conditions. In *Second MIT Conference on Computational Fluid and Solid Mechanics*, Elsevier. 4
- DEPARIS, S., DISCACCIATI, M., FOURESTEY, G. & QUARTERONI, A. (2006). Fluid-Structure algorithms based on Steklov-Poincaré operators. *Comput. Meth. Appl. Mech. Eng.*, **195**, 5797–5812. 4
- DESJARDINS, B. & ESTEBAN, M.J. (2000). On weak solutions for fluid-rigid structure interaction: compressible and incompressible models. *Comm. Partial Diff. Eq.*, **25**, 1399–1413. 26
- DESJARDINS, B., ESTEBAN, M.J., GRANDMONT, C. & LE TALEC, P. (2001). Weak solutions for a fluid-elastic structure interaction model. *Rev. Mat. Comput.*, **14**, 523–538. 26
- DONEA, J. (1983). Arbitrary lagrangian-eulerian finite element methods. In T.B. Belytschko & T.J.R. Hughes, eds., *Numerical Methods for Transient Analysis*, 473–516, North Holland, Amsterdam. 2, 33
- DONEA, J., GIULIANI, S. & HALLEUX, J. (1982). An Arbitrary Lagrangian Eulerian Finite Element Method for transient dynamic Fluid-Structure Interactions. *Comput. Meth. Appl. Mech. Eng.*, **33**, 689–723. 2, 33
- EVANS, D. (1983). *Preconditioning Methods: Analysis and Applications*. Gordon & Breach, New York. 104
- EVANS, M. & SWARTZ, T. (2000). *Approximating Integrals via Monte Carlo and Deterministic Methods*. Oxford University Press, New York, USA. 160

REFERENCES

- FERNÁNDEZ, M. & MOUBACHIR, M. (2003). An exact block-newton algorithm for the solution of implicit time discretized coupled systems involved in fluid-structure interaction problems. In K.J. Bathe, ed., *Second M.I.T. Conference on Computational Fluid and Solid Mechanics*, 1337–1341, Elsevier, Amsterdam. [97](#)
- FERNÁNDEZ, M. & MOUBACHIR, M. (2004). Numerical simulation of fluid-structure systems via Newton’s method with exact Jacobians. In P. Neittaanmki, T. Rossi, K. Majava & O. Pironneau, eds., *Fourth European Congress on Computational Methods in Applied Sciences and Engineering*, vol. 1, Jyväskylä, Finland. [97](#)
- FERNÁNDEZ, M. & MOUBACHIR, M. (2005). A Newton method using exact Jacobians for solving fluid-structure coupling. *Computers and Structures*, **83**, 127–142. [4](#), [6](#), [7](#), [8](#), [97](#), [145](#), [149](#)
- FERNÁNDEZ, M., GERBEAU, J. & GRANDMONT, C. (2007). A projection semi-implicit scheme for the coupling of an elastic structure with an incompressible fluid. *International Journal of Numerical Methods in Engineering*, **69**, 794–821. [4](#), [145](#)
- FORMAGGIA, L., GERBEAU, J., NOBILE, F. & QUARTERONI, A. (2001). On the coupling of 3D and 1D Navier-Stokes equations for flow problems in compliant vessels. *Comput. Meth. Appl. Mech. Eng.*, **191**, 561–582. [8](#), [145](#), [146](#), [149](#)
- FORMAGGIA, L., QUARTERONI, A. & VENEZIANI, A. (2009). *Cardiovascular Mathematics*. Springer. [150](#)
- FÖRSTER, C., WALL, W. & RAMM, E. (2007). Artificial added mass instabilities in sequential staggered coupling of nonlinear structures and incompressible viscous flows. *Comput. Meth. Appl. Mech. Eng.*, **196**, 1278–1293. [4](#)
- FORTIN, A. (1981). Old and new finite elements for incompressible flows. *Int. J. for Numer. Meth. in Fluids*, **1**, 347–364. [77](#)

REFERENCES

- FUNG, Y.C. (1993). *Biomechanics: Mechanical Properties of Living Tissues*. Springer-Verlag, New York, USA. [8](#)
- GERBEAU, J.F. & VIDRASCU, M. (2003). A quasi-Newton algorithm based on a reduced model for fluid-structure interaction problems in blood flows. *ESAIM: Mathematical Modeling and Numerical Analysis*, **37**, 631–647. [4](#), [6](#), [95](#), [145](#)
- GHOSH, S. & KIKUCHI, N. (1991). An arbitrary lagrangian-eulerian finite element method for large deformation analysis of elastic-viscoplastic solids. *Comput. Meth. Appl. Mech. Eng.*, **86**, 127–188. [33](#)
- GIRAULT, V. & P.-A., R. (1986). *Finite Element Methods for Navier-Stokes Equations*. Springer-Verlag, Berlin. [76](#)
- GLOWINSKI, R., PAN, T. & PERIAUX, J. (1994a). A Fictitious domain method for Dirichlet problem and applications. *Comput. Meth. Appl. Mech. Eng.*, **111**, 283–303. [2](#)
- GLOWINSKI, R., PAN, T. & PERIAUX, J. (1994b). A Fictitious domain method for external incompressible viscous flow modeled by Navier-Stokes equations. *Comput. Meth. Appl. Mech. Eng.*, **112**, 133–148. [2](#)
- GRANDMONT, C. & MADAY, Y. (2000). Existence for an unsteady fluid-structure interaction problem. *M2AN Math. Model. Numer. Anal.*, **34**, 609–63. [26](#)
- GUERMOND, J., MINEV, P. & SHEN, J. (2006). An overview of projection methods for incompressible flows. *Computer Methods in Applied Mechanics and Engineering*, **195**, 6011–6045. [5](#)
- GURTIN, M.E. (1981). *Topics in Finite Elasticity*. SIAM. [27](#)
- HABER, R.B. (1984). A mixed eulerian-lagrangian displacement model for large deformation analysis in solid mechanics. *Comput. Meth. Appl. Mech. Eng.*, **43**, 277–292. [33](#)
- HAHN, T. (2005). Cuba - a library for multidimensional numerical integration. *Comput. Phys. Commun.*, **168**, 78–95. [160](#)

REFERENCES

- HAUPT, P. (2000). *Continuum Mechanics and Theory of Materials*. Springer. [27](#)
- HEIL, M. (2004). An Efficient Solver to the Fully Coupled Solution of Large-Displacement Fluid-Structure Interaction Problems. *Comput. Meth. Appl. Mech. Eng.*, **193**, 1–23. [4](#), [95](#), [97](#)
- HILBER, H.M., HUGHES, T.J.R. & TAYLOR, R.L. (1977). Improved numerical dissipation for time integration algorithms in structural dynamics. *Earthquake Engineering and Structural Dynamics*, **5**, 283–292. [81](#)
- HIRT, C.W., AMSDEN, A.A. & COOK, J.L. (1974). An arbitrary lagrangian-eulerian computing method for all flow speeds. *Journal of Computational Physics*, **14**, 227–253. [33](#)
- HOFF, C. & PAHL, P.J. (1988a). Development of an implicit method with numerical dissipation from a generalized single-step algorithm for structural dynamics. *Computer Methods in Applied Mechanics and Engineering*, **67**, 367–385. [81](#)
- HOFF, C. & PAHL, P.J. (1988b). Practical performance of the θ_1 method and comparison with other dissipative algorithms in structural dynamics. *Computer Methods in Applied Mechanics and Engineering*, **67**, 87–110. [81](#)
- HRON, J. & TUREK, S. (2006). A monolithic fem/multigrid solver for ale formulation of fluid structure interaction with application in biomechanics. In H.J. Bungartz & M. Schäfer, eds., *Fluid-Structure Interaction: Modeling, Simulation, Optimization*, vol. 53 of *Lecture Notes in Computational Science and Engineering*, 146–170, Springer. [4](#), [6](#), [95](#), [97](#), [99](#), [113](#)
- HRON, J., OUAZZI, A. & TUREK, S. (2002). A computational comparison of two fem solvers for nonlinear incompressible flow. In E. Bänsch, ed., *Challenges in Scientific Computing*, vol. 53, 87–109, Springer. [3](#)
- HÜBNER, B., WALHORN, E. & DINKLER, D. (2004). A Monolithic approach to fluid-structure interaction using space-time finite elements. *Comput. Meth. Appl. Mech. Eng.*, **193**, 2087–2104. [2](#)

REFERENCES

- HUGHES, T.J.R. & TEZDUYAR, T.E. (1984). Finite element methods for first order hyperbolic systems with particular emphasis on the compressible euler equations. *Comput. Meth. Appl. Mech. Eng.*, **45**, 217–284. [33](#)
- HUGHES, T.J.R., LIU, W.K. & ZIMMERMANN, T.K. (1981). Lagrangian eulerian finite element formulation for incompressible viscous flows. *Comput. Meth. Appl. Mech. Eng.*, **29**, 329–349. [2](#), [33](#)
- HUMPHREY, J. (1995). Mechanics of the arterial wall: review and directions. *Crit. Rev. Biomed. Eng.*, **23**, 1–62. [8](#)
- JANSEN, K.E., WHITING, C.H. & HULBERT, G.M. (2000). A generalized- α method for integrating the filtered navier-stokes equations with a stabilized finite element method. *Comput. Meth. Appl. Mech. Eng.*, **190**, 305–319. [81](#), [83](#)
- JOBELIN, M., LAPUERTA, C., LATCHÉ, J.C., ANGOT, P. & PIAR, B. (2006). A finite element penalty-projection method for incompressible flows. *Journal of Computational Physics*, **217**, 502–518. [5](#)
- KELLEY, C. (1999). *Iterative methods for Optimization*. SIAM, Philadelphia. [100](#)
- KEVIN, L., KIRBY, R. & VAN BLOEMEN WAANDEERS, B. (2010). Unified embedded parallel finite element computations via software-based fréchet differentiation. *SIAM J. Sci. Comput.*, **32**, 3323–3351. [98](#)
- KU, D. (1997). Blood flow in arteries. *Annu. Rev. Fluid Mech.*, **29**, 399–434. [57](#)
- LE TALLEC, P. & MANI, S. (2000). Numerical analysis of a linearized fluid-structure interaction problem. *Num. Math.*, **87**, 317–354. [26](#)
- LE TALLEC, P. & MOURO, J. (2001). Fluid structure interaction with large structural displacements. *Comput. Meth. Appl. Mech. Eng.*, **190**, 3039–3067. [4](#)
- LI, X.S. (2005). An overview of SuperLU: Algorithms, implementation, and user interface. *ACM Trans. Math. Software*, **31**, 302–325. [100](#)
- LIONS, J.L. & MAGENES, E. (1968a). *Problèmes aux Limites non Homogènes et Applications*, vol. 1. Dunod, Paris. [21](#), [22](#)

REFERENCES

- LIONS, J.L. & MAGENES, E. (1968b). *Problèmes aux Limites non Homogènes et Applications*, vol. 2. Dunod, Paris. [21](#)
- LIU, W.K. & GVILDYS, J. (1986). Fluid-structure interaction of tanks with an eccentric cor barrel. *Comput. Meth. Appl. Mech. Eng.*, **58**, 51–57. [33](#)
- LIU, W.K. & MA, D. (1982). Computer implementation aspects for fluid structure interaction problems. *Comput. Meth. Appl. Mech. Eng.*, **31**, 129–148. [33](#)
- LIU, W.K., BELYTSCHKO, T.B. & CHANG, H. (1986). An arbitrary lagrangian-eulerian finite element method for path-dependent materials. *Comput. Meth. Appl. Mech. Eng.*, **58**, 227–245. [33](#)
- MANSERVISI, S. (2006). Numerical analysis of Vanka-type solvers for steady stokes and Navier-Stokes flows. *SIAM Journal on Numerical Analysis*, **44**, 2025–2056. [112](#)
- MASUD, A. & HUGHES, T. (1997). A Space-time Galerkin/least squares finite element formulation of the Navier-Stokes equations for moving domain problem. *Comput. Meth. Appl. Mech. Eng.*, **146**, 91–126. [2](#)
- MATTHIES, H. & STEINDORF, J. (2000). Numerical efficiency of different partitioned methods for fluid-structure interaction. *Z. Angew. Math. Mech.*, **2**, 557–558. [4](#)
- MATTHIES, H. & STEINDORF, J. (2002). Partitioned but strongly coupled iteration schemes for nonlinear fluid-structure interaction. *Computers and Structures*, **80**, 1991–1999. [95](#)
- MATTHIES, H. & STEINDORF, J. (2003). Partitioned strong coupling algorithms for fluid-structure interaction. *Computers and Structures*, **81**, 805–812. [95](#)
- MITTAL, S. & TEZDUYAR, T. (1995). Parallel finite element simulation of 3D incompressible flows: fluid-structure interactions. *Int. J. Numer. Methods Fluids*, **21**, 933–953. [2](#)

REFERENCES

- MOK, D., WALL, W. & RAMN, E. (2001). Accelerated iterative substructuring schemes for instationary fluid-structure interaction. In *Cambridge, MA*, vol. 1, 1325–1328, Elsevier, Amsterdam. [95](#)
- MOLENAAR, J. (1991). A two-grid analysis of the combination of mixed finite elements and vanka-type relaxation. In W. Hackbusch & U. Trottenberg, eds., *Multigrid methods III, Proc. 3rd Eur. Conf., Bonn/Germany, ISNM 98*, 313–323, Birkhäuser user Verlag. [112](#)
- NEWMARK, N.M. (1959). A method of computation for structural dynamics. *Journal of the Engineering Mechanics Division ASCE*, **85**, 67–94. [81](#)
- NOBILE, F. (2001). *Numerical Approximation of Fluid-Structure Interaction problems with application to haemodynamics*. Ph.D. thesis, École Polytechnique Fédérale de Lausanne. [89](#), [95](#)
- NOH, W.F. (1964). A time dependent, two space dimensional coupled eulerian lagrangian code. In B. Aldert, ed., *Methods in Computational Physics*, 117, Academic Press, New York. [33](#)
- PESKIN, C. (1977). Numerical analysis of blood flow in the heart. *J. of Comp. Phys.*, **25**, 220–252. [2](#)
- PESKIN, C. & MCQUEEN, D. (1989). A Three Dimensional Computational Method for Blood Flow in the Heart - I Immersed Elastic Fibers in a Viscous Incompressible Fluid. *J. of Comp. Phys.*, **81**, 372–405. [2](#)
- POPINET, S. (2009). An accurate adaptive solver for surface–tension–driven interfacial flows. *J. Comput. Phys.*, **228**, 5838–5866. [160](#)
- PRACHT, W.E. (1975). Calculating three-dimensional fluid flows at all flow speeds with an eulerian-lagrangian computing mesh. *Journal of Computational Physics*, **17**, 132–159. [33](#)
- PRESS, W.H., TEUKOLSKY, S., VETTERLING, W.T. & FLANNERY, B.P. (2002). *Numerical Recipes in C++. The Art of Scientific Computing*. Cambridge University Press, Cambridge. [99](#)

REFERENCES

- QUARTERONI, A. (2009). *Numerical Models for Differential Problems*. Springer. 102
- QUARTERONI, A. & VALLI, A. (1994). *Numerical Approximation of Partial Differential Equations*. Springer. 68, 103
- QUARTERONI, A., TUVERI, M. & VENEZIANI, A. (2000). Computational vascular fluid dynamics: problems, models and methods. *Comput. Visual. Sci.*, **190**, 163–197. 8
- QUARTERONI, A., SACCO, A. & SALERI, F. (2010). *Numerical Mathematics*. Springer. 96
- RAZZAQ, M. (2011). *Finite element simulation techniques for incompressible fluid-structure interaction with applications to bio-engineering and optimization*. Ph.D. thesis, Technischen Universität Dortmund, Fakultät für Mathematik. 113
- RAZZAQ, M., TUREK, S., HRON, J., ACKER, J.F., WEICHERT, F., GRUNWALD, I.Q., ROTH, C., WAGNER, B.F. & ROMEIKE, M. (2010). Numerical simulation and benchmarking of fluid-structure interaction with application to hemodynamics. In G.P. Galdi & R. Rannacher, eds., *Fundamental Trends in Fluid-Structure Interaction*, vol. 1 of *Contemporary Challenges in Mathematical Fluid Dynamics and its applications*, 171–199, World Scientific. 126
- RUMPF, M. (1998). On equilibria in the interaction of fluids and elastic solids. In J. Heywood, K. Masuda, R. Rautmann & V. Solonnikov, eds., *Theory of the Navier-Stokes equations*, 136–158, World Sci., River Edge, New York. 26
- SAAD, Y. (2000). *Iterative Methods for Sparse Linear Systems*. SIAM, 2nd edn. 6, 101, 104
- SACKINGER, P., SCHUNK, P. & RAO, R. (1996). A Newton-Raphson pseudo-solid domain mapping technique for free and moving boundary problems: a finite element implementation. *J. of Comp. Phys.*, **125**, 83–103. 51

REFERENCES

- SCARDOVELLI, R. & ZALESKI, S. (2000). Analytical relations connecting linear interfaces and volume fractions in rectangular grids. *J. Comput. Phys.*, **164**, 228–237. [160](#)
- SCHEBERL, J. & ZULEHNER, W. (2003). On schwarz-type smoothers for saddle point problems. *Numerische Mathematik*, **95**, 377–399. [112](#)
- SOKOLOWSKI, J. & J.-P., Z. (1992). *Introduction to shape optimization*, vol. 16 of *Springer Series in Computational Mathematics*. Springer-Verlag, Berlin. [97](#)
- TEZDUYAR, T. (2001). Finite element methods for fluid dynamics with moving boundaries and interfaces. *Arch. Comput. Meth. Engrg.*, **8**, 83–130. [95](#), [97](#)
- TEZDUYAR, T. & BENNEY, R. (2003). Mesh moving techniques for fluid-structure interactions with large displacements. *Int. J. Applied Mechanics*, **70**, 58–66. [51](#), [52](#)
- TEZDUYAR, T., BEHR, M. & LIOU, J. (1992a). A new strategy for finite element computations involving moving boundaries and interfaces - the deforming-spatial-domain/space-time procedure: I. the concept and preliminary numerical tests. *Comput. Meth. Appl. Mech. Eng.*, **94**, 339–351. [2](#)
- TEZDUYAR, T., BEHR, M., MITTAL, S. & LIOU, J. (1992b). A new strategy for finite element computations involving moving boundaries and interfaces - the deforming-spatial-domain/space-time procedure: II. computation of free surface flows, two-liquid flows and flows with drifting cylinders. *Comput. Meth. Appl. Mech. Eng.*, **94**, 339–351. [2](#)
- TEZDUYAR, T.E., BEHR, M., MITTAL, S. & JOHNSON, A.A. (1992c). Computation of unsteady incompressible flows with the finite element methods. In P. Smolinski, W.K. Liu, G. Hulbert & K. Tamma, eds., *Space-Time Formulations, Iterative Strategies and Massively Parallel Implementations*, vol. 143 of *New Methods in Transient Analysis*, 7–24, ASME, New York. [53](#)
- TUREK, S. (1999). *Efficient Solvers for Incompressible Flow Problems: An Algorithmic and Computational Approach*. Springer. [6](#), [74](#), [99](#), [112](#), [117](#)

REFERENCES

- TUREK, S. & HRON, J. (2006). Proposal for numerical benchmarking of fluid-structure interaction between an elastic object and laminar incompressible flow. In H.J. Bungartz & M. Schäfer, eds., *Fluid-Structure Interaction: Modeling, Simulation, Optimization*, vol. 53 of *Lecture Notes in Computational Science and Engineering*, 371–385, Springer. [7](#), [126](#), [156](#)
- TUREK, S. & SCHÄFER, M. (1996). Benchmark computations of laminar flow around a cylinder. In E.H. Hirschel, ed., *Flow Simulation with High-Performance Computers II*, vol. 52 of *Notes on Numerical Fluid Mechanics*, 547–566, Vieweg. [112](#), [119](#), [124](#), [126](#), [128](#)
- TUREK, S., HRON, J., MÁDLÍK, M., RAZZAQ, M., WOBKER, H. & ACKER, J.F. (2010a). Numerical simulation and benchmarking of a monolithic multi-grid solver for fluid-structure interaction problems with application to hemodynamics. In H.J. Bungartz, M. Mehl & M. Schäfer, eds., *Fluid-Structure Interaction II: Modeling, Simulation, Optimization*, vol. 73 of *Lecture Notes in Computational Science and Engineering*, 193–220, Springer. [126](#)
- TUREK, S., HRON, J., RAZZAQ, M., WOBKER, H. & SCHÄFER, M. (2010b). Numerical benchmarking of fluid-structure interaction: A comparison of different discretization and solution approaches. In H.J. Bungartz, M. Mehl & M. Schäfer, eds., *Fluid-Structure Interaction II: Modeling, Simulation, Optimization*, vol. 73 of *Lecture Notes in Computational Science and Engineering*, 413–424, Springer. [126](#), [135](#), [136](#)
- VAN DER VORST, H. (1989). High performance preconditioning. *SIAM J. Sci. Stat. Comput.*, **10**, 1174–1185. [104](#)
- VAN DER VORST, H. (2003). *Iterative Krylov Methods for Large Linear Systems*. Cambridge University Press. [104](#)
- VANKA, S.P. (1985). Implicit Multigrid Solutions of Navier-Stokes Equations in Primitive Variables. *J. of Comp. Phys.*, **65**, 138–158. [111](#)
- VANKA, S.P. (1986). Block-implicit multigrid calculation of two-dimensional recirculating flows. *Comput. Methods Appl. Mech. Eng.*, **59**, 29–48. [111](#)

REFERENCES

- VITO, R.P. & DIXON, S.A. (2003). Blood vessel constitutive models. *Annual Review of Biomedical Engineering*, **5**, 413–439. [8](#)
- VOLKER, J. & TOBISKA, L. (2000). Numerical performance of smoothers in coupled multigrid methods for the parallel solution of the incompressible navier-stokes equations. *International Journal for Numerical Methods in Fluids*, **33**, 453–473. [117](#)
- WALBURN, F.J. & SCHNECK, D.J. (1976). A constitutive equation for whole human blood. *Biorheol.*, **13**, 201–210. [60](#)
- WESSELING, P. & OOSTERLEE, C.W. (2001). Geometric multigrid with applications to computational dynamics. *Journal of Computational and Applied Mathematics*, **128**, 311–334. [112](#)
- WILSON, E.L. (1968). A computer program for the dynamic stress analysis of underground structures. Tech. Rep. SESM No. 68-1, Division of Structural Engineering and Structural Mechanics - University of California, Berkeley, CA. [81](#)
- WOBKER, H. & TUREK, S. (2009). Numerical studies of vanka-type smoothers in computational solid mechanics. In *Advances in Applied Mathematics and Mechanics*, vol. 1, 29–55, Springer. [112](#)
- WOOD, W.L., BOSSAK, M. & ZIENKIEWICZ, O.C. (1981). An alpha modification of newmark’s method. *International Journal for Numerical Methods in Engineering*, **15**, 1562–1566. [81](#)
- YOSIDA, K. (1974). *Functional Analysis*. Springer-Verlag, Berlin, 4th edn. [13](#)
- ZHANG, H., ZHANG, X., JI, S., GUO, Y., LEDEZMA, G., ELABBASI, N. & DECOUGNY, H. (2003). Recent development of fluid-structure interaction capabilities in the adina system. *Computers & Structures*, **81**, 1071–1085. [95](#), [97](#)